INSTITUTO POTOSINO DE INVESTIGACIÓN CIENTÍFICA Y TECNOLÓGICA, A.C.

POSGRADO EN CIENCIAS APLICADAS

Simulating Unusual Phenomena in Low Dimensional Systems

Tesis que presenta

M. C. Juan Pedro Palomares Báez

Para obtener el grado de

Doctor en Ciencias Aplicadas

En la opción de

Nanociencias y Nanotecnología

Codirectores de la Tesis:

Dr. José Luis Rodríguez López (DMA-IPICYT)

Dr. Boris Ivlev (IF-UASLP)

San Luis Potosí, S.L.P., Diciembre de 2011

CONSTANCIA DE APROBACIÓN DE LA TESIS

CRÉDITOS INSTITUCIONALES

Esta tesis fue elaborada en la División de Materiales Avanzados del Instituto Potosino de Investigación Científica y Tecnológica, A.C., bajo la dirección de los doctores José Luis Rodríguez López (DMA-IPICYT) y Boris Ivlev (IF-UASLP)

Durante la realización del trabajo el autor recibió una beca académica del Consejo Nacional de Ciencia y Tecnología (No. de registro 182521) y del Instituto Potosino de Investigación Científica y Tecnológica, A.C.

CERTIFICADO DE GRADO

IPICYT

Instituto Potosino de Investigación Científica y Tecnológica, A.C.

Acta de Examen de Grado

El Secretario Académico del Instituto Potosino de Investigación Científica y Tecnológica, A.C., certifica que en el Acta 036 del Libro Primero de Actas de Exámenes de Grado del Programa de Doctorado en Ciencias Aplicadas en la opción de Nanociencias y Nanotecnología está asentado lo siguiente:

En la ciudad de San Luis Potosí a los 19 días del mes de diciembre del año 2011, se reunió a las 12:00 horas en las instalaciones del Instituto Potosino de Investigación Científica y Tecnológica, A.C., el Jurado integrado por:

Dr. Boris Ivlev	**Presidente**	**UASLP**
Dr. José Luis Rodríguez López	**Secretario**	**IPICYT**
Dr. José Luis Ricardo Chávez	**Sinodal**	**IPICYT**
Dr. Juan Martín Montejano Carrizales	**Sinodal externo**	**UASLP**
Dr. Ricardo Alberto Guirado López	**Sinodal externo**	**UASLP**
Dr. Román López Sandoval	**Sinodal**	**IPICYT**

a fin de efectuar el examen, que para obtener el Grado de:

DOCTOR EN CIENCIAS APLICADAS
EN LA OPCIÓN DE NANOCIENCIAS Y NANOTECNOLOGÍA

sustentó el C.

Juan Pedro Palomares Baez

sobre la Tesis intitulada:

Simulating Unusual Phenomena in Low Dimensional Systems

que se desarrolló bajo la dirección de

Dr. José Luis Rodríguez López
Dr. Boris Ivlev (UASLP)

El Jurado, después de deliberar, determinó

APROBARLO

Dándose por terminado el acto a las 13:50 horas, procediendo a la firma del Acta los integrantes del Jurado. Dando fe el Secretario Académico del Instituto.

A petición del interesado y para los fines que al mismo convengan, se extiende el presente documento en la ciudad de San Luis Potosí, S.L.P., México, a los 19 días del mes de diciembre de 2011.

Dr. Marcial Bonilla Marín
Secretario Académico

Mtra. Ivonne Lizette Cuevas Vélez
Jefa del Departamento del Posgrado

DEDICATORIA

A mi familia y amigos, por brindarme siempre su apoyo...
Los amo..

AGRADECIMIENTOS

Quiero agradecer a mis asesores, los doctores José Luis Rodríguez López y Boris Ivlev por las muchas horas de discusión que llevaron a buen término este trabajo. A CONACYT por haberme otorgado la beca de doctorado. Al IPICYT por todas las facilidades otorgadas durante mi estancia en dicha institución y finalmente a todas las personas que de alguna u otra forma han formado parte de mi vida durante el desarrollo de mi doctorado. A todos, Gracias.

CONTENTS

LIST OF FIGURES

LIST OF TABLES

ABSTRACT

This thesis deals with physics phenomena in low dimensional systems, i.e., systems that range between few atoms and the bulk. The work deals with well studied (in this sense, classical) phenomena such as quantum tunneling and the enhancement of tunneling, surface reconstructions on surfaces, stability of structures vs. shape and size of nanoparticles, the mechanical properties studied in classical elastic theory for metals (such as hardness, ductility, malleability, etc.). However, althouh we have used and applied "classical" theories from both quantum and mechanical physics, we studied new, *unusual phenomena in low dimensional systems*. Thus, the reader will find in this thesis work, theoretical developments, hypothesis and results that advance explanations in unusual physical phenomena.

In quantum physics there are phenomena which do not have analogs in classical physics. One of these phenomena is quantum tunneling. The manifestation of this process is penetration of a particle or more complicated object through a potential barrier. Such process is forbidden by classical mechanics. Besides tunneling through static potential barriers there are many phenomena in labs and nature when tunneling occurs across nonstationary barriers. There are many examples of such processes, ionization of atoms by a nonstationary electric filed, ac electric current in junctions of metals or semiconductors, dissociation of molecules by a high-frequency fields, field emission from metals by the action of an ac field, decay of current states in Josephson junctions, alpha decay of nuclei initiated by an external flux of protons, etc. These processes of tunneling through nonstationary barriers require an adequate theoretical description.

Regarding studies for nanoparticles, we have faced the shape, structure and mechanical properties of metallic nanoparticles. First, we studied a particular truncation operated on the regular icosahedron gives rise to a new (not reported

before) particle with five-fold symmetry and external decahedral shape termed the decmon motif. These truncated icosahedra exposes internal facets (100) and (111)âĂŞadditional to the external (111) facets of the regular icosahedron. The uncovering of additional facets to the icosahedron gives rise to phenomena such as surface reconstructions and a delicate competition in the energy contribution coming from the new facets (100) and (111) to the total surface energy, a competence that makes arise some regions in the path from the icosahedron to the decahedron (m-$\mathrm{I_h}\rightarrow$st-$\mathrm{I_h}\rightarrow$s-$\mathrm{D_h}$) that becomes more stable than the icosahedron at that size. This study give us physical insights for nucleation and growth paths of metallic nanoparticles.

A main second problem faced had been the mechanical properties of multi-twinned metallic nanoparticles. We present support from theory and molecular dynamics simulations for startling experimental observations that reveal nanoparticles are extremely strong and malleable at the same time. These facts are unexpected since one of the nanotechnology leitmotifs "smaller is stronger" implies an almost brittle behaviour. Explanations are supported on the role of twin boundaries in finite grains, as has been demonstrated that ductility could be increased without losing strength by introducing coherent twin boundaries as is reported for polycrystalline materials though not for individual nanoparticles. Our results show unprecedented deformation on twinned nanoparticles up to 90%, both experimentally as well from molecular dynamics simulations.

In summary we present both from theory, and from numerical simulations techniques, the results for frontier phenomena in modern physics with potential applications or clear developments in the disciplines where each problem has been settled.

CHAPTER 1

INTRODUCTION

QUANTUM TUNNELING PHENOMENA

In quantum physics there are phenomena which do not have analogs in classical physics. One of these phenomena is quantum tunneling. The manifestation of this process is penetration of a particle or more complicated object through a potential barrier. De Broglie's idea of "matter as wave" suggests a startling consequence, and that's what is called the tunnel effect. More precisely, Schrödinger's wave equation can show this rigorously. Unlike the classical mechanics of particles, quantum mechanics allows light as well as particles (such as electrons and protons) to appear even where the "wall" of potential should prevent them from appearing. In Fig, 1.1, you may imagine the wall as the "wall of potential", in that any particle must have an energy, greater than a certain amount, for going through it and appearing on the other side. But even when the particle has a lower energy than that, it can go through the wall, just as a wave can appear on the other side (since its oscillation can go through the wall). Since particles as well as light have particle-wave duality, matter (with an appropriate energy) can go through the wall according to quantum mechanics. This can explain the spontaneous desintegration of radioactive substances (such as radium); even though the strong interaction within the nucleus forms a high wall of potential, alphadistintegration can occur because of the tunnel effect [1].

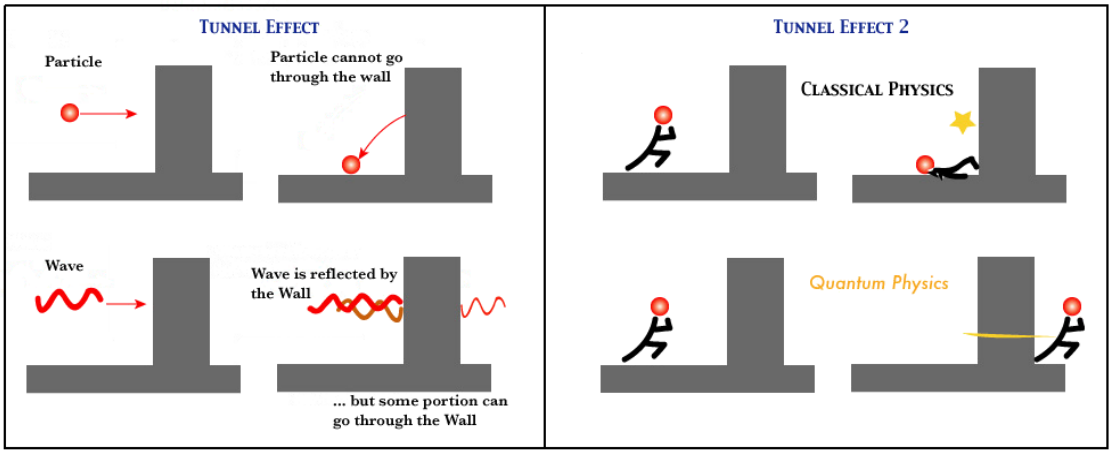

Figure 1.1: Cartooned picture of the tunnel effect. Due to particle-wave duality, quantum mechanics allows the matter to tunnel trough a "wall of potential".

The theory of tunneling through one-dimensional static barriers was developed by Wentzel, Kramers, and Brillouin (WKB) in twentieth of the last century [1]. The main feature of the WKB theory is that a wave function has a "tail“ under the barrier which can be extended over the entire barrier length. This provides a finite flux of particles from under the barrier. This flux becomes exponentially small when the barrier is high or long. Such potential barrier are called semiclassical.

Besides tunneling through static potential barriers there are many phenomena in labs and nature when tunneling occurs across nonstationary barriers. There are many examples of such processes, ionization of atoms by a nonstationary electric field, ac electric current in junctions of metals or semiconductors, dissociation of molecules by high-frequency fields, field emission from metals by the action of an ac field, decay of current states in Josephson junctions, alpha decay of nuclei initiated by an external flux of protons, etc.

The above processes of tunneling through nonstationary barriers require an adequate theoretical description. When a nonstationary field is very small the penetration of a particle through a barrier hardly differs from the conventional tunneling described by the semiclassical WKB theory. At a relatively big nonstationary field an overbarrier motion enters the problem when a particle should absorb a number of quanta to reach the barrier top. Many situations in experiments are associated with a *soft* nonstationary field with atypical frequency much less than the barrier height. This means that the particle has to absorb a large number of quanta to reach the barrier top. In the language of quantum mechanics, this corresponds to a high order of the perturbation theory when the probability is proportional to a high power of the nonstationary field.

There are some intermediate magnitudes of the nonstationary field when neither pure tunneling nor pure overbarrier motion describes the penetration through the barrier. In this case, the real motion through a barrier is a combination of quanta absorption and tunneling. The particle pays in its probability to absorb quanta and to reach the certain higher energy level but the subsequent tunneling is easier since it occurs in a more transparent part of the barrier. That higher energy is determined by a maximization of the total probability. This mechanism of barrier penetration in a nonstationary field is called *photon-assisted tunneling*.

The physics of photon-assisted tunneling has no conflict with intuition since the loss in absorption probability is compensated by the gain in probability of tunneling. In photon-assisted tunneling two processes (absorption and tunneling) are weakly coherent, which allows one to consider them independently and, therefore, the total probability is a product of two partial ones. This recalls static tunneling through two barriers, separated in space, when the quantum coherence between them is artificially destroyed by some external source. In this case, the two probabilities (tunneling and tunneling) are also independent and the total probability is a product of the partial ones.

In addition to quanta absorption, resulting in the increase of particle energy, quanta emission is also possible, followed by tunneling with a lower energy. At first sight, this process cannot lead to an enhancement of tunneling due to a double loss in probability: (i) emission of quanta and (ii) tunneling in a less transparent part of the barrier (with a lower energy). This conclusion is based on the assumption that quanta emission and tunneling are not strongly coherent processes which allows us to consider them almost independently. The remarkable point of physics of nonstationary tunneling is that the processes of quanta emission and tunneling may be strongly *coherent* and cannot be considered independently. Moreover, the conclusion was drawn [2] that emission of quanta and tunneling with a lower energy may result in a strong enhancement of barrier penetration. This conclusion is counterintuitive. Indeed, intuition is sometimes useless in description of certain quantum mechanical processes. For example, the property of nonreflectivity of some potentials [1] cannot be established on the basis of general arguments.

The strong coherence of quanta emission and tunneling is similar to the strong coherence of two stationary tunneling processes through a static double barrier potential. After tunneling through the first barrier the particle performs multiple reflections from the walls of the two barriers and then tunnels through the second barrier. Due to multiple coherent reflections, the two tunneling processes become strongly coherent and the total penetration probability dramatically increases if the particle energy E coincides with one of the energy levels E_R in the well between two barriers. Fig. 1.2 shows a typical Transmision Coefficient $T(E)$ for a double barrier system. The physical idea of this mechanism, called resonant tunneling, stems from Wigner [1]. The strong coherence between quanta emission and tunneling also results in a resonant effect and penetration probability, as a function of a particle energy E, has a sharp peak at a certain energy E_R determined by dynamical characteristics. This effect is called *Euclidean resonance* (ER) [2]. The difference between a stationary resonant tunneling through a static double barrier and Euclidean resonance in a dynamic barrier is that the former requires a long time for its formation but the latter occurs fast.

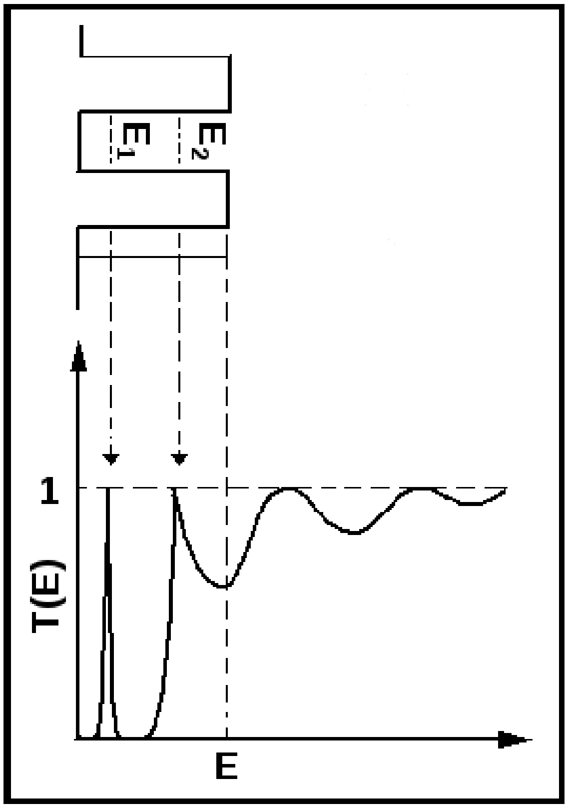

Figure 1.2: Transmission coefficient for a double barrier potential. The transmission probability increases when the energy of the incident particle is close to E_1 and E_2 and reaches its maximum for those energy levels (it is said to be in resonance).

STRUCTURAL PROPERTIES OF NANOPARTICLES

Nanotechnology is a leading interdisciplinary science that is emerging as a distinctive field of research. Its advances and applications will result in technical capabilities that will allow the development of novel nanomaterials with applications that will revolutionize the industry in many areas [3, 4]. It is now well established that dimensionality plays a critical role in determining the properties of materials and its study has produced important results in chemistry and physics [5].

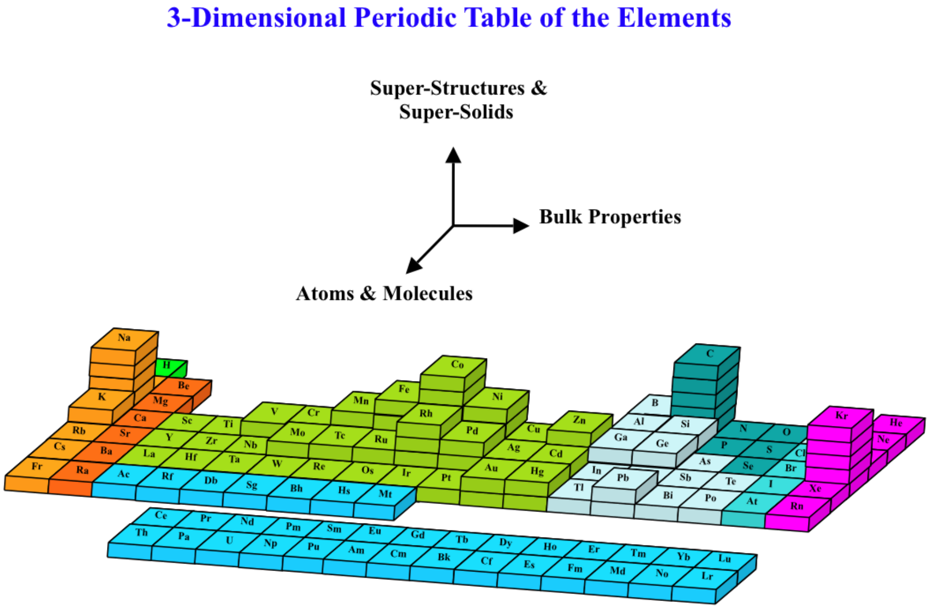

Figure 1.3: The periodic table of the elements in 3D. The first dimension represents the knowledge about atoms, molecules and low dimensional systems (surfaces and clusters); the second dimension represents the well known bulk properties of the elements. The third dimension represents jerarchical systems based on nanostructures–clusters, nanostructures and arrays of so called super-atoms–with periodicity and crystal structure, with totally new, unexpected and relevant chemical and physical properties [13].

Nanoparticles are one of the cornerstones of nanotechnology. Indeed, even when the research on this field has been going on for a long time, many present and future applications are based on nanoparticles. For instance, the electron tunneling through quantum dots has led to the possibility of fabricating single electron transistors [6–11]. One concept particularly appealing is a new three-dimensional periodic table based on the possibility of generating artificial atoms from clusters of all the elements [12]. This idea is based on the fact that several properties of nanoparticles show large fluctuations, which can be interpreted as electronic or shell closing properties with the appearance of magic numbers. Therefore, it is conceivable to tailor artificial super-atoms with given properties by controlling the number of shells on a nanoparticle. This idea is illustrated in Fig.1.3.

The development of nanotechnology can be approached from several directions; mesoscopic physics, microelectronics, materials nanotechnology and cluster science. The different fields are now coming together and a completely new area is emerging [14, 15]. Figure 1.4 illustrates how the different approaches are converging; it exhibits the domains of clusters and nanoparticles with different structures that result from an increase on the number of atoms. The different possible structures include nanorods, nanoparticles, fullerenes, nanotubes, and layered materials.

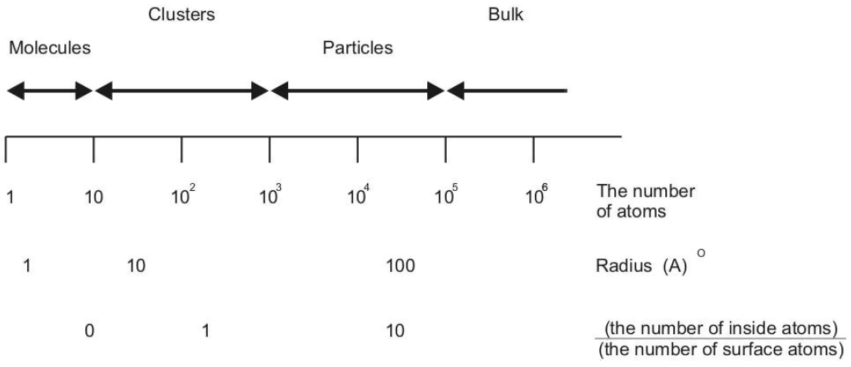

Figure 1.4: Domains of nanoparticles and clusters with different structures.

The shape of metallic nanoparticles with diameters in the region of few nanometers is a topic of extreme importance in all the research fields on nanotechnology. The atomic packing of a particle will define its surface orientation and, as a consequence, its catalytic activity, as well as the optical, mechanical, magnetic, electronic, etc., properties [16–19]. In addition, the shape of nanoparticles is strongly dependent on the preparation method [20–22], thus they can be in a metastable or even in non-equilibrium state [23, 24]. Dramatic variations in their structure can be understood in terms of the *energy landscape* concept [13], whereby many structures, or isomers, are represented in a free-energy landscape by minima of similar energies and separated by relatively small energy barriers, see the picture-concept illustrated in Fig. 1.5. This fact is clearly observed in the so called quasi-melting states, where a nanoparticle changes its shape in a very dramatic way under an electron beam, an effect that has been extensively studied by several authors and is a direct proof of the energy landscape concept [23, 24].

Now, the fundamental question of how matter properties develop from the atom to the bulk has been the subject of many studies facing the problem in so many ways and at different levels. For example, the magnetic behavior of systems with reduced dimensions are expected to have higher magnetic moments than the corresponding bulk value, mainly due to the reduced atomic coordination, thus increasing the electron localization and a correspondingly reduced valence band width. Studying small Ni_N clusters from photo-emission data, Ganteför and Eberhardt [26] have identified that the spectra corresponding to Ni clusters is surprisingly similar to small Cu_N clusters. From that point, they had outlined *the roots of magnetism*, showing how the magnetism increases in open shell metals and reduces its magnitude as the system size increases, and how the magnetism is quenched in closed shell metals.

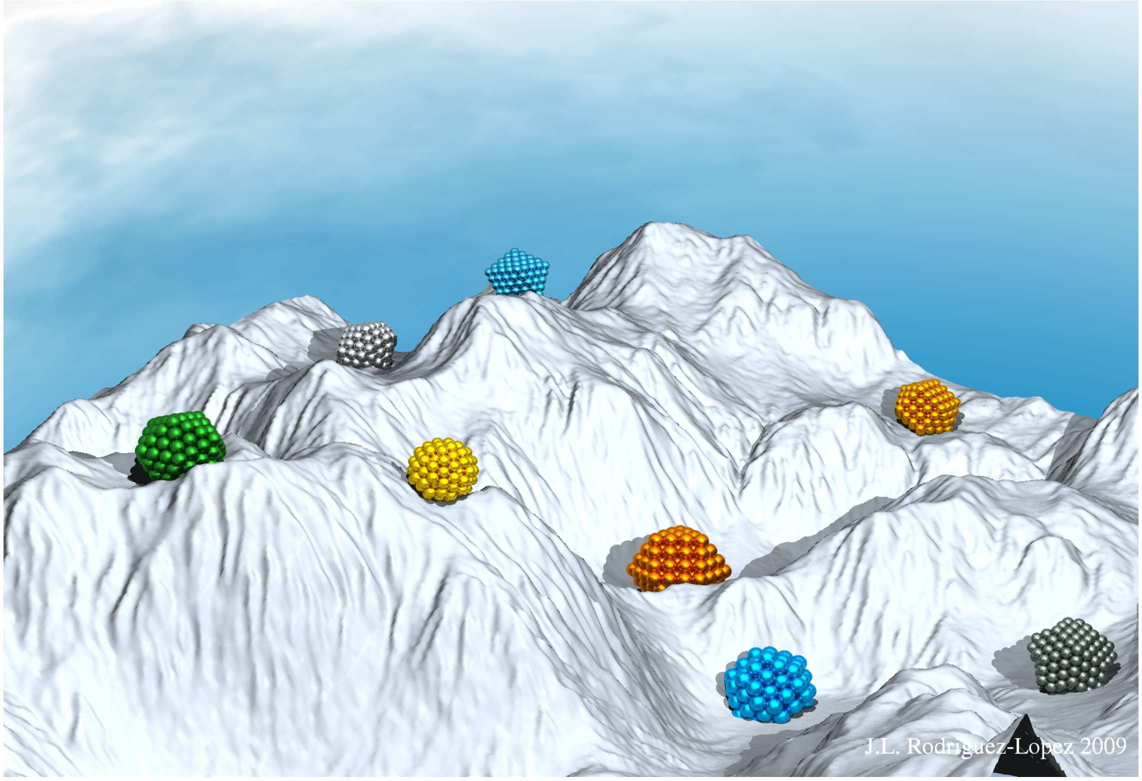

Figure 1.5: A simplified but useful cartoon for illustrating the relevant concept of surface energy landscape. Structures can be in metastable states (on maxima) or local minima, all of which can be perturbed by small amounts of energy, thus changing to another state/structure. In practice, there are many minima in the region of configurational space that a given result or a physical technique would give, but most likely is would not be the global minima.

Therefore, trying to understand the properties of a given system from its nature fundaments it is a task that worths the efforts. The sole possibility that the atomic arrangement as a function of the number of atoms presents some kind of phase diagram is an enchanting idea. To have the certainty that at a given cluster size range, and under a given set of physical conditions the majority of the particles will have a predetermined structure and symmetry, it would improve applications of nanoparticles and boost the research in nanotechnology.

This sort of phase maps or structural diagrams for small and multi-twined particles have been discussed by Cleveland and co-workers [27], Ajayan and

Marks [24], and Doye and Calvo [28]. Atomistic calculations based on the embedded atom method for the structural evolution with size of nickel clusters by Cleveland and coworkers [27] show a growth sequence of icosahedra, truncated decahedra, single closed-packed crystallites and mono-twinned particles. Marks and co-workers have summarized four primary models appeared in the literature for multi-twinned growth mechanism (see Ref. [24] and references therein), concluding that intrinsic equilibrium structures of lower energy are favored at small sizes, that undergo to phase transformations as the cluster size increases. In this sense, Doye and Calvo [28] have reported a phase diagram for Lennard-Jones clusters from thermodynamic considerations with emphasis on metallic particles, where the icosahedral and decahedral phases dominate in the small size range, and as the particle size grew up the fcc phase appears, although the phase boundaries transitions are not clear nor the thermodynamic conditions.

However, nature is still more complicated. Although, the existence of twinned and multi-twinned decahedral particles are predominant in the small size range, they co-exist with fcc and other particles, the formation rate is not uniform nor independent of the element in the cluster. There exist the possibility that the particle structures are determined statistically, an alternative path where the quasi-melting behavior would play an important role [24]. And even has been suggested the idea of the existence of symmetries and atomic arrangements different than the decahedral, icosahedral and fcc symmetry [29].

MECHANICAL PROPERTIES OF NANOPARTICLES

The strong interest in nanotechnology was first manifested from the materials science community in the early 90s. The interest was based on the change of mechanical properties with reducing the size of structures. [30–33] The rationale for the interest in the mechanical properties of nanostructures was simple: A metal with no defects can sustain elastic deformation up to 10%. Metals start to yield plastically at much lower stress. The threshold stress σ (ideal) obtained by *ab-initio* calculations is about Y/10, where Y is the *Young modulus* [34]. The real strength of a solid is reduced by the presence of defects. Plastic deformation in solids is controlled by dislocations gliding; surfaces and grain boundaries are the sink of dislocations (creating steps) and deformation will continue as long as new dislocations are created inside the crystal. The most common mechanism of dislocation creation is the Frank-Read sources [35], however, when the size of the crystal is less than 100 nm, Frank-Read sources will not be stable anymore. This opens the possibility of fabricating solids using nanoparticles that would make ultra strong materials out of soft metals. Experimental work resulted in the Hall-Petch effect, which indicated that σ (effective) $\approx kd^{-\alpha}$ where k and α are independent constants and d is the mean grain size [36]. This result confirms that it is possible to fabricate new materials with macroscopic flow strengths that are better than the conventional microstructures [37]. However, the achievement of ultra strong materials has come to the expense of ductility, thus making them very impractical in many cases. An important development was achieved by Lu *et al.* [38, 39] whom demonstrated that ductility could be increased without losing strength by introducing coherent twin boundaries. These authors reported a very unusual combination of high yield strength of 1GPa and a ductility of 14% elongation to failure, being the optimal separation between coherent twin boundaries 15 nm in length. A theoretical mechanism to explain the role of coherent twin boundaries was reported by Zhu *et al.* [40] and have also review the central role of twins on plastic deformation of nanoparticles. The experimental studies of mechanical properties of individual nanoparticles are of great interest for the full understanding of the mechanical behavior of the matter at this size regime. The experimental challenges are enormous and no direct studies have been reported. Previous experimental work on *in-situ* measurements of mechanical properties using transmission electron microscopy (TEM) has been focused on metal nanowires [41]. Zheng *et al.* have studied the plasticity in Au nanowires with a size less than 10 nm [42]. They observed that plasticity of the Au nanowires is dominated by the partial dislocations (PDs) emitted from the steps of the free surfaces; their results were consistent with previous theoretical calculations [43–46]. In the case of nanoparticles, the only experimental work that indirectly measures properties of individual nanoparticles is that of Sun *et al.* [47]. They used electron beam irradiation to induce mechanical stress on metal crystals inside graphitic nanocontainers. They concluded that the short-lived PDs nucleated by the formation of intrinsic stacking faults.

The deformation mechanisms of nanomaterials, are particularly difficult to study experimentally; for example, in high-strain-rate deformation of single crystalline fcc metals such as Cu, certain strain relaxation time scales are in the subnanosecond range [48]. Atomic-scale and other fine-scale dynamical simulation methods provide ideal means for analyzing the deformation mechanisms in ductile thin films by direct monitoring of the dynamical response of the materials at the atomic/microscopic scale [49, 50]. First-principles density functional theory calculations and large-scale molecular dynamics simulations have been used extensively toward a fundamental understanding of plastic flow initiation and nucleation of dislocations, as well as investigations of plastic deformation during nanoindentation of metal surfaces [51, 52]. Molecular dynamics simulations is important both for providing quantitative predictions of dislocation mobility, and for understanding the underlying atomistic mechanisms governing the complex plastic deformation behavior in nanosized metals [53, 54].

An interesting question is: How twinned nanoparticles respond to an applied stress, for example, in a nanoindentation experiment?. This question arises from the fact that this kind of nanoparticles, have intrinsic internal stresses due that they are formed by fcc tetrahedral units deformed in order to complete the angle needed to close them, and also it is well known that twinnings can play an important role as dislocation barriers [38, 39].

BIBLIOGRAPHY

[1] L. D. Landau and E. M. Lifshitz, *Quantum Mechanics* (Pergamon, New York, 1977).

[2] B.I. Ivlev, Tunneling through nonstationary barriers and Euclidean resonance. *Phys. Rev. A* **70**, 032110 (2004).

[3] Gross, M., *The nanoworld, Miniature Machinery in Nature and Technology.* (New York and London: Plenum Trade, 254 1999)

[4] Nalwa, H. S., *Handbook of Nanostructured Materials and Nanotechnology*. (San Diego: Academic Press, 1-4 2000)

[5] Sugano, S., Koizumi, H., *Microcluster Physics*. (Springer-Verlag, 1998)

[6] Das-Sarma, S. a. P., *Perspectives in Quantum Hall Effects*. (New York: John Wiley and Sons, 430 1997)

[7] Stormer, H. L., Fractional Quantum Hall Effect Today. *Solid State Comunications*. **107**, 617 (1998).

[8] Grabert, H., *Single Charge Tunneling*. (New York: Plenum Press. 335 1992)

[9] Dvoret, M. H., Esteve D. and Urbina, C., Single-electron transfer in metallic nanostructures. *Nature* **547** (1992).

[10] Ashoori, R. C, Electrons in artificial atoms. *Nature* **413** (1996).

[11] Alivisatos, A. P, Semiconductor Clusters, Nanocrystals, and Quantum Dots. *Science* **933** (1996).

[12] Rosen, A., *Nanostructured Materials Made from Self-Assembled Particles*, (Chalmers University of Sweeden, 2000).

[13] J. L. Rodríguez-López *et al.*, Size Effect and Shape Stability of Nanoparticles. *Key Enginering Materials* **444**, 47 (2010).

[14] Haberland, H., *Clusters of Atoms and Molecules I and II: Solvation and Chemistry of Free Clusters, Embeded, Supported and Compressed Cluster.* (Berlin, New York: Springer-Verlag, 412 1994)

[15] de Heer, W. A. The physics of simple metal clusters: experimental aspects and simple models, *Rev. Mod. Phys*. **65**, 611 (1993).

[16] W. Krakow, D.G. Ast, Surface structure and surface lattice constant of (001) vapor deposited Au films using high resolution transmission electron microscopy. *Surf. Sci*. **58**, 485 (1976).

[17] A.I. Frenkel, C.W. Hills, R. G. Nuzzo, A View from the Inside: Complexity in the Atomic Scale Ordering of Supported Metal Nanoparticles. *J. Phys. Chem. B* **105** , 12689 (2001).

[18] Y.D. Kim, M. Fisher, G. Ganteför, Origin of unusual catalytic activities of Au-based catalysts, *Chem. Phys. Lett.* **377**, 170 (2003).

[19] H.-G. Boyen, G. Kestle, F. Weigl, B. Koslowski, C. Dietrich, P. Ziemann, J. P. Spatz, S. RiethmGller, C. Hartmann, M. Müller, G. Schmid, M.G. Garnier, P. Oelhafen, *Science* **297**, 1533 (2002).

[20] F. Kim, S. Connor, H. Song, T. Kuykendall, P. Yang, Platonic Gold Nanocristals. *Angew. Chem.* **116**, 3759 (2004); *idem*, *Angew. Chem. Int. Ed.* **43**, 3673 (2004).

[21] B. Wiley, T. Herricks, Y. Sun, Y. Xia, *Nano Lett.* **4**, 1733 (2004).

[22] S. I. Stoeva, B. L. V. Prasad, S. Uma, P. K. Stoimenov, V. Zaikovski, C. M. Sorensen, K. J. Klabunde, *J. Phys. Chem. B* **107**, 7441 (2003).

[23] S. Iijima, T. Ichihashi, *Phys. Rev. Lett.* **56**, 616 (1986).

[24] (a) P.M. Ajayan, L.D. Marks, *Phys. Rev. Lett.* **60**, 585 (1988); (b) P.M. Ajayan, L.D. Marks, *Phys. Rev. Lett.* **63**, 279 (1989).

[25] L.D. Marks, *Rep. Prog. Phys.* **57**, 603 (1994).

[26] G. Ganteför, W. Eberhardt, *Phys. Rev. Lett.* **76**, 4975 (1996).

[27] U. Landman, C.L. Cleveland, *J. Chem. Phys.* **94**, 7376 (1991); C.L. Cleveland, U. Landman, M.N. Shafigullin, P.W. Stephens, R.L. Whetten, *Z. Phys. D* **40**, 503 (1997).

[28] J.P.K. Doye, F. Calvo, *Phys. Rev. Lett.* **86**, 3570 (2001).

[29] D.J. Wales, A.I. Kirkland, and D.A. Jefferson, *J. Chem. Phys.* **91**, 603 (1989).

[30] Gleiter, H., Nanocrystalline materials.*Progress in Materials Science* 1989, **33 (4)**, 223-315.

[31] Gleiter, H., Nanocrystalline solids. *Journal of Applied Crystallography* 1991, **24**, 79-90.

[32] Gleiter, H., Nanostructured materials: basic concepts and microstructure.*Acta Materialia* 2000, **48 (1)**, 1-29.

[33] Suryanarayana, C.; Koch, C. C., Nanocrystalline materials - Current research and future directions. *Hyperfine Interactions* 2000, **130 (1)**, 5-44.

[34] Pokluda, J.; Cerny, M.; Sandera, P.; Sob, M., Calculations of theoretical strength: State of the art and history. *Journal of Computer-Aided Materials Design* 2004, **11 (1)**, 1-28.

[35] Hirth, J. P. a. L. J., *Theory of dislocations*. (Mcgraw Hill: New York, 1968).

[36] Courtney, T. H., *Mechanical Behavior of Materials*. 2nd ed.; (McGraw Hill: Boston, 2000).

[37] Zhu, T.; Li, J., Ultra-strength materials. *Progress in Materials Science* 2010, **55 (7)**, 710-757.

[38] Lu, L.; Chen, X.; Huang, X.; Lu, K., Revealing the maximum strength in nanotwinned copper. *Science* 2009, **323** , 607-610.

[39] Lu, L.; Shen, Y.; Chen, X.; Qian, L.; Lu, K., Ultrahigh strength and high electrical conductivity in copper.*Science* 2004, **304**, 422-426.

[40] Zhu, Y. T.; Liao, X. Z.; Wu, X. L., Deformation twinning in nanocrystalline materials. *Progress in Materials Science* 2011, **57 (1)**, 1-62.

[41] Wang, Z. L.; Gao, R. P.; Pan, Z. W.; Dai, Z. R., Nano-scale mechanics of nanotubes, nanowires, and nanobelts. *Advanced Engineering Materials* 2001, **3 (9)**, 657-661.

[42] Zheng, H.; Cao, A.; Weinberger, C. R.; Huang, J. Y.; Du, K.; Wang, J.; Ma, Y.; Xia, Y.; Mao, S. X., Discrete plasticity in sub-10-nm-sized gold crystals.*Nat. Commun.* 2010, **1 (9)**, 144.

[43] Agrait, N., Rubio, G. and Vieira, S., Plastic deformation of nanometer-scale gold connective necks. *Physical Review Letters* 1995, **74 (20)**, 3995-3992.

[44] Deng, C.; Sansoz, F., Near-ideal strength in gold nanowires achieved through microstructural design. *ACS Nano* 2009, **3 (10)**, 3001-3008.

[45] Diao, J.; Gall, K.; L. Dunn, M., Atomistic simulation of the structure and elastic properties of gold nanowires. *Journal of the Mechanics and Physics of Solids* 2004, **52 (9)**, 1935-1962.

[46] Ji, C. P., H. S., Geometric effects on the inelastic deformation of metal nanocrystals.*Applied Physics Letters* 2006, **89**, 181916.

[47] Sun, L.; Krasheninnikov, A. V.; Ahlgren, T.; Nordlund, K.; Banhart, F., Plastic deformation of single nanometer-sized crystals.*Physical Review Letters* 2008, **101 (15)**, 156101.

[48] A. Loveridge-Smith *et al.*, *Phys. Rev. Lett.* **86**, 2349 (2001).

[49] V. V. Bulatov, F. F. Abraham, L. Kubin, B. Devincre, and Y. Yip, *Nature*, **391**, 669 (1998).

[50] F. F. Abraham, *Adv. Phys*. **52**, 727 (2003).

[51] J. Li, K. J. Van Vliet, T. Zhu, S. Yip, and S. Suresh, *Nature* **418**, 307 (2002).

[52] E. T. Lilleodden, J. A. Zimmerman, S. M. Foiles, and W. D. Nix, *J. Mech. Phys. Solids* **51**, 901 (2003).

[53] M.S. Duesbery, V. Vitek, Plastic anisotropy in BCC transition metals, *Acta Mater.* **46**, (1998) 1481.

[54] V.V. Bulatov, L.P. Kubin, Curr. Opin. *Solid State Mater. Sci.* **3**, (1998) 558.

CHAPTER 2

THEORY

The purpose of this chapter, is to remember and describe some of the basic concepts and theory that were needed for the development of the present thesis work.

2.1 WKB THEORY

The WKB (Wentzel, Kramers, Brillouin) approximation is, in sense to be made clear below, a quasi-classical method for solving the one-dimensional (and effectively one-dimensional, such as radial) time-independent Schrödinger equation. The nontrivial step in the method is the connection formulas, that problem was first solved by Lord Rayleigh [1] and as Jeffries notes [2] "it has been rediscovered by several later writers" presumable referring to W., K. and B.

2.1.1 THE SEMICLASSICAL APPROXIMATION TO LEADING ORDER

Consider a particle moving along in a slowly varying one-dimensional potential. By "slowly varying" we mean here that in any small region the wave function is well approximated by a plane wave, and that the wavelength only changes over distances long compared with a wavelength. We are also assuming for the moment that the particle has positive kinetic energy in that region. Under these conditions, it is easy to see the general form of the solution to the time independent Schrödinger equation

$$\frac{-\hbar^2}{2m}\frac{\partial\psi(x)}{\partial x^2} + V(x)\psi(x) = E\psi(x). \tag{2.1}$$

Very approximately, $\psi(x)$ will look like $A(x)e^{\pm ip(x)x/\hbar}$ where $p(x)$ is the "local momentum" defined classically by

$$\frac{p(x)}{2m} + V(x) = E, \tag{2.2}$$

and $A(x)$ is slowly varying compared with the phase factor. Clearly this is a semiclassical limit: has to be sufficiently small that there are many oscillations in the typical distance over which the potential varies. To handle this a little more precisely, we emphasize the rapid phase variation in this semiclassical limit by writing the wave function

$$\psi(x) = e^{\frac{i}{\hbar}\sigma(x)}. \tag{2.3}$$

and writing Schrödinger's equation for $\sigma(x)$. So from

$$i\hbar\psi'(x) = -\sigma'(x)e^{\frac{i}{\hbar}\sigma(x)}, \tag{2.4}$$

and

$$-\hbar^2\psi''(x) = -i\hbar\sigma''(x)e^{\frac{i}{\hbar}\sigma(x)} + (\sigma'(x))^2e^{\frac{i}{\hbar}\sigma(x)}, \tag{2.5}$$

Schrödinger's equation written for the phase function is:

$$-i\hbar\sigma''(x) + (\sigma'(x))^2 = (p(x))^2. \tag{2.6}$$

Since we are assuming the system is close to classical, it makes sense to expand σ as a series in $\hbar$:

$$\sigma = \sigma_0 + \left(\frac{\hbar}{i}\right)\sigma_1 + \left(\frac{\hbar}{i}\right)^2\sigma_2 + ... \tag{2.7}$$

The zeroth order approximation is

$$(\sigma_o')^2 = p^2 \tag{2.8}$$

and fixing the sign of p by

$$p(x) = +2m\sqrt{(E - V(x))} \tag{2.9}$$

we conclude that

$$\sigma_o = \pm \int p(x)dx. \tag{2.10}$$

2.1.2 REGION OF VALIDITY OF THE APPROXIMATION

From the Schrödinger equation 3.10, it is evident that this approximate solution is only valid if we can ignore that first term. That is to say, we must have

$$|\hbar\sigma''(x)/(\sigma'(x))^2| \ll 1, \tag{2.11}$$

or

$$\left|\frac{d(\hbar/\sigma')}{dx}\right| \ll 1. \tag{2.12}$$

But in leading approximation $\sigma' = p$, and $p = 2\pi\hbar/\lambda$, so the condition is

$$\frac{1}{2\pi}\left|\frac{d\lambda}{dx}\right| \ll 1. \tag{2.13}$$

This just means the change in wavelength over a distance of one wavelength must be small. Obviously, this cannot always be the case: if the particle is confined by an attractive potential, at the edge of the classically allowed region, that is, where $E = V(x)$, p is zero and the wavelength is infinite. The approximation is only good well away from that point.

2.1.3 NEXT TO LEADING CORRECTION

The second term in the expansion of the phase, $\sigma = \sigma_0 + (\hbar/i)\sigma_1 + ...$ satisfies

$$-i\hbar\sigma_0'' + 2\sigma_0'\frac{\hbar}{i}\sigma_1' = 0 \tag{2.14}$$

so

$$\sigma_1' = -\frac{\sigma_0''}{2\sigma_0'} = -\frac{p'}{2p}, \tag{2.15}$$

and

$$\sigma_1 = -\frac{1}{2} = \ln p. \tag{2.16}$$

Therefore the wave function to this order is:

$$\psi(x) = \frac{C_1}{\sqrt{p(x)}} e^{\frac{i}{\hbar}\int p dx} + \frac{C_2}{\sqrt{p(x)}} e^{-\frac{i}{\hbar}\int p dx}. \tag{2.17}$$

To interpret the $p(x)$ factor, consider the first term, a wave moving to the right. Since p is real, the exponential has modulus unity, and the local amplitude squared is proportional to $1/p$, that is, $1/v$, where v is the velocity of the particle. This is simple to understand physically: the probability of finding the particle in any given small interval is proportional to the time it spends there, hence inversely proportional to its speed. We turn now to the wave function in the classically forbidden region,

$$\frac{p(x)^2}{2m} = E - V(x) < 0. \tag{2.18}$$

Here p is of course pure imaginary, but the same formal phase solution of the Schrödinger equation works, again provided that the particle is well away from the points where $E = V(x)$. The wave function is:

$$\psi(x) = \frac{C_1'}{\sqrt{|p(x)|}} e^{-\frac{1}{\hbar}\int |p| dx} + \frac{C_2'}{\sqrt{|p(x)|}} e^{\frac{1}{\hbar}\int |p| dx}. \tag{2.19}$$

2.1.4 CONNECTION FORMULAS, BOUNDARY CONDITIONS AND QUANTIZATION RULES

Let us assume we are dealing with a one-dimensional potential, and the classically allowed region is $b \le x \le a$. Clearly, in the forbidden region to the right, $x > a$, only the first term in the above equation for $\psi(x)$ appears, and for $x < b$ only the second term. Furthermore, in the "inside" (classically allowed) region, $b \le x \le a$, the wave function has the oscillating form discussed earlier. But how do we connect the three regions together? We make an assumption: we take it that the potential varies sufficiently smoothly that it is a good approximation to take it to be linear in the vicinity of the classical turning points. That is to say, we assume that a linear potential is a sufficiently good approximation out to the point where the short wavelength (or decay length for tunneling regions) description is adequate. Therefore, near $x = a$, we take the potential to be

$$E - V(x) \cong F_o(x - a) \tag{2.20}$$

(so F_0 would be the force) and then approximate the wave function by the known exact solution for a linear everywhere potential: the Airy function. It is known that for the Airy function, the solution having the form [3]

$$\psi(x) = \frac{C}{2\sqrt{|p(x)|}} e^{-\frac{1}{\hbar}\int_a^x |p| dx} \tag{2.21}$$

to the right becomes

$$\psi(x) = \frac{C}{\sqrt{|p(x)|}} \cos\left(\frac{1}{\hbar}\int_a^x p dx + \frac{\pi}{4}\right) = \frac{C}{\sqrt{|p(x)|}} \sin\left(\frac{1}{\hbar}\int_x^a p dx + \frac{\pi}{4}\right), \tag{2.22}$$

for $x < a$. At b, the same argument gives

$$\psi(x) = \frac{C}{\sqrt{|p(x)|}} \sin\left(\frac{1}{\hbar}\int_b^x p dx + \frac{\pi}{4}\right). \tag{2.23}$$

For these two expressions to be consistent, we must have

$$\int_b^a p dx + \frac{\pi}{2} = (n+1)\pi, \tag{2.24}$$

or

$$\oint p dx = 2\pi\hbar\left(n + \frac{1}{2}\right). \tag{2.25}$$

where the latter integral is over a complete cycle of the classical motion. Here n is the number of zeros of the wave function: this is the *quantization condition*.

2.2 PHOTON-ASSISTED TUNELING

A penetration of a particle through a potential barrier is forbidden in classical mechanics. Only due to quantum effects the probability of passing across a barrier becomes finite and it can be calculated on the basis of WKB approach, which is also called the semiclassical theory. The transition probability through the barrier, shown in Fig. 2.1, is

$$W \sim \exp\left[-A_0(E)\right] \tag{2.26}$$

where

$$A_0(E) = \frac{2}{\hbar}\int dx\sqrt{2m\left[V(x) - E\right]} \tag{2.27}$$

is the classical action measured in units of $\hbar$. The integration goes under the barrier between two classical turning points where $V(x) = E$. One can use the general estimate $A_0 \sim V/\hbar\omega$, where V is the barrier height and ω is the frequency of classical oscillations in the potential well. A semiclassical barrier relates to a big value $V/\hbar\omega \gg 1$.

What happens when the static potential barrier $V(x)$ is acted by a weak non-stationary electric field $\mathcal{E}(t)$? In this case there are two possibilities for barrier penetration: (i) the conventional tunneling, which is not affected by $\mathcal{E}(t)$, shown by the dashed line in Fig. 2.1, and (ii) an absorption of the quantum $\hbar\Omega$ of the field $\mathcal{E}(t)$ and subsequent tunneling with the new energy $E + \hbar\Omega$. The latter process is called photon-assisted tunneling. The total probability of penetration across the barrier can be schematically written as a sum of two probabilities

$$W \sim \exp\left(-\frac{V}{\hbar\omega}\right) + \left(\frac{a\mathcal{E}_\Omega}{\hbar}\right)^2 \exp\left(-\frac{V - \hbar\Omega}{\hbar\omega}\right) \tag{2.28}$$

where $\mathcal{E}_\Omega$ is the Fourier component of the field $\mathcal{E}(t)$ and the length a is a typical barrier extension in space. The second term in Eq. (2.28) relates to photon-assisted tunneling and it is a product of probabilities of two quantum mechanical processes: absorption of the quantum $\hbar\Omega$ and tunneling through the reduced barrier $V - \hbar\Omega$.

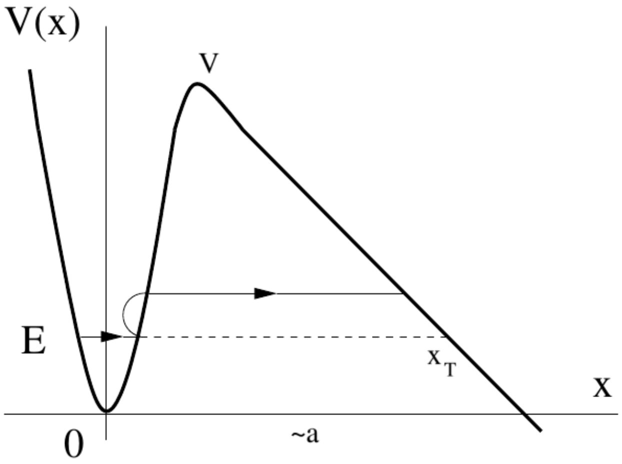

Figure 2.1: The path of tunneling is denoted by the dashed line. x_T is the classical turning point. E is the energy of the metastable state, V is the barrier height, and a is the typical potential length. The particle can absorb a quantum and tunnel in a more transparent part of the barrier with the energy $E + \hbar\Omega$.

2.3 TRAJECTORIES IN IMAGINARY TIME

According to Feynman [4], when the phase of a wave function is big, it can be expressed through classical trajectories of the particle. But in our case there are no conventional trajectories since a classical motion is forbidden under a barrier. Suppose a classical particle to move in the region to the right of the classical turning point x_T in Fig. 2.1 and to reach this point at $t = 0$. Then, close to the point x_T, $x(t) = x_T + ct^2$ ($c > 0$) and there is no a barrier penetration as at all times $x(t) > x_T$. Nevertheless, if t is formally imaginary, $t = i\tau$, the penetration becomes possible since $x(i\tau) = x_T - c\tau^2$ is less then x_T. Therefore, one can use classical trajectories in imaginary time to apply Feynman's method to tunneling. In the absence of a nonstationary field a classical trajectory satisfies Newton's equation in imaginary time

$$m\,\frac{\partial^2 x}{\partial \tau^2} = \frac{\partial V(x)}{\partial x} \tag{2.29}$$

where $V(x)$ is the static barrier in Fig. 2.1. The classical turning point x_T in Fig. 2.1 is reached at $\tau = 0$ with the initial condition $\partial x/\partial\tau = 0$. The classical trajectory $x = x(\tau)$ can be considered as a change of variables $x \to \tau$ in the WKB exponent (2.27) when it becomes of the form

$$A_0 = \frac{2}{\hbar}\int d\tau \left[\frac{m}{2}\left(\frac{\partial x}{\partial\tau}\right)^2 + V(x) - E\right] \tag{2.30}$$

So, in the absence of a non-stationary field, use of classical trajectories in imaginary time is obvious and it is simply reduced to a change of variable.

2.4 MOLECULAR DYNAMICS

Molecular Dynamics simulation is a technique for computing the equilibrium and transport properties of a classical many-body system. In this context, the word *classical* means that the nuclear motion of the constituent particles obeys the laws of classical mechanics. This is an excellent approximation for a wide range of materials.

In a Molecular Dynamics simulation, we follow exactly the same approach as in a real experiment. First, we prepare the sample: we select a model system consisting of N particles and we solve Newton's equations of motion for this system until the properties of the system no longer changes with time (we equilibrate the system). After equilibration, we perform the actual measurement.

To measure an observable quantity in a Molecular Dynamics simulation, we must first of all be able to express this observable as a function of the positions and momenta of the particles in the system. For instance, a convenient definition of the temperature in a (classical) many-body system makes use of the equipartition of energy over all degrees of freedom that enter quadratically in the Hamiltonian of the system. In particular for the average kinetic energy per degree of freedom, we have

$$\left\langle \frac{1}{2} m v_\alpha^2 \right\rangle = \frac{1}{2} k_B T. \tag{2.31}$$

In a simulation, we use this equation as an operational definition of temperature. In practice, we would measure the total kinetic energy of the system and divide this by the number of dregrees of freedom $N_f (= 3N - 3)$ for a system of N particles with fixed total momentum). As the total kinetic energy of a system fluctuates, so does its instantaneous temperature:

$$T(t) = \sum_{i=1}^{N} \frac{m_i v_i^2(t)}{k_B N_f}. \tag{2.32}$$

The relative fluctuations in the temperature will be of order $1/N_f$. As N_f is typically on the order of $10^2 - 10^3$, the statisticall fluctuations in the temperature are on the order of $5 - 10\%$. To get an accurate estimate of the temperature, one should average over many fluctuations [5].

2.4.1 BASIC APPROACH

The essential elements for a Molecular Dynamics simulation are (i) the interaction potential (i.e., potential energy) for the particles, from which the forces can be calculated, and (ii) the equations of motion governing the dynamics of the particles. We follow the laws of classical mechanics, mainly Newton's law

$$\mathbf{F}_i = m_i \mathbf{a}_i. \tag{2.33}$$

for each atom i in a system constituted by N atoms. Here, m_i is the atom mass, $\mathbf{a}_i$ its acceleration and $\mathbf{F}_i$ the force acting upon it due to the interactions with the other atoms. Equivalently one can solve classical Hamiltonian equation of motion

$$\dot{\mathbf{p}}_i = -\frac{\partial H}{\partial \mathbf{r}_i}, \tag{2.34}$$

$$\dot{\mathbf{r}}_i = \frac{\partial H}{\partial \mathbf{p}_i}, \tag{2.35}$$

where $\mathbf{p}_i$ and $\mathbf{r}_i$ are the momentum and position coordinates for the *ith* atom. H, the Hamiltonian, which is defined as a function of position and momenta, is given by

$$H(\mathbf{p}_i, \mathbf{r}_i) = \sum_{i=1}^{N} \frac{\mathbf{p}_i^2}{2m_i} + V(\mathbf{r}_i). \tag{2.36}$$

The force on an atom can be calculated as the derivative of energy with respect to the change in the atom's position

$$\mathbf{F}_i = m_i \mathbf{a}_i = -\nabla_i V = -\frac{dE}{d\mathbf{r}_i}. \tag{2.37}$$

Knowledge of the atomic forces and masses can then be used to solve for the positions of each atom along a series of extremely small time steps (on the order of femtoseconds). The velocities are calculated from the accelerations

$$\mathbf{a}_i = \frac{d\mathbf{v}_i}{dt}. \tag{2.38}$$

Finally, the positions are calculated from the velocities

$$\mathbf{v}_i = \frac{d\mathbf{r}_i}{dt}. \tag{2.39}$$

To summarize the procedure, at each step, the forces on the atoms are computed and combined with the current positions and velocities to generate new positions and velocities a short time ahead. The force acting on each atom is assumed to be constant during the time interval. The atoms are then moved to the new positions, an updated set of forces is computed and new dynamics cycle goes on. Usually molecular dynamics simulations scale by either $O(N\ log\ N)$ or $O(N)$, with N as the number of atoms. This makes simulations with macroscopic number of atoms or molecules ($\sim 10^{23}$) impossible to handle with MD. Therefore, statistical mechanics is used to extract the macroscopic information from the microscopic information provided by MD. Two important properties of the equations of motion should be noted. One is that they are time reversible, i.e., they take the same form when the transformation $t \rightarrow t$ is made. The consequence of time reversal symmetry is that the microscopic physics is independent of the direction of the flow of time. Molecular dynamics calculates the real dynamics, i.e. the behavior of the system, from which the time average of the system's properties can be calculated. The second important property of the equations of motion is that they conserve the Hamiltonian. This can be easily seen by computing the time derivative of H and substituting 2.34 and 2.35 for the time derivatives of position and momentum

$$\frac{dH}{dt} = \sum_{i=1}^{N}\left[\frac{\partial H}{\partial \mathbf{r}_i}\dot{\mathbf{r}}_i + \frac{\partial H}{\partial \mathbf{p}_i}\dot{\mathbf{p}}_i\right] = \sum_{i=1}^{N}\left[\frac{\partial H}{\partial \mathbf{r}_i}\frac{\partial H}{\partial \mathbf{p}_i} - \frac{\partial H}{\partial \mathbf{p}_i}\frac{\partial H}{\partial \mathbf{r}_i}\right] = 0. \tag{2.40}$$

The conservation of the Hamiltonian is equivalent to the conservation of the total energy of the system and provides an important link between molecular dynamics and statistical mechanics [**?**].

2.5 EMBEDDED ATOM METHOD

As we have seen in the previous section, one of the essential elements for a Molecular Dynamics simulation is the interaction potential for the particles. Because we are interested in phenomena such as growth for noble metals clusters, the calculation scheme adopted for this study was the embedded atom method (EAM [7, 8]). It is known that EAM is able to give reasonable physical trends and reliable calculated properties of noble metal bulk systems.

The embedded atom method evaluates the effective interactions between two atoms depending of the environment where they are inside the system, $i.e.$, the study is more than only a pair potential approximation. The EAM is related to the mean field theory, it replaces the problem of the cohesive energy of N-atoms into a metallic system, by the sum of the interacting energies of each one of the atoms in the system, with a host matrix that simulates the effects of the other $N-1$ atoms. The density of electrons is the physical quantity responsible of the interaction because these methods are based on the Functional Density Theory [6].

Daw and Baskes [7,8] proposed the idea of to consider each atom in a metallic system as an impurity in a host formed by all the other atoms. The bonding energy for this system is

$$E_B = \sum_i \left[F_i(\bar{\rho}_i) + \frac{1}{2} \sum_{i \neq j} \phi_{ij}(R_{ij}) \right] , \tag{2.41}$$

where F_i is the energy required to embedd the atom i inside the electronic density $\bar{\rho}_i$ in the site i, and $\phi_{ij}(R_{ij})$ is the interaction between the core of the ith-atom and the core of the jth-atom that are separated a distance R_{ij}. The approximation to the host electronic density $\bar{\rho}_i$ is made by a superposition of the mean spherical average of the electronic densities of the atoms that surround the ith-atom, and is given by

$$\bar{\rho}_i = \sum_{j(\neq i)} \rho_j(R_{ij}) , \tag{2.42}$$

where $\rho_j(R_{ij})$ is the electronic density of the jth-atom in the position of the core of the ith-atom. The functions F_i and ϕ_{ij} were empirically obtained by Daw and Baskes [8] from the physical properties of the solid, although they can be obtained from first principles methods [9]. In the Foile's version of the EAM [10], the function $\phi_{ij}(R)$ that describe the core-core interaction is given by

$$\phi_{ij}(R) = \frac{Z_0^2 (1 + \beta R^{\nu})^2 e^{-2\alpha R}}{R} , \tag{2.43}$$

where Z_0 is the number of external electrons of the atom and α, β and ν are some adjustable parameters.

The atomic densities are obtained from the Hartree-Fock atomic calculation of Clementi and Rosetti [11] and MacLean and MacLean [12],

$$\rho(R) = n_s \rho_s(R) - (n - n_s)\rho_d(R) , \tag{2.44}$$

being n the total number of external electrons ($s + d$), n_s is the number of external electrons s, and ρ_s and ρ_d are the partial densities associated with the wave functions s and d, respectively. Knowing the atomic densities $\rho(R)$ and the pair interactions $\phi(R)$, it can be defined in a unique way, the embedding energy adjusting the total energy given by Eq. (2.41) to the equation of state of Rose *et al.* [13] for a wide set of values of the lattice parameters. In this way the functional $F_i(\rho)$ is obtained in a numerical form.

2.6 DISLOCATIONS THEORY

Dislocations are crystal defects; lines along which and in the vicinity of which the regular arrangement of the atomic planes characteristic for the crystal is disrupted. Dislocations and other crystal defects determine many physical properties of crystals; such properties are called structurally sensitive properties. In particular, the mechanical properties of crystals such as strength and plasticity are caused by the existence of dislocations and by their special features.

2.6.1 TYPES OF DISLOCATIONS

The simplest types of dislocations are edge and screw dislocations. In an ideal crystal, the neighboring atomic planes are parallel over their entire width, but in a real crystal, the atomic planes frequently terminate within the crystal (Fig. 2.2 a), which gives rise to an edge dislocation, whose axis is the edge of the "extra" plane. The use of electron microscopes of high resolving power makes it possible to observe the arrangement of the atomic rows in some crystals that is characteristic of edge dislocation.

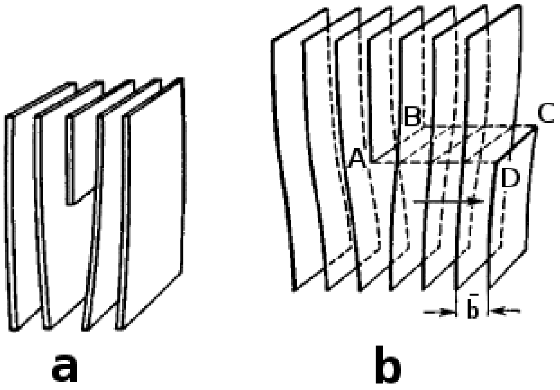

Figure 2.2: Edge dislocation: (a) Disruption of the atomic plane within the crystal, (b) diagram of the formation of an edge dislocation.

The formation of edge dislocations may be imagined by cutting the crystal along part of the plane **ABCD** (Fig. 2.2 **b**), displacing the lower part with respect to the upper part by one atomic distance **b** in the direction perpendicular to **AB**, and then again joining the atoms at the opposite sides of the cut. The remaining extra plane terminates along the edge dislocation **AB**. The vector $\vec{b}$, whose magnitude is equal to the interatomic distance, is called the characteristic slip vector (known as $Burgers\ vector$). The plane passing through the slip vector and the line of dislocation is called the glide plane for the edge dislocation.

If the slip direction $\vec{b}$ is parallel rather than perpendicular to the boundary **AB** of the cut, a screw dislocation results (Fig. 2.3 **a**). In contrast to the edge dislocation, the glide plane for a screw dislocation may be any crystallographic plane passing through the line **AB**. A crystal with a screw dislocation no longer consists of parallel atomic planes but should be regarded as consisting of a single atomic plane twisted into the shape of a helicoid, or spiral staircase without steps (Fig. 2.3 **b**). The Fig. 2.3 **c** shows the arrangement of atoms above (open circles) and below (solid circles) the glide plane in a simple cubic lattice with a screw dislocation. If the screw dislocation emerges at the external surface of the crystal, then the step **AD**, one atomic layer in height, is terminated at the point of emergence **A** (Fig. 2.3 **b**).

This step plays an active role during the crystallization process. Atoms of material precipitating from the vapor phase or solution readily add to the step at the surface of the growing crystal. The number of atoms included in the step and the rate of displacement of the step at the crystal surface are greater in the area of the emergence of the dislocation; therefore, the step is twisted about the axis of the dislocation. The step gradually rises from one crystal "level" to another, which leads to the spiral growth of the crystal.

Between the extreme cases of pure edge and screw dislocations, many intermediate cases are possible in which the dislocation line forms an arbitrary angle with the slip vector (mixed dislocation). The dislocation line must not necessarily be straight; it may be an arbitrary curve. The dislocation lines cannot terminate within the crystal. They must be closed, forming a loop; branched, to give several dislocations; or emerging at the surface of the crystal. The dislocation density in a crystal is defined as the average number of dislocation lines intersecting an area of 1 cm^2 drawn within the body. The dislocation density usually varies from 10^2 to 10^3 per cm^2 in the most perfect single crystals and reaches $10^{11} - 10^{12}$ per cm^2 in strongly distorted (work-hardened) metals.

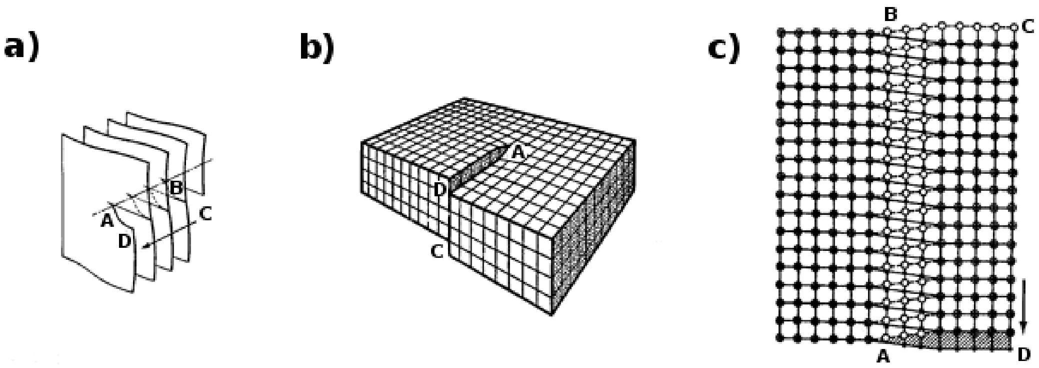

Figure 2.3: Screw dislocation: (a) Diagram of the formation of a screw dislocation, (b) arrangement of atoms in a crystal with a screw dislocation (atoms are located at the corners of the cubes), (c) arrangement of atoms in the glide plane of the screw dislocation.

2.6.2 DISLOCATIONS AS SOURCES OF INTERNAL STRESSES

The regions of the crystal in the vicinity of dislocations are in an elastically stressed state. The stresses decrease in inverse proportion to distance from the dislocation. The stress fields of the individual dislocations are made visible (in transparent crystals with low dislocation density) by polarized light. Depending on the orientation of the glide vectors of two dislocations, they may be either repelled or attracted. The approach of two dislocations with the same glide vectors (Fig. 2.4 **a**) increases the compression of the crystal on one side of the glide plane and the stretching of the crystal on the other side of the glide plane. The approach of dislocations with opposite slip vectors leads to a compensation of the stretching and compression on both sides of the glide plane (Fig. 2.4 **b, c, d**).

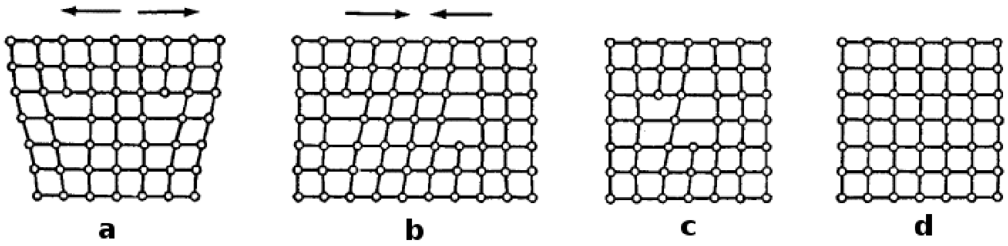

Figure 2.4: (a) and (b) Attracting and repelling dislocations; (c) and (d) annihilation of attracting dislocations.

The magnitude of the elastic energy caused by the dislocation stress field is proportional to b^2.

2.6.3 MOTION OF DISLOCATIONS.

Dislocations can move within the crystal, causing plastic deformation. Motion of the dislocation in the glide plane is called glide. Glide of a single dislocation through the crystal leads to a plastic shear by one interatomic distance b (Fig. 2.5). Upon displacement of a dislocation within the glide plane, interatomic bonds are broken and re-formed at any given moment not between all of the atoms in the glide plane (Fig. 2.5 **a**) but only between the atoms located near the axis of the dislocation (Fig. 2.5 **b**). For this reason, dislocation glide occurs at relatively small external stresses. These stresses are several orders of magnitude lower than the stress leading to a plastic deformation of a perfect crystal without dislocations (theoretical shear strength). Filament crystals (whiskers) without dislocations may have shear strengths approaching the theoretical.

Motion of an edge or mixed dislocation in the direction perpendicular to the glide plane is called climb. It occurs as a result of the diffusion of atoms, or the movement of vacancies in opposite directions, from the crystal toward the edge of the extra plane forming the dislocation (Fig. 2.6). Since the rate of diffusion de-

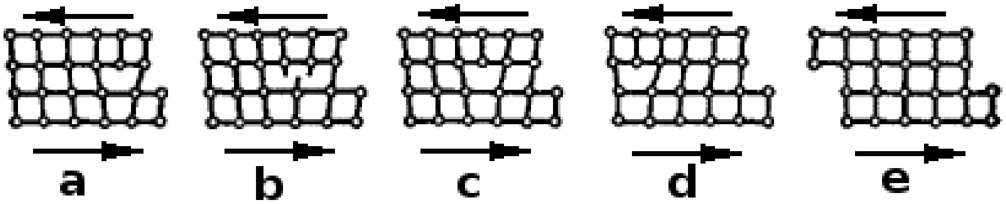

Figure 2.5: Motion of a dislocation in the glide plane is accompanied by rupture and reformation of the interatomic bonds. In a dislocation-free crystal, shear in the glide plane requires simultaneous rupture of all interatomic bonds.

creases very sharply (exponentially) with decreasing temperature, climb occurs with appreciable velocity only at rather high temperatures. If the crystal containing the dislocation is under load, the fluxes of atoms and vacancies are directed in such a way that the elastic stresses are minimized. This results in plastic deformation of the crystal caused not by glide but by climb of the dislocation. Thus, the plastic deformation of a crystal with a dislocation is always motion of the dislocation. In this case the rate of plastic deformation of the crystal is found to be directly proportional to the density of moving dislocations and to their mean velocity. Plastic deformation of a crystal without dislocations occurs through diffusion of point defects.

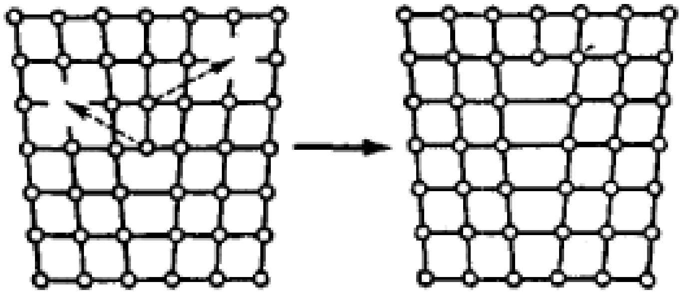

Figure 2.6: Climb of an edge dislocation. Atoms of the extra plane migrate to the vacant lattice points.

2.6.4 MOBILITY OF DISLOCATIONS.

Glide of dislocations is resisted not only by the strength of the interatomic bonds that are being broken but also by the scattering of the thermal oscillations of atoms and conduction electrons (in metals) in the elastically distorted region of the crystal surrounding the moving dislocation, by elastic interaction with other dislocations and with atoms of impurity elements in solid solutions, by grain boundaries in polycrystals, and by particles of another phase in separating alloys (twins). Part of the work of external forces is expended on overcoming these obstacles; as a result, the fewer defects the crystal contains, the greater the dependence of the mobility of dislocations on the lattice structure. The rate of dislocation glide increases sharply with stress but does not exceed the speed of propagation of sound in the crystal. The rate of climb is proportional to the stress.

2.6.5 FORMATION AND DISAPPEARANCE OF DISLOCATIONS.

Dislocations usually arise during the formation of crystals from melts or gaseous phase. Methods of growing single crystals containing no dislocations at all are very complex and have been developed only for a few crystalline materials. After careful annealing, the crystals usually contain $10^4 - 10^5$ dislocations per cm^2. The smallest plastic deformation of such a crystal leads to an intensive ”multiplication” of dislocations (Fig. 2.7), without which significant plastic deformation of the crystal is impossible. If new dislocations were not generated within the crystal, the deformation would terminate after the emergence onto the surface of all dislocations present in the crystal.

Attracting dislocations with opposing glide vectors, located in the same glide plane, annihilate each other on approach (Fig. 2.4 **b, c, d**). If such dislocations are located in different glide planes, climb is required for their annihilation. For this reason, high-temperature annealing, which favors climb, lowers the density of dislocations.

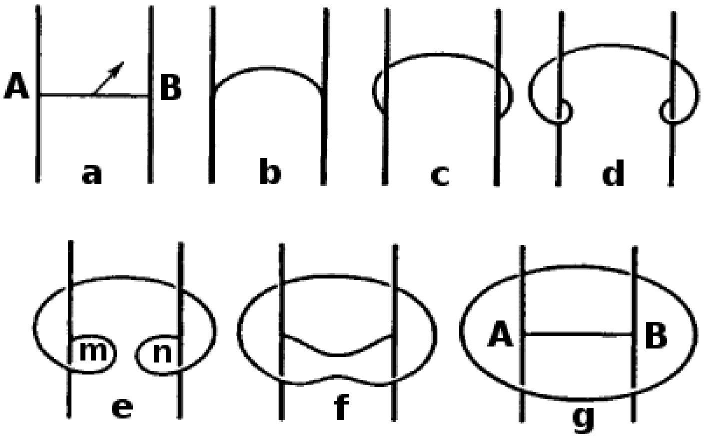

Figure 2.7: Diagram of a Frank-Read dislocation source. A section of the dislocation is fixed at points A and B. The section is bent under the influence of the external force (arrow) and successively assumes configurations (a) through (g) until the closed dislocation loop is separated, with the regeneration of the initial section AB. The attracting regions m and n of the loop undergo annihilation at stage (f).

2.6.6 DISLOCATIONS AS A SOURCE OF LATTICE CURVATURE.

Crystal regions separated by rows of dislocations (Fig. 2.8 **a**) or by dislocation networks have a different orientation of the atomic planes and are called crystalline blocks (grains). If dislocations are uniformly distributed throughout the crystal volume, the block structure does not exist, but the lattice is curved (Fig. 2.8 **b**).

The curvature of the atomic planes and distortion of the interplane distances near dislocations increase the intensity of X-ray and electron scattering. This is the basis of the X-ray and electron-microscope methods for the study of dislocations.

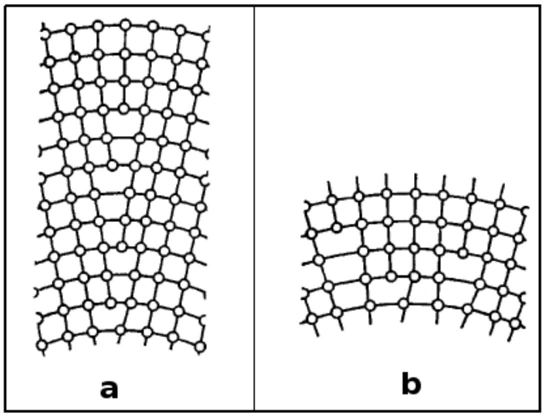

Figure 2.8: a) Dislocations forming a grain boundary. b) Bent crystal.

2.6.7 DISLOCATION STRUCTURE OF DEFORMED CRYSTALS: FRACTURE.

The distribution of dislocations in deformed crystals is usually nonuniform. At a low degree of deformation (usually up to 10%), dislocations are frequently located along selected glide planes. An increase in deformation generates (usually in metals) a block structure, which may be detected with an electron microscope or by X-ray scattering. The size of the blocks decreases with increasing deformation. Multiplication of the dislocations decreases the mean distances between dislocations, their elastic stress fields overlap, and glide is made more difficult (work hardening of crystals). To continue the slippage, the externally applied stress must be increased.

Upon further multiplication of dislocations, the internal stresses may attain values approaching the theoretical strength. In this case, fracture of the crystal takes place through the nucleation and propagation of microscopic cracks. Destruction may also be facilitated by thermal oscillations.

2.6.8 EFFECT OF DISLOCATIONS ON THE PHYSICAL PROPERTIES OF CRYSTALS.

Dislocations affect not only such mechanical properties of solids as plasticity and strength, for which the existence of dislocations is essential, but also other physical properties of crystals. For example, an increase in the number of dislocations leads to a decrease in crystal density and internal friction, a change in the optical properties, and an increase in electrical resistance. Dislocations increase the mean rate of diffusion within the crystal and accelerate aging and other processes involving diffusion. Dislocations decrease the chemical stability of the crystal; as a result, treatment of the surface with various materials (etching agents) leads to the formation of visible etch pits at the sites of the emergence of dislocations at the surface. This forms the basis for detecting dislocations in opaque materials by the selective etching method.

BIBLIOGRAPHY

[1] Rayleigh, *Proc. Roy. Soc. A* 86, , (2)07 (1912).

[2] R. Schneider *et al.*: *Introduction to Molecular Dynamics, Lect. Notes Phys* **739**, 3-40 (2008)

[3] D.K. Roy *Quantum Mechanical Tunneling And Its Applications* (World Scientific, Philadelphia PA, 1986)

[4] R.P. Feynman and A.R. Hibbs, *Quantum Mechanics and Path Integrals* (McGrow-Hill, New York, 1965)

[5] D. Frenkel and B. Smith, *Understanding Molecular Simulation. From Algorithms to Applications* 2nd ed. (Academic Press, San Diego, 2002).

[6] P. Hohenberg and W. Kohn, *Phys Rev* **136**, B864 (1964).

[7] M.S. Daw and M.I. Baskes, *Phys. Rev. Lett* **50**, 1285 (1983).

[8] M.S. Daw and M.I. Baskes, *Phys. Rev. B* **29**, 6443 (1984).

[9] M.S. Daw, *Phys. Rev. B* **39**, 7441 (1989).

[10] S.M. Foiles, M.I. Baskes, and M.S. Daw, *Phys. Rev. B* **33**, 7983 (1986).

[11] E. Clementi and C. Rosetti, *At. Data Nucl. Data Tables* **14**, 177 (1974).

[12] A.D. MacLean and R.S. MacLean, *At. Data Nucl. Data Tables* **26**, 197 (1981).

[13] J.H. Rose, J.R. Smith, F. Guinea, and J. Ferrante, *Phys. Rev. B* **29**, 2963 (1985).

CHAPTER 3

PHOTON ASISTED TUNNELING

3.1 INTRODUCTION

The probability of quantum tunneling through a one-dimensional static potential barrier is described by the theory of Wentzel, Kramers, and Brillouin (WKB) [1] if the barrier is not very transparent. For a three-dimensional static barrier the semi-classical approach $\psi \sim \exp[iS(\vec{r})/\hbar]$ for the wave function is appropriate, where $S(\vec{r})$ is the classical action. The main contribution to the tunneling probability comes from the extreme path linking two classically allowed regions. The path can be parametrized as a classical trajectory in imaginary time $\vec{r}(i\tau)$. See, for example, Ref. [2–4]. The trajectory is a solution of Newton's equation in complex time. The wave function is well defined at each point of the trajectory.

For a nonstationary barrier one can also apply the method of classical trajectory in complex time [5–9]. But in contrast to the static case, this trajectory solely connects an initial and a terminal physical points at the certain moment of time and does not track the whole under-barrier path as in the static case. One can say that the trajectory provides a semiclassical "bypass" of the complicated underbarrier dynamics through the plane of complex time [10–12]. This is the main difference in properties of trajectories for static and nonstationary barriers.

It follows that the underbarrier dynamics is governed by analytical properties of the nonstationary potential in the complex time plane. For example, a monochromatic ac field goes over into a large hyperbolic cosine [7–9] or a Lorentz shaped pulse is also amplified due to the pole structure in the plane of complex time [10–12].

The most delicate point of this theoretical construction is that the semiclassical approach for a wave function $\psi \sim \exp[iS(x,t)/\hbar]$, where $S(x,t)$ is an action for the nonstationary classic problem, is valid not at all times. Fast unavoidable processes break the semiclassical approach for short periods of time [10–14]. Since an exact analytical solution is absent it is not completely clear how those processes may influence the semiclassical "bypass".

This problem becomes extremely important when we deal with Euclidean resonance (an easy penetration through a classical nonstationary barrier due to an underbarrier interference [11, 12]). This process allows a description in terms of classical trajectories. The phenomenon of Euclidean resonance is surprising and counterintuitive since a particle emits quanta and tunnels with lower energy where, according to WKB, the barrier is less transparent. In this situation an evidence of applicability of the method of classical trajectories to nonstationary barriers would be valuable.

The goal of this study is to show by numerical calculations the validity of semiclassical methods for description of tunneling through a nonstationary potential barrier. The words "semiclassical methods" mean a possibility to approach a wave function through the classical action $\psi \sim \exp[iS(x,t)/\hbar]$ excepting some short time intervals of a fast dynamics. In addition, this means a possibility to connect certain physical points by a classical trajectory which goes apart of the complicated dynamical regions providing a "bypass" of them through the plane of complex time.

First, we consider photon-assisted tunneling which is a known phenomenon when an amplitude of the external nonstationary field is small and perturbation theory works. When the amplitude of the nonstationary field is not small the process becomes essentially multiquantum. The tunneling particle absorbs many quanta of the nonstationary field and exits from under the barrier with a higher energy. In this case perturbation theory is not applicable and one should use semiclassical methods, in particular, trajectories in complex time. It is shown that the main dynamical properties of photon-assisted tunneling are governed by analytical properties of classical trajectory in the plane of complex time.

Direct numerical solutions of the Schrödinger equation are obtained and compared with trajectory results. We check the threshold dynamics which follows from the main analytical properties of trajectories. A new branch of the wave function is only created when a position of a singularity of the external Lorentz shaped field in the plane of complex time is below compared to a singularity of the trajectory. The trajectory singularity relates to analytical properties of a solution of Newton's equation without an external nonstationary field [7–9]. We compared the numerically computed amplitude of the output wave with the semiclassical one as a function of an amplitude of the nonstationary perturbation. All the numerical results are consistent with those based on the trajectory method.

In further stage, we performed some preliminary numerical calculations of Euclidean resonance that corresponds to the opposite sign of the nonstationary perturbation. Euclidean resonance requires a more rigorous semiclassical condition compared to photon-assisted tunneling. This is due to that a new time interval Δt appears in the problem. This interval is not sufficiently long as can be seen in Sec. 3.9B. We shown that in our situation the proper semiclassical parameter, instead of being large, is of the order of unity. This parameter can be large enough for more thick potential barriers. At present, this is outside of possibilities of the numerical scheme used. So numerical studies of Euclidean resonance need further efforts.

Remarkable achievements in investigation of tunneling, including nonstationary barriers, are presented in Refs. [15–23].

3.2 FORMULATION OF THE PROBLEM

We consider tunneling through the one-dimensional nonstationary barrier

$$V(x,t) = V - \mathcal{E}_0|x| - \hbar\sqrt{2/m}\sqrt{V - E(t)}\,\delta(x), \tag{3.1}$$

shown in Fig. 3.1. The function $E(t)$ varies slowly compared to the time scale $\hbar/V$. For this reason, $E(t)$ can be treated as a discrete energy level in the δ-well and plays a role of a nonstationary drive. We suppose the function $E(t)$ to be even and $E(t) < V$. When t is pure imaginary the energy $E(t)$ is real.

In references [10–12] the δ-function was static but the outside potential was dynamical. In the present study the situation is opposite. The outside static potential enables to apply the reflectionless algorithm in the numerical calculations [24].

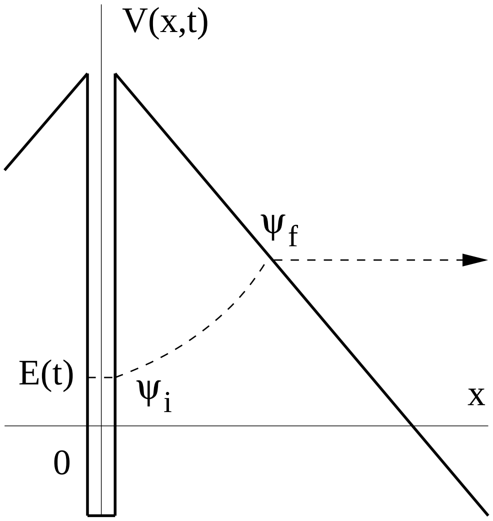

Figure 3.1: The potential energy. $E(t)$ is a position of the discrete energy level in the δ-well. The x axis is intersected at the point $V/\mathcal{E}_0$. Tunneling, assisted by quanta absorption, occurs from the initial state ψ_i in the δ-well to the final state ψ_f localized outside the barrier.

3.3 THE SEMICLASSICAL SOLUTION

Below we measure the spatial coordinate in units of $V/\mathcal{E}_0$ and time in units of $\sqrt{2mV}/\mathcal{E}_0$. In these units Schrödinger's equation reads

$$\frac{i}{B}\frac{\partial\psi}{\partial t} = -\frac{1}{B^2}\frac{\partial^2\psi}{\partial x^2} + (1-x)\psi. \tag{3.2}$$

The δ-function in the potential (3.1) is accounted for by the boundary condition

$$\left.\frac{\partial\psi(x,t)}{\partial x}\right|_{x=0} = -B\sqrt{1-h(t)}\psi(0,t), \tag{3.3}$$

where we introduce the dimensionless discrete level $h(t) = E(t)/V$ in the δ-well and the large semiclassical parameter

$$B = \frac{V\sqrt{2mV}}{\hbar\mathcal{E}_0}. \tag{3.4}$$

The process is symmetric in x and we consider a positive x only. One can write the wave function in the form

$$\psi(x,t) = a(x,t)\exp\left[iS(x,t)\right], \tag{3.5}$$

where $S(x,t)$ is the classical action, measured in the units of Planck's constant $\hbar$ and satisfying the Hamilton-Jacobi equation [25]

$$\frac{1}{B}\frac{\partial S}{\partial t} + \frac{1}{B^2}\left(\frac{\partial S}{\partial x}\right)^2 + 1 - x = 0. \tag{3.6}$$

In the semiclassical limit, $1 \ll B$, the preexponential function $a(x,t)$ in Eq. (3.5) is less significant since it provides a soft x and t dependence compared to a strong dependence given by the exponent $\exp(iS)$. The semiclassical approximation of the wave function $\psi \sim \exp(iS)$ is called the exponential one. We use this approximation below.

The boundary condition for the action follows from Eq. (3.3)

$$\left.\frac{\partial S(x,t)}{\partial x}\right|_{x=0} = iB\sqrt{1-h(t)}. \tag{3.7}$$

In the static case, when $h(t) = 0$, the exponentially small tunneling probability is given by the WKB expression $w \sim \exp(-A_{WKB})$ [1] where

$$A_{WKB} = \frac{4B}{3}. \tag{3.8}$$

One can solve the equation (3.6) by the method of variation of a constant [25]

$$\frac{S(x,t)}{B} = i\int_0^x dy\sqrt{1-y-\varepsilon(x,t)} - t\varepsilon(x,t) + iA(\varepsilon), \tag{3.9}$$

where $A(\varepsilon)$ is the certain function to be determined. The condition of independence of the action on the variable constant, $\partial S/\partial\varepsilon = 0$, has the form

$$\frac{1}{2}\int_0^x \frac{dy}{\sqrt{1-y-\varepsilon(x,t)}} = \frac{\partial A(\varepsilon)}{\partial\varepsilon} + it. \tag{3.10}$$

Under this condition

$$\frac{\partial S(x,t)}{\partial x} = iB\sqrt{1-x-\varepsilon(x,t)}. \tag{3.11}$$

The boundary condition (5.1) is satisfied if $\varepsilon(0,t) = h(t)$ which determines the function $t(\varepsilon)$ since the function $h(t)$ is given. At $x = 0$ the condition (3.10) $t = i\partial A(\varepsilon)/\partial\varepsilon$ determines in a implicit form, the function $A(\varepsilon)$ since ε is a known function of t. By means of the function $\tau(\varepsilon) = -it(\varepsilon)$ the condition (3.10) reads

$$\frac{1}{2}\int_0^x \frac{dy}{\sqrt{1-y-\varepsilon}} = \tau(\varepsilon) + it. \tag{3.12}$$

In this equation one can consider τ as a variable and $\varepsilon = h(i\tau)$. It is easy to show that

$$x = (\tau + it)\left[2\sqrt{1-h(i\tau)} - \tau - it\right]. \tag{3.13}$$

Equation (3.13) determines the function $\tau(x,t)$. As follows from Eqs. (3.11) and (3.13),

$$i\frac{\partial S(x,t)}{\partial x} = B\left[\tau + it - \sqrt{1-h(i\tau)}\right]. \tag{3.14}$$

The action can be calculated from the equation

$$iS(x,t) = B\int_{-it}^{\tau} d\tau_1 \frac{\partial x}{\partial\tau_1}\left[\tau(x_1,t) + it - \sqrt{1-h(i\tau)}\right]. \tag{3.15}$$

After a short calculation we obtain

$$\begin{aligned}\frac{iS(x,t)}{B} =& \frac{2}{3}\left[\sqrt{1-h(i\tau)}-\tau-it\right]^3-\frac{2}{3}\left[1-h(i\tau)\right]^{3/2}\\ &-(\tau+it)h(i\tau)+\int_{-it}^{\tau}d\tau_1 h(i\tau_1).\end{aligned} \tag{3.16}$$

Equation (3.16) provides the semiclassical solution of the problem if we insert the function $\tau(x,t)$ from equation (3.13).

3.4 PHOTON-ASSISTED TUNNELING

We specify below a time dependence of the energy level in the δ-well (3.1), $E(t) = Vh(t)$, in the Lorentz form

$$h(t)=\frac{h}{1+\Omega^2t^2}, \tag{3.17}$$

where h and Ω are dimensionless parameters satisfying the conditions $0<h<1$ and $\Omega\sim 1$. The pulse (3.17) is soft compared to the short time scale $1/B$. The particle under the barrier absorbs quanta of the external nonstationary perturbation (3.17) and exits from under the barrier with a higher energy as shown in Fig. 3.1. This process is called photon-assisted tunneling. From Eq. (3.16) one can analyze dynamics of the wave function (3.5). At $t\to-\infty$ the barrier is static. In this case, as follows from Eq. (3.13), $1-x=(1-\tau)^2$. Eqs. (3.5) (without the preexponent) and (3.16) result in the known WKB expression

$$\psi\sim\exp\left(\frac{A_{WKB}}{2}\left[(1-x)^{3/2}-1\right]\right),\qquad t\to-\infty. \tag{3.18}$$

Eq. (3.18) relates to the branch indicated in Fig. 3.2(a) as 1.

In addition to that, as follows from Eq. (3.16), the new branch, denoted as 2 in Fig. 3.2(a), is near to be created. This means that, according to semiclassical approximation, it exists but the proper contribution to the wave function of the type (3.5) has zero coefficient $a=0$. When $h(t)$ reaches its maximum ($t=0$) the new branch touches the branch 1, as in Fig. 3.2(b), and the coefficient a becomes

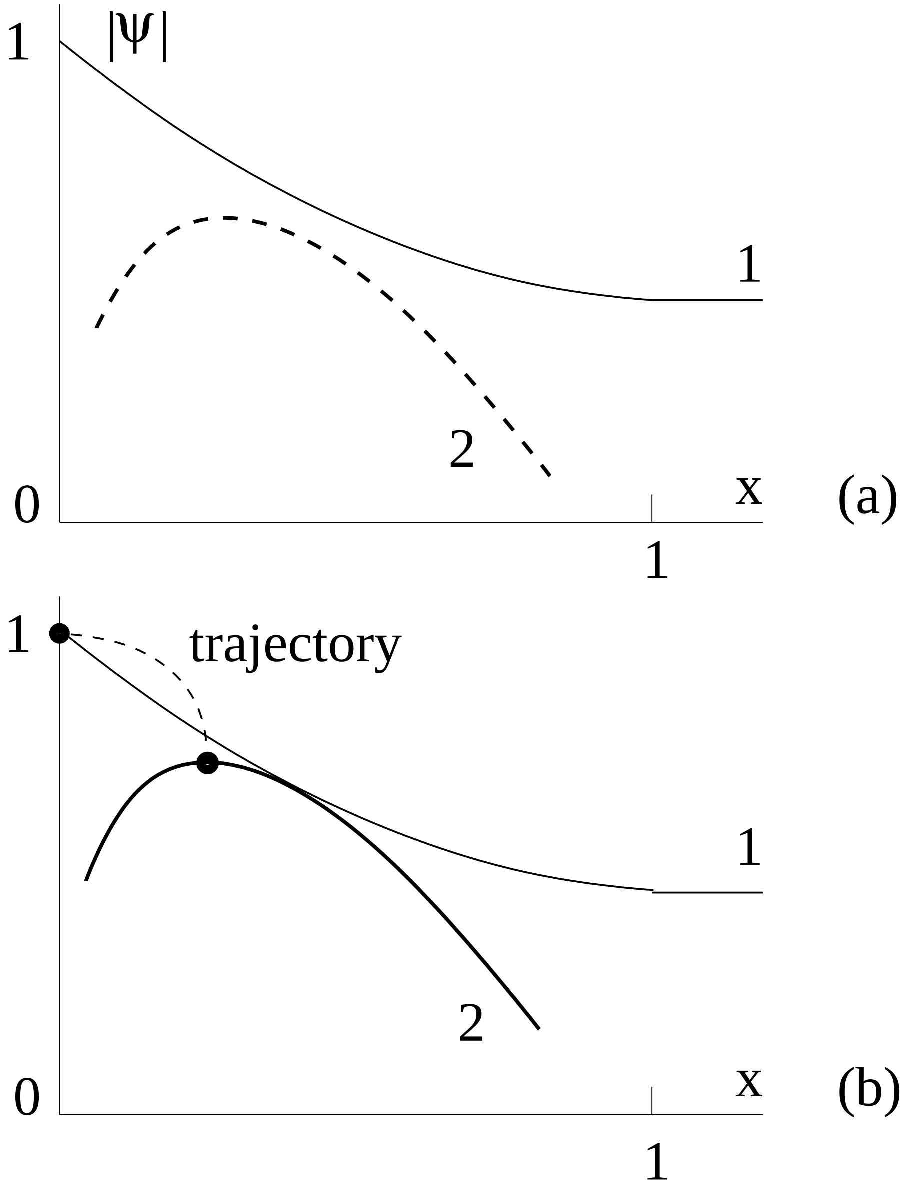

Figure 3.2: The branches of the wave function at $0 < h$ followed from the semiclassical approximation. (a) $t < 0$. The curve 1 corresponds to the conventional WKB branch at $t \to -\infty$ when the barrier is static. The new branch 2 still does not exist. (b) $t = 0$. The new branch 2 is created. The initial point (branch 1, $x = 0$) and the final one (branch 2, the top point) are connected by the classical trajectory in imaginary time (“bypass").

nonzero. This short-time process is substantially nonsemiclassical. At positive t the new branch 2 moves away from the barrier as a semiclassical wave packet.

The states before and after tunneling are denoted as ψ_i and ψ_f in Fig. 3.1. The tunneling probability can be defined as $w = |\psi_f/\psi_i|^2$ where $\psi_i = \psi(0,0)$ is associated with the branch 1 and ψ_f is an amplitude value of the branch 2 in Fig. 3.2(b). The tunneling probability, with the exponential accuracy, is given by

$$w \sim \exp\left[2iS(x_0,0)\right], \tag{3.19}$$

where x_0 relates to the maximum of the branch 2 where $\partial S(x,0)/\partial x = 0$. It follows from Eqs. (3.13) and (3.14) that $x_0 = \tau_0^2$. The parameter τ_0 satisfies the equation

$$1 - \tau_0^2 = h(i\tau_0). \tag{3.20}$$

As follows from Eqs. (3.16) and (3.19),

$$w \sim \exp\left(-A\right), \quad A = 2B\left[\tau_0 - \frac{\tau_0^3}{3} - \int_0^{\tau_0} d\tau h(i\tau)\right]. \tag{3.21}$$

Equations (3.20) and (3.21) determine the tunneling probability with the exponential accuracy if we express τ_0 from Eq. (3.20) and is inserted into Eq. (3.21).

In the static case, $h = 0$, the particle escapes from under the barrier with zero energy. Under the nonstationary conditions the energy of the outgoing particle, δE, is determined by its potential energy $(1 - x_0)V$ at the point x_0 since the kinetic energy is zero due to the condition $\partial S(x,0)/\partial x = 0$ at that point. So the energy of the outgoing particle, at the point f in Fig. 3.1, is

$$\delta E = (1 - \tau_0^2)V. \tag{3.22}$$

3.5 CLASSICAL TRAJECTORY

The tunneling probability is given, with the exponential accuracy, by Eqs. (3.20) and (3.21) which follow from the the Hamilton-Jacobi formalism. In this section we show that the same result can be obtained by a simple method of classical trajectories in imaginary time $\tau = -it$. The classical trajectory starts at the top point of the branch 2 in Fig. 3.2(b), where $\tau = 0$ and $\partial x/\partial\tau = 0$. The trajectory ends up at the certain imaginary time τ_0 where the coordinate $x(\tau_0) = 0$ belongs to the δ-well. This imaginary time τ_0 coincides with the parameter τ_0 introduced in Sec. 3.4. The trajectory is determined by Newton's equation

$$\frac{1}{2}\frac{\partial^2 x}{\partial\tau^2} = -1, \qquad \left.\frac{\partial x(\tau)}{\partial\tau}\right|_{\tau_0} = -2\sqrt{1 - h(i\tau_0)}. \tag{3.23}$$

The second equation is the boundary condition which coincides with Eq. (3.20). The solution has the form

$$x(\tau) = \tau_0^2 - \tau^2. \tag{3.24}$$

We consider the wave function not in the whole (x, t) plane but on the trajectory $\psi\,[x(\tau), i\tau]$. Then the equation holds

$$\psi\,[x(\tau_0), i\tau_0] = \exp\left(B\int_0^{\tau_0} d\tau\left[\frac{1}{4}\left(\frac{\partial x}{\partial\tau}\right)^2 + 1 - x\right]\right)\psi_f, \tag{3.25}$$

where $\psi_f = \psi\,[x(0), 0]$ and the expression in the square brackets is the Lagrangian. Since the energy $E(t) = Vh(t)$ is a slow function of t, the semiclassical relation

$$\psi\,[x(\tau_0), i\tau_0] = \exp\left[B\int_0^{\tau_0} h(i\tau)d\tau\right]\psi_i \tag{3.26}$$

is valid where $\psi_i = \psi\,[x(\tau_0), 0]$. By means of Eqs. (3.25) and (3.26) one can write the tunneling probability $w = |\psi_f/\psi_i|^2$ in the form $w \sim \exp(-A)$ where

$$A = 2B\int_0^{\tau_0} d\tau\left[\frac{1}{4}\left(\frac{\partial x}{\partial\tau}\right)^2 + 1 - x - h(i\tau)\right]. \tag{3.27}$$

In this expression the parameter τ_0 is determined by Eq. (3.20). If we insert the solution (3.24) into Eq. (3.27), we obtain the previous result (3.21). The energy of the outgoing particle is given by same expression (3.22) or, in other words, $\delta E = E(i\tau_0)$.

The trajectory in imaginary time provides a connection of the two points in Fig. 3.2(b) shown by the dashed curve. This is a "bypass" through the complex

t plane of the complicated dynamics in real time. For our Lorentz pulse (3.17), it follows from Eq. (3.20) and (3.21) that

$$\frac{A}{2B} = \tau_0 - \frac{\tau_0^3}{3} - \frac{h}{2\Omega}\ln\frac{1+\Omega\tau_0}{1-\Omega\tau_0}, \quad 1-\tau_0^2 = \frac{h}{1-\Omega^2\tau_0^2}, \tag{3.28}$$

where one should choose a lowest root for τ_0. In the static case ($h = 0$) $\tau_0 = 1$ and A has the static limit value A_{WKB} (3.8).

When h is not zero the parameter Ω, indicating the width of the nonstationary pulse (3.17), plays a crucial role in the dynamics of the system. It is easy to show in the case of a small h. When $\Omega < 1$ the parameter τ_0 hardly differs from unity, $\tau_0 = 1 - h/2(1-\Omega^2)$. Under this condition, A is close to its static limit value A_{WKB} and the energy of the outgoing particle $\delta E = hV/(1-\Omega^2)$ is small. The amplitude of the generated wave packet is close to the equilibrium value of the wave function $\exp(-A_{WKB}/2)$ at the conventional WKB exit point $x = 1$. This means that the wave packet dynamics is not very pronounced.

When $1 < \Omega$, due to the singularity of the pulse, even a small parameter h can substantially influence τ_0 which becomes to approximately equal $1/\Omega$ as follows from Eq. (3.28). As a result, one can present the action (3.28) at a small h in the form

$$A \simeq A_{WKB}\begin{cases} 1, & \Omega < 1 \\ (3\Omega^2-1)/2\Omega^3, & 1 < \Omega. \end{cases} \tag{3.29}$$

At $\Omega > 1$ the outgoing particle has the energy $\delta E = (1 - 1/\Omega^2)V$.

We see that the tunneling rate is strongly increased (a reduction of A) when Ω exceeds the threshold value $\Omega = 1$. This is a result of analytical properties of the function $h(t)$ in the complex plane which has a pole at $t = i/\Omega$. On the other hand, in the considered limit of a small h the classical trajectory has a singularity at $t = i$ which is simply a time of motion to the point $x = 0$ of singularity of the potential (3.1) [7–9]. At $\Omega < 1$ the pole of the external pulse is placed higher in the complex plane compared to the position of the trajectory singularity and the effect is weak. Under increase of Ω the two singularities merge at $\Omega = 1$ and at a larger Ω the pole of $h(t)$ is beneath of the trajectory singularity resulting in the strong effect.

One should note that the result (3.29) at $\Omega > 1$ can be obtained by an approximate method of representation of the total probability as a product of one due to quanta absorption and another due to subsequent tunneling with a higher energy. An optimization with respect to a frequency of an individual quantum and a number of those absorbed quanta is generic, to some extend, with the trajectory method. We do not repeat the calculation here but just cite Ref. [10].

3.6 NUMERICAL STUDY OF PHOTON-ASSISTED TUNNELING

In order to check the above predictions we performed the direct numerical solution of the Schrödinger equation using the finite differences scheme applied to Crank-Nicholson's method. The δ-function was modeled by a deep rectangular well of the width of a few steps $\delta x = 5 \times 10^{-4}$ in coordinate. We used different steps in time δt between 5×10^{-4} and 5×10^{-5} and different calculation precisions of 15, 30, and 100 digits. At the points $x = \pm 6$ the transparent boundary conditions were imposed [24]. In order to match this reflectionless scheme the potential was chosen at a non-zero x in the form $(1 - |x|)$ at $|x| < 6$ and -5 otherwise. According to quantum mechanical calculations, the reflection due to the change of the potential slope at $x = 6$ is small, of the order of 10^{-3} [1]. In the numerical calculations no reflection was observed. First, we calculated a wave function for a static potential ($h(t) = 0$), diagonalization of the time-independent Schrödinger equation was done using the $LAPACK$ package [26]. Fig. 3.3 shows the wave funtion obtained by the diagonalization and used as the initial condition for the time-dependent calculation.

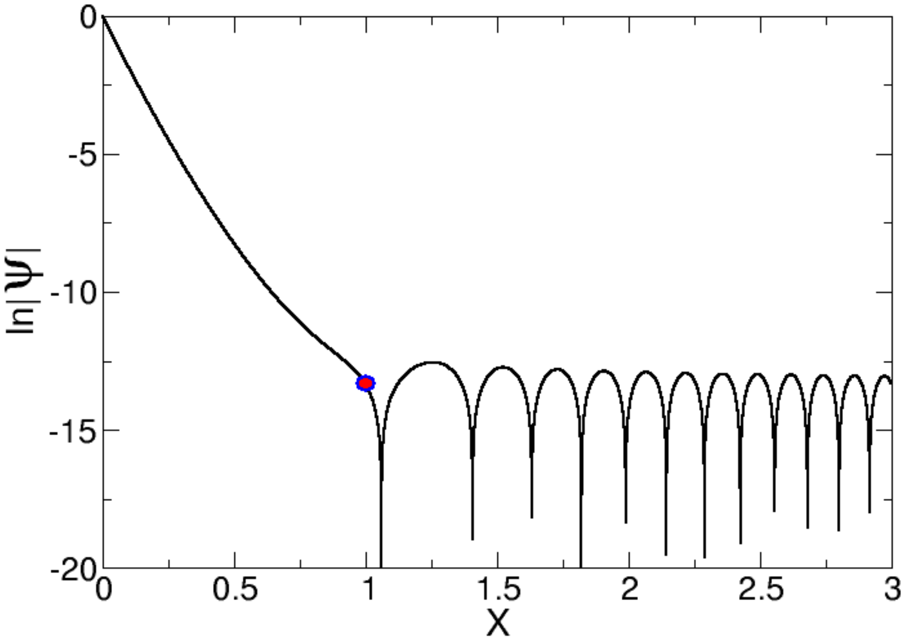

Figure 3.3: The numerically calculated initial wave function for $B = 20$. The scape point predicted by WKB theory is marked by the red dot.

After the initial wave function was calculated, we switched on the pulse (3.17) started with a large negative t, when $h(t)$ was very small, to exclude switch effects.

At sufficiently moderate $\Omega \leq 1$ no formation of an outgoing packet was observed, as demonstrated in Fig. 5.6. The increase of tunneling rate, due to a small reduction of the barrier slope, is small. This relates to the result (3.29) at $\Omega < 1$.

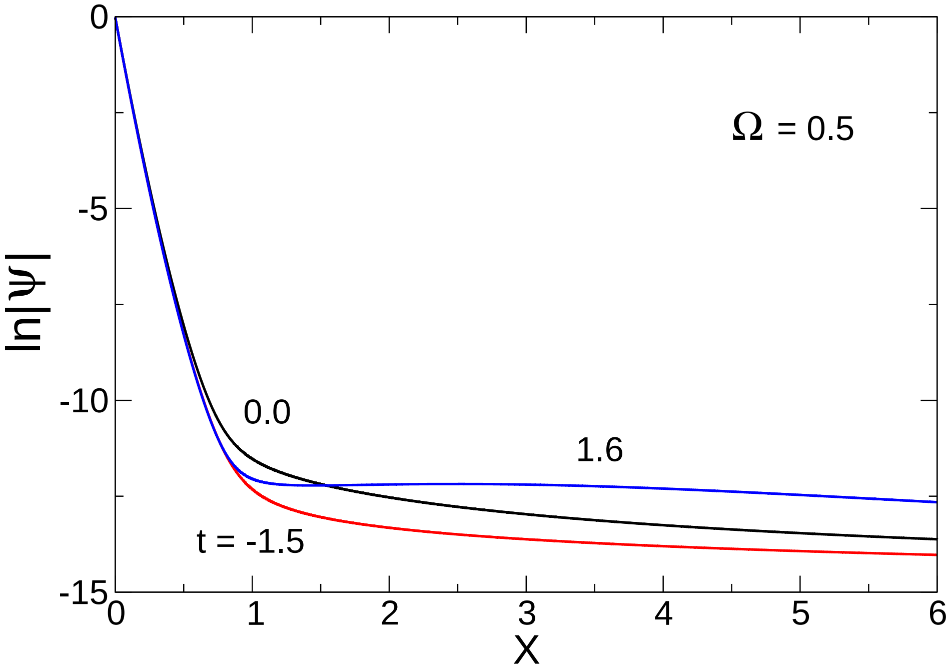

Figure 3.4: The numerically calculated dynamics of the wave function for $h = 0.1$ and $B = 20$ when Ω is less then the threshold.

At a larger $\Omega \geq 1$ (Fig. 5.7) a very pronounced wave packet is formed which propagates away from the barrier. This relates to the result (3.29) at $\Omega > 1$.

The dynamics of the packet generation in Fig. 5.7 corresponds to the theoretical scenario sketched in Fig. 3.2. At $t = 0$ the wave function hardly differs from the static one since the new branch is formed but remains hidden as in Fig. 3.2(b). At a positive t the new branch moves to the right resulting in appearance of the packet in Fig. 5.7 at $t \simeq 0.8$. At a larger t the wave packet smoothly disappears at the point $x = 6$ where the reflectionless condition is imposed [24].

Figs. 5.6 and 5.7 relate to different regimes with respect to the threshold frequency $\Omega = 1$. Actually, the threshold behavior (3.29) occurs in the limit of a small h. The value $h = 0.1$ used is small but finite and the threshold form (3.29) smears out into a narrow crossover region around $\Omega = 1$. This can be clearly seen in Fig. 5.8 where for $\Omega = 0.5$ and 0.8 the dynamics is smooth but for $\Omega = 1.5$ and 2.0

it changes qualitatively exhibiting a formation of the pronounced wave packet.

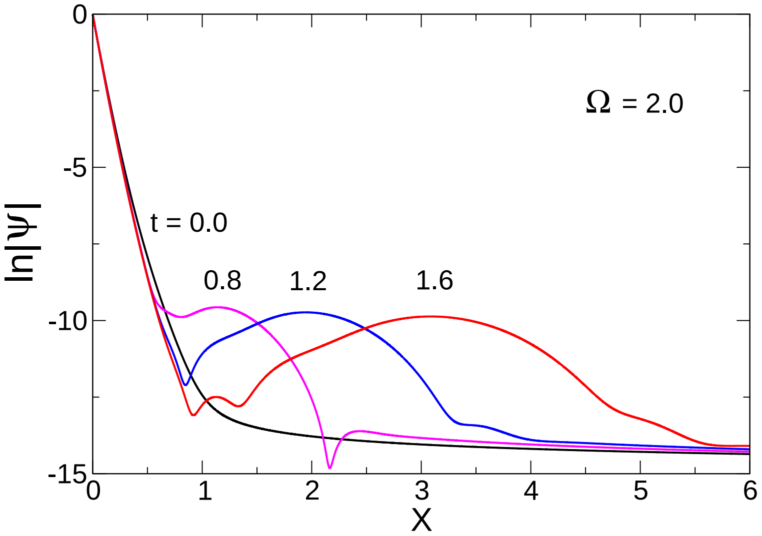

Figure 3.5: The numerically calculated dynamics of the wave function at $h = 0.1$ and $B = 20$ when Ω exceeds the threshold.

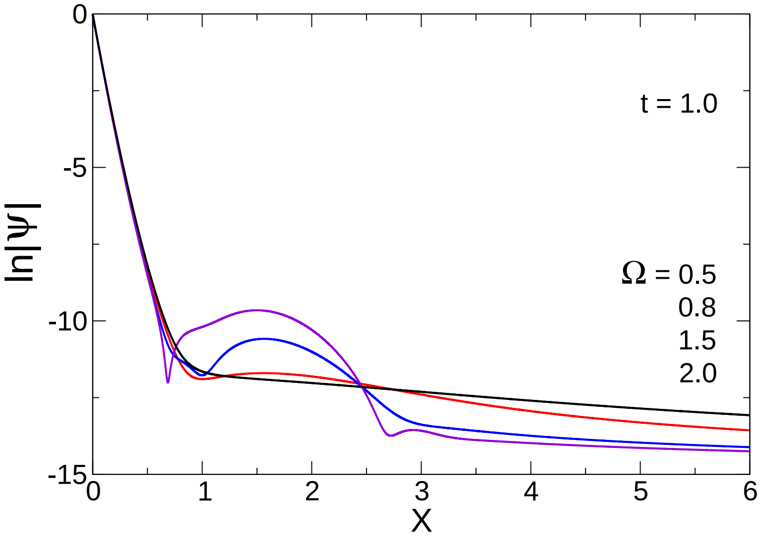

Figure 3.6: The numerically calculated wave function at $h = 0.1$ and $B = 20$. There is the crossover between the smooth behavior at Ω = 0.5 and 0.8 and the qualitatively different dynamics (wave packet formation) at Ω = 1.5 and 2.0.

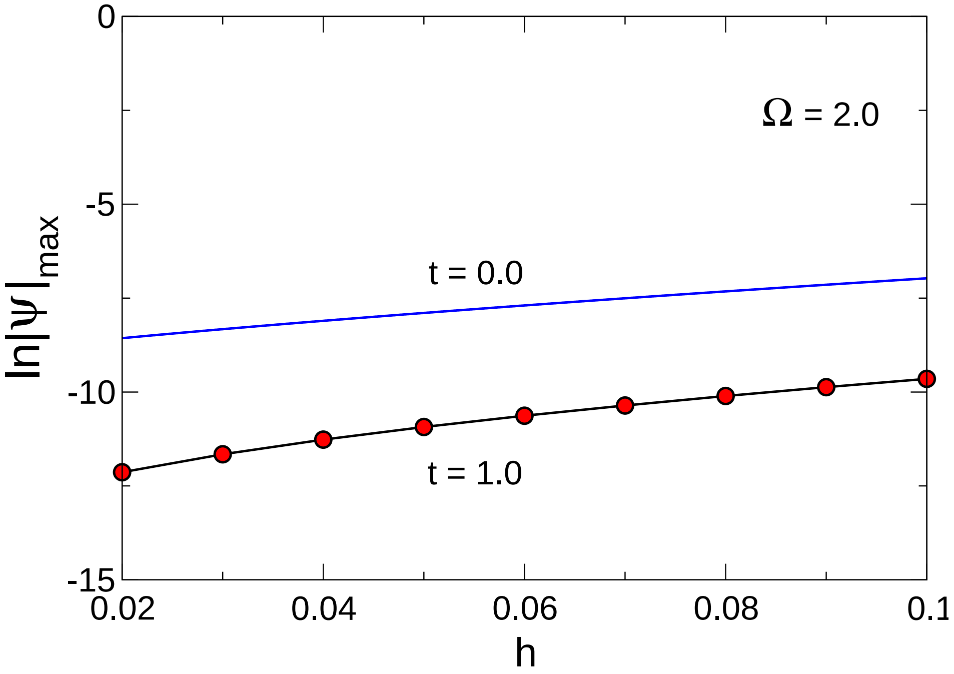

Figure 3.7: The numerically calculated dependence of the wave packet amplitude for $B = 20$ at the moment $t = 1.0$ versus h is shown by the circled curve. The theoretical dependence (without a preexponent) at $t = 0$ is drawn by the solid curve.

To demonstrate a further coincidence between the trajectory predictions and the numerical results we plot an amplitude of the wave packet versus h at $\Omega = 2.0$ in Fig. 5.9. The theoretical curve for the moment $t = 0$ follows from Eq. (3.28) where we take $|\psi|_{max} = \exp(-A/2)$. In this expression a preexponential factor is neglected. The numerical results are taken at the moment $t = 1.0$ since at $t = 0$ the branch is hidden. One can see from Fig. 5.9 that both dependences are in a reasonable agreement. The difference is due to a missing preeponential factor for the upper (theoretical) curve in Fig. 5.9. Another reason for the difference in the curves position is due to that they are taken at different moments of time. The preeponential factor for the branch 2 in Fig. 3.2b should be approximately 0.2 to get a coincidence.

One should note that when a position of the energy level varies in time just within of 2% the semiclassical approach is still valid and the dynamics is governed by the analytical properties of $h(t)$ in the complex plane of time. The presented approach should be broken at sufficiently small h which is less than 0.02.

3.7 EUCLIDEAN RESONANCE

In the previous sections we considered a positive particle energy $E(t)$ ($0 < h$) which results in a positive energy δE of the outgoing particle. In that case the energy of the state ψ_f in Fig. 3.1 is higher than one of the state ψ_i. This corresponds to photon-assisted tunneling.

When $E(t)$ is negative ($h < 0$) the exit energy δE can be negative when the energy of ψ_f is lower than one of ψ_i. In this situation a phenomenon of Euclidean resonance can occur when quanta emissions strongly interfere with tunneling [11, 12]. At a negative h the formalism, developed in Secs. 3.3 and 3.5, remains valid if to formally change the sign of h. Analogously to Fig. 3.2, one can follow branch dynamics also at a negative h on the basis of Eqs. (3.13) and (3.16).

1. At $t \to -\infty$ the situation is static and close to WKB.

2. $t < -\Delta t$. Under increase of time the WKB-branch 1-1 deforms as shown in Fig. 3.8. In addition to that, the new branch 2-2, indicated in Fig. 3.8 and which still does not exist, has a tendency to appear. The parameter $\Delta t \sim 1$ can be evaluated from Eqs. (3.13) and (3.16).

3. $t = -\Delta t$. The curve 2-2 touches the branch 1-1 and formation of the new branch 2-2 occurs within the short nonsemiclassical time $1/B \ll 1$. Since the interval $\Delta t \sim 1$ is of a semiclassical order of magnitude the fast nonsemiclassical processes, occurring within the time scale $1/B \ll 1$, have sufficient time to form the branch 2-2 in Fig. 3.9.

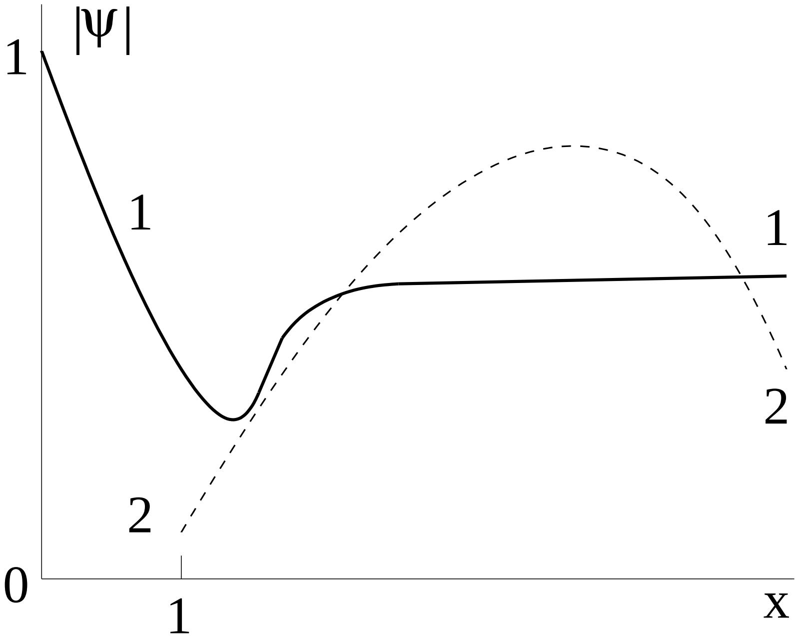

Figure 3.8: The branches of the wave function at $h < 0$ and the moment $t < -\Delta t$ followed from the semiclassical approximation. The initial branch 1-1 is deformed compared to WKB state. The new branch 2-2 almost touches the branch 1-1 having a tendency to appear.

4. $-\Delta t < t < \Delta t$. The reconnected branches are shown in Fig. 3.9 at $t = 0$. Forms of them can be calculated by means of Eqs. (3.13) and (3.16) where one should substitute the function (3.17) with a negative h. There is a cubic algebraic equation for τ^2. One solution is real related to the branch 1-2 in Fig. 3.9. Two other complex conjugated solutions result in one branch of $|\psi|$. This is the branch 2-1 in Fig. 3.9. It is remarkable that during this finite interval of time the branch 1-2 starts at the potential well, $x = 0$, and continues up to the point of maximum with no violation of semiclassical conditions. The maximum of the branch 1-2 in Fig. 3.9 determines the tunneling probability given by Eqs. (3.20) and (3.21) which can also be calculated by a classical trajectory as in Sec. 3.5. This trajectory is denoted in Fig. 3.9 by the dashed curve.

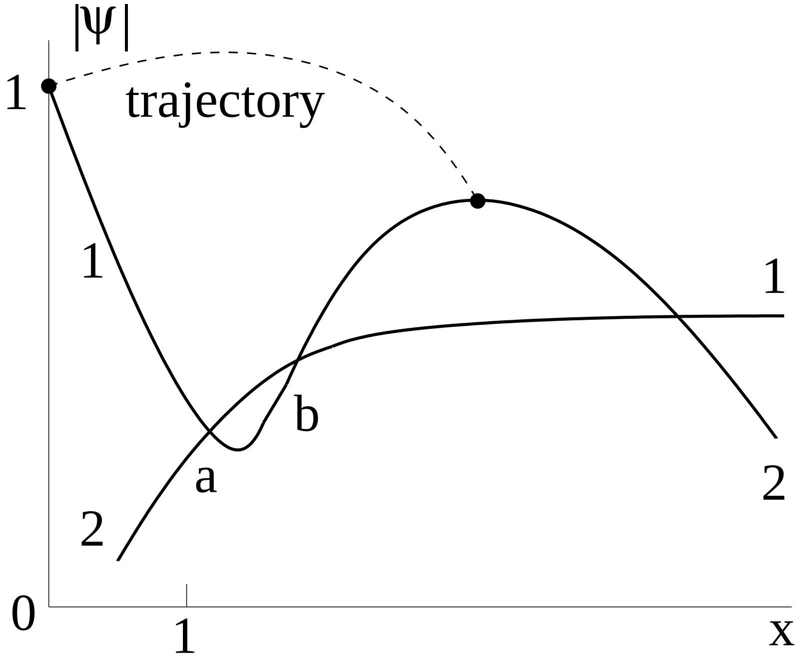

Figure 3.9: The branches of the wave function at $h < 0$ and the moment $t = 0$ followed from the semiclassical approximation. The branches are already reconnected compared to Fig. 3.8. The classical trajectory in imaginary time (the dashed curve) connects the point at the potential well, $x = 0$, and the top point.

5. $t = \Delta t$. The branches initially touch each other at some point and then they are detached during the short nonsemiclassical time $1/B \ll 1$.

6. $\Delta t < t$. The new generated branch 2-2 (similar to one in Fig. 3.8) is now physical and propagates to the right as a wave packet.

The formalism of classical trajectories in imaginary time, developed in Sec. 3.5, results at $h < 0$ in the tunneling probability

$$w \sim \exp(-A), \quad A = A_{WKB} f(\Omega, h)\,[\Omega - \Omega_R(h)]\,, \tag{3.30}$$

where the function $f(\Omega, h)$ is, generally, of the order of unity. At the resonance frequency $\Omega_R(h)$ the action formally equals zero. This phenomenon is called Euclidean resonance [11, 12]. The approximation used allows to approach the resonance frequency keeping the condition of small $\exp(-A)$. Otherwise one has to use a multi-instanton formalism.

It is instructive to consider small $|h| \ll 1$ when one can easily obtain exact analytical formulas. We omit details since analogous calculations are demonstrated in Refs. [11, 12]. In this case A has the form

$$A = A_{WKB} \frac{\sqrt{3}(1+\Omega\sqrt{3})}{2\Omega^3} \left[\Omega - \Omega_R(h)\right], \tag{3.31}$$

with the resonance frequency

$$\Omega_R(h) \simeq \frac{1}{\sqrt{3}} \left(1 - \frac{|h|}{4}\right). \tag{3.32}$$

The energy of the outgoing particle (3.22) is

$$\delta E = \frac{\Omega^2 - 1}{\Omega^2} V. \tag{3.33}$$

The equations (3.31)-(3.33) are applicable for frequencies $\Omega_R < \Omega$. There is also an upper restriction for Ω. It should not exceed the semiclassical limit which, in the dimensionless units, is of the order of the large parameter A_{WKB}. In the physical units, this condition reads $\hbar\Omega \ll V$.

3.8 NUMERICAL STUDY OF EUCLIDEAN RESONANCE

For the case of a negative h the same numerical scheme is used described in Sec. 3.6. We take the value $h = -0.28$. As follows from Eqs. (3.13) and (3.16), the resonance frequency in Eq. (3.30) is $\Omega_R(-0.28) \simeq 0.443$. For calculations the parameter $\Omega = 0.5$ is taken. So we are a little away of the resonance. In other words, the maximum of the branch 1-2 in Fig. 3.9 does not reach a value of the order of $|\psi(0,0)|$. By means of Eqs. (3.13) and (3.16) one can evaluate the important time interval discussed in Sec. 3.7 as $\Delta t \simeq 0.22$.

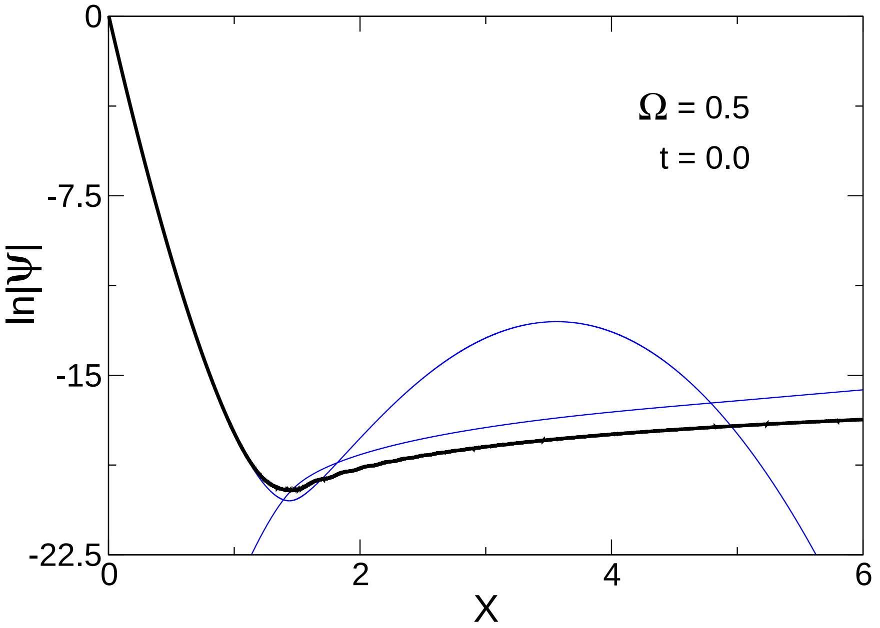

Figure 3.10: The case of $B = 20$, $h = -0.28$, and $\Omega = 0.5$ for the moment $t = 0$. The thick curve shows the numerical result. The thin curves are analogous to ones in Fig. 3.9 and are calculated from the semiclassical formalism of Sec. 3.3 (without a preexponent).

The result of numerical calculations is shown in Fig. 3.10 by the thick curve that corresponds to the moment $t = 0$. In the same figure the two branches, 1-2 and 2-1, of Fig. 3.9 are drawn as thin curves. Those branches are calculated on the basis of Eqs. (3.13) and (3.16) which account for only the classical action in Eq. (3.5) without the preexponent $a(x, t)$.

These numerical results are discussed in Sec. 3.9 B.

3.9 DISCUSSIONS

3.9.1 PHOTON-ASSISTED TUNNELING

As one can see in Sec. 3.6, for photon-assisted tunneling ($0 < h$) the predictions made on the basis of the semiclassical theory are well confirmed by the numerical calculations. Namely, it is confirmed that a classical trajectory in complex time, defined by Newton's equation, plays a crucial role in the underbarrier dynamics. Without a nonstationary drive such a trajectory has a singularity in the complex time plane which is determined by a form of the static potential barrier and a particle energy [7–9]. On the other hand, an external pulse of the Lorentz form in time has a pole at the certain complex time. When this pole is lower in the complex plane than the trajectory singularity the pronounced outgoing wave packet is formed.

Under the action of a smooth external drive the underbarrier dynamics is semiclassical (smooth) not at all times. At the certain moment there is a fast process of formation of a new branch of the wave function. The classical trajectory in complex time provides a "bypass" of that complicated dynamics since along the complex trajectory the semiclassical approach is never violated.

One has to note that the semiclassical method, including classical trajectories, relates to a substantially multiquantum processes assisting tunneling when a nonstationary perturbation is not very small [10–12].

3.9.2 EUCLIDEAN RESONANCE

For photon-assisted tunneling ($0 < h$) the new branch 2 in Fig. 3.2 is generated at the position of the main branch 1. Therefore, during this process only a local in space redistribution of density occurs. In contrast to that, for Euclidean resonance ($h < 0$) the density redistribution should occur through a finite space interval. This is clear from Fig. 3.9 where the maximum of the branch 1-2 is well apart of the region close to $x = 0$ from where the probability should come out.

The completely semiclassical solution, shown in Fig. 3.9, exists during the finite time $2\Delta t \sim 1$. The wave function from the region close to $x = 0$ smoothly reaches the maximum along the curve 1-2. Suppose, this does not happen. In this case the branch 1-2 in Fig. 3.9 intersects the branch 2-1, at the points a and b, and goes over into the same branch 2-1 at $x > b$. This nonsemiclassical abrupt cannot be smooth in time and is associated with an instability originated at the region $a < x < b$. This instability implies a short time (of the order of $1/B \ll 1$) nonsemiclassical perturbations for which the time interval $\Delta t \sim 1$ is very long. The instability develops until the system reaches its semiclassical branches (Fig. 3.9) which are almost static compared to the instability time $1/B$. By means of the formalism of classical trajectories one can connect the two points in Fig. 3.9 providing a “bypass” of the complicated dynamics. So in the limit of large B one has to expect, within the time interval $-\Delta t < t < \Delta t$, the solution shown in Fig. 3.9.

Let us take a look at Fig. 3.10. There is a coincidence between the numerical curve and theoretical ones. In order to get an exact coincidence one should shift the lower thin curve at the interval $2 < x < 6$ by $\ln|a|$ where $a \sim 0.4$ is the preeponential factor in Eq. (3.5). But the part of the branch 1-2 with the maximum is not generated. Why?

The answer relies in the fact that the time interval Δt of existence of semiclassical branches in Fig. 3.9, generally speaking, is of the order of unity. But for the parameters chosen $\Delta t \simeq 0.22$ is relatively short. This means that the two thin curves in Fig. 3.10 are not far from positions when they did touch each other at the moment $-\Delta t$ and when a did coincide with b. For $B = 20$ one can estimate $B\Delta t \simeq 4.4$ that is not a sufficiently large number. In other words, during the interval Δt, which is short in our case, the nonsemiclassical instability does not have time to be developed. For photon-assisted tunneling ($0 < h$) the semiclassical parameter is B. For Euclidean resonance ($h < 0$) the analogous parameter, which should be also large, is $B\Delta t$. We see that the conditions of Euclidean resonance are more rigorous.

The interval Δt does not depend on B. If to take, say, $B = 100$ (a very thick barrier) the parameter $B\Delta t \simeq 22$ is larger which is more preferable for formation of the maximum in Fig. 3.10. Values of B larger than 40 bring essential problems into the numerical calculations. Fluctuations in the wave function close to $x = 0$ should be small compared to the wave function at a large distance which is exponentially small as $\exp(-2B/3)$ or even less. Otherwise these fluctuations would transfer toward larger x and destroy a wave function at that region.

Another way to increase the parameter $B\Delta t$ is to take a larger $|h|$ in Eq. (3.5) keeping the same $B = 20$. In this case the minimum of the curve 1-2 in Figs. 3.9 and 3.10 becomes more deep. This requires a higher accuracy of calculations which is impossible for the numerical scheme used. For this reason, numerical studies of Euclidean resonance require further efforts.

3.10 CONCLUSIONS

The numerical solutions confirm the existing theoretical results that the main features of photon-assisted tunneling can be described by a classical trajectory in complex time. The probability of tunneling is governed by analytical properties of a nonstationary field and by those of a classical trajectory in the complex plane of time. This supports the general idea of applicability of trajectories to tunneling in a nonstationary case.

The results obtained open a way to apply the method of classical trajectories to more complicated problems of tunneling through nonstationary barriers, for example, to Euclidean resonance when the probability of tunneling through a classical barrier can be not exponentially small. The preliminary numerical study of Euclidean resonance is presented in the thesis. It is shown that Euclidean resonance occurs in more thick barriers compared to those allowed by the numerical scheme used.

BIBLIOGRAPHY

[1] L. D. Landau and E. M. Lifshitz, *Quantum Mechanics* (Pergamon, New York, 1977).

[2] C. G. Callan and S. Coleman, Phys. Rev. D **16**, 1762 (1977).

[3] A. Schmid, Ann. Phys. **170**, 333 (1986).

[4] U. Eckern and A. Schmid, in *Quantum Tunneling in Condensed Media*, edited by A. Leggett and Yu. Kagan (North-Holland, Amsterdam, 1992).

[5] L. V. Keldysh, Zh. Éksp. Teor. Fiz. **47**, 1945 (1964) [Sov. Phys. JETP **20**, 1307 (1965)].

[6] V. S. Popov, V. P. Kuznetsov, and A. M. Perelomov, Zh. Éksp. Teor. Fiz. **53**, 331 (1967) [Sov. Phys. JETP **26**, 222 (1968)].

[7] B. I. Ivlev and V. I. Melnikov, Phys. Rev. Lett. **55**, 1614 (1985)

[8] B. I. Ivlev and V. I. Melnikov, Zh. Éksp. Teor. Fiz. **90**, 2208 (1986) [Sov. Phys. JETP **63**, 1295 (1986)].

[9] B. I. Ivlev and V. I. Melnikov, in *Quantum Tunneling in Condensed Media*, edited by A. Leggett and Yu. Kagan (North-Holland, Amsterdam, 1992).

[10] B. I. Ivlev, Phys. Rev. A **62**, 062102 (2000).

[11] B. I. Ivlev, Phys. Rev. A **66**, 012102 (2002).

[12] B. I. Ivlev, Phys. Rev. A **70**, 032110 (2004).

[13] B. Ivlev and V. Gudkov, Phys. Rev. C **69**, 037602 (2004).

[14] B. Ivlev, G. Pepe, R. Latempa, A. Barone, F. Barkov, J. Lisenfeld, and A. Ustinov, Phys. Rev. B **72**, 094507 (2005).

[15] S. Keshavamurthy and W. H. Miller, Chem. Phys. Lett. **218**, 189 (1994).

[16] T. Martin and G. Berman, Phys. Lett. A **196**, 65 (1994).

[17] A. Defendi and M. Roncadelli, J. Phys. A **28**, L515 (1995).

[18] N. T. Maitra and E. J. Heller, Phys. Rev. Letter. **78**, 3035 (1997).

[19] J. Ankerhold and H. Grabert, Europhys. Lett. **47**, 285 (1999).

[20] G. Cuniberti, A. Fechner, M. Sassetti, and B. Kramer, Europhys. Lett. **48**, 66 (1999).

[21] M. Saltzer and J. Ankerhold, Phys. Rev. A **68**, 042108 (2003).

[22] S. Zhang and E. Pollak, Phys. Rev. Lett. **91**, 190201 (2003).

[23] L. Hartman, I. Gouchuk, and P. Hänggi, J. Chem. Phys. **113**, 11159 (2000).

[24] M. Erhardt and A. Arnold, Rev. Mat. Univ. Parma, **6/4**, 57 (2001).

[25] L. D. Landau and E. M. Lifshitz, *Mechanics* (Pergamon, New York, 1977).

[26] Anderson, E., *LAPACK User's Guide* (Society for Industrial and Applied Mathematics, 1999, Philadelphia, PA).

CHAPTER 4

SHAPE AND STRUCTURE OF DECAHEDRAL METALLIC NANOPARTICLES

4.1 INTRODUCTION: GEOMETRICAL CONSIDERATIONS

A cluster is defined as an aggregate of atoms; this can lead to clusters from 2 atoms (diatomic molecules), a lineal array of atoms, bidimensional or three-dimensional arrays. This work presents the study of clusters with pentagonal symmetry, with sizes up to thousands of atoms in arrays of spherical or concentric layers type.

Arrays of linked atoms forming three-dimensional clusters are considered here as sites in geometric positions attached by the edges in such a way that faces of diverse forms are generated (triangular, squared, rombohedral, etc.). Distance between the sites is considered as the distance to first neighbors, d_{NN}, which is normalized to one. There could be sites in the vertices, edges and faces, either in the surface or internals; also there could be different types of sites, depending on its position and the number and type of neighbors in the geometric array. There

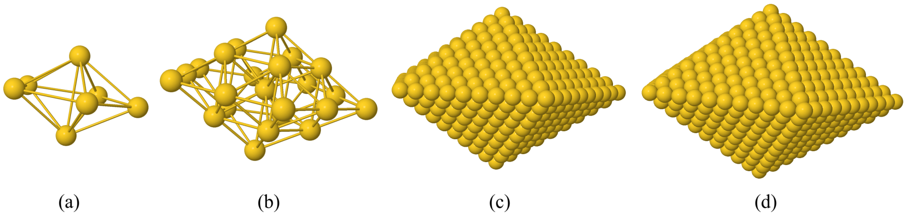

Figure 4.1: Decahedral polyhedra, a) bicapped hexahedron or decahedron of 7 atoms of order 1, without a central site; b) Decahedron of 23 atoms of order 1 with a central site; c) Decahedron of 835 sites of order 5, without a central site and d) Decahedron of 1111 atoms of order 5 with a central site.

could be also equivalent sites, which present the same geometric characteristics: to the same distance from the center of the geometric array, in the same type of site and with the same number and type of neighbors.

From the bicaped hexahedron or decahedron, Fig. 4.1a, pentagonal symmetry structures can be obtained. Among the clusters with structures of pentagonal symmetry the following structures are considered: decahedra with and without a central site, pentadecahedra, truncated decahedra (Marks decahedra), and modified and developed decahedra.

4.1.1 DECAHEDRA

Decahedra are obtained from the bicapped hexahedra and also from attaching two pentagonal based pyramids from their bases and sharing their sites (which form the equator of the cluster), yielding geometrical bodies of seven vertices (2 at poles and 5 at equator), 15 edges (all from the same length, 5 at the equator) and 10 triangular equilateral faces, 5 of them converge on each pole and by pairs they form the edges of the equator. Decahedra can be without a central site, Figs. 4.1a and 4.1c, and with a central site, Figs. 4.1b and 4.1d, without losing the decahedral form. So, decahedra have the vertices at the poles, VP, vertices at the equator, VE, at the edges over the equator, EE, edges at poles, EP, and in triangular faces T. It has to be noticed that coordination, *i. e.*, distribution to first neighbors (NN) is what makes the difference in each type of sites, although total coordination is the same for all the sites of the corresponding cluster. Table 4.1 presents the coordination of each site, for example the poles (VP) have 5 first neighbors (NN) with sites at their same shell, 1 NN towards the inner shell and 6 towards the exterior shell. The decahedron of order 1, without a central site, Fig. 4.1a, has only 7 vertices in two layers; the one from order 2, is obtained from covering the one of order one with a shell of 47 sites distributed as follows: 7 V sites of two types, 30 E sites in three layers (10 sites of one type at the equator) and 10 at triangular faces (sites T, one for each triangular face) in one single layer, for a total of 54 sites in the cluster. Decahedra of superior order are formed by coverage of this cluster of order two with successive shells of many layers each one.

The decahedron with central site of order 1, Fig. 4.1b, has 15 sites E, one per edge, of two types, 5 sites of one type at the equator, and 7 sites V, a total of 22 sites and the central one in five layers. The second order cluster results from the order one cluster covered by a shell of 82 sites distributed in 8 layers; 45 E sites in 5 layers, 30 T sites in one single layer and 7 V sites in two layers, for a total of 105 sites in the cluster, and so on for cluster of superior order.

Table 4.2 presents the geometric characteristics of decahedra with and without a central site. First column, common for all decahedra, lists the cluster order ν. This is followed by two groups of 9 columns each one, which correspond to the decahedron with and without a central site. The three first columns of each group list the number of sites on each type of site in the cluster, triangular face (T), N_T, edge (E), N_E, and vertex (V) N_V. The next column show the number of sites that form a cap of the decahedron; a cap is formed for the surface sites from the equator to the poles, which will be needed afterwards. Finally, the two last columns of each group, the number of sites in the shell, N_σ, and the total of sites in the cluster, N. Decahedra with (without) a central site, have an odd (even)

Table 4.1: Coordination or number of first neighbors (NN), of the different types of sites in the decahedron and the pentadecahedron with sites in shells in external, the same and internal shells.

	type of site						
Shell	T	EE	EP	EV	RF	VE	VP
	3	6	4	–	–	8	6
Decahedron	6	6	6	–	–	4	5
	3	0	2	–	–	0	1
	3	6	4	6	4	8	6
Pentadecahedron	6	6	6	4	4	4	5
	3	0	2	2	4	0	1

number of sites per edge.

From Table 4.2 it is observed that for both decahedron types the number of vertices per shell is 7, 2 type VP and 5 type VE. The dependence with the cluster order of N_σ and N is expressed in the following relations for the decahedra with a central site,

$$N_\sigma(\nu) = 20\nu^2 + 2, \tag{4.1}$$

$$N(\nu) = \frac{20}{3}\nu^3 + 10\nu^2 + \frac{16}{3}\nu + 1, \tag{4.2}$$

and for decahedra without a central site:

$$N_\sigma(\nu) = 20\nu^2 - 20\nu + 7, \tag{4.3}$$

$$N(\nu) = \frac{20}{3}\nu^3 + \frac{\nu}{3}. \tag{4.4}$$

4.1.2 PENTADECAHEDRA

The cap, defined below, or several caps are added to the decahedron to form the pentadecahedra, Fig. 4.2, this is, a decahedron with a wide waist or developed decahedron.

The pentadecahedra are polyhedra of 12 vertices (2 poles and 10 in vertices at the waist), 25 edges (10 from the poles to the waist, 10 at the waist and 5 of

Table 4.2: Geometric characteristics for the decahedra with and without a central site. ν is the order of the cluster, N_I with I = T, E and V, is the number of sites I. The number of sites in the cap, N_cap, the number of surface sites, N_σ, and the total number of sites in the cluster are also listed.

	with a central site						without a central site					
ν	N_T	N_E	N_V	N_cap	N_σ	N	N_T	N_E	N_V	N_cap	N_σ	N
1	0	15	7	16	22	23	0	0	7	6	7	7
2	30	45	7	51	82	105	10	30	7	31	47	54
3	100	75	7	106	182	287	60	60	7	76	127	181
4	210	105	7	181	322	609	150	90	7	141	247	428
5	360	135	7	276	502	1111	280	120	7	226	407	835
6	550	165	7	391	722	1833	450	150	7	331	607	1442
7	780	195	7	526	982	2815	660	180	7	456	847	2289
8	1050	225	7	681	1282	4097	910	210	7	601	1127	3416
9	1360	255	7	856	1622	5719	1200	240	7	766	1447	4863
10	1710	285	7	1051	2002	7721	1530	270	7	951	1807	6670

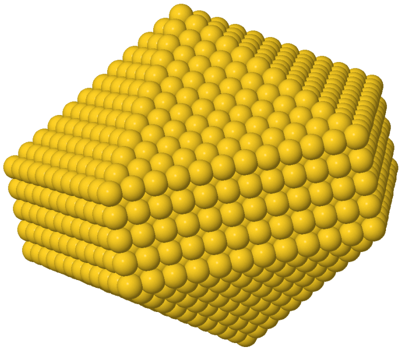

Figure 4.2: Pentadecahedron of 2766 atoms of order 65, obtained from a decahedron without a central site of order 6 with 5 caps.

other type, which join the vertices of the two pyramids, and whose length depends on the number of caps added), 10 equilateral triangular faces and 5 rectangular lateral faces (or squared, depending on the number of intermediate layers added) Fig. 4.2. The number of sites in these pentadecahedra depends on the size of the original decahedron and of how many caps are added, also, with and without central site are considered depending on the original decahedron from which they were generated. So, at the surface of the pentadecahedra there are the same type and number of sites as in the decahedra, plus the waist sites, which are divided in sites type VE, sites EE, sites at vertical edges at the width of the waist, EV and in rectangular faces, RF. Table 4.1 presents the coordination of each type of site in the pentadecahedron. Notice that, As expected; only the sites corresponding to the pentadecahedron are added and those are not of the decahedron.

For pentadecahedron order it can be used $\nu\mu$, ν for the decahedron order from which it comes and μ for the number of layers at the waist, so, regular decahedra would be pentadecahedra with μ = 1. The number of caps which are added to the decahedron referred to generate the pentadecahedron is $\mu - 1$. So, in order to have the pentadecahedron of order 65 without a central site, Fig. 4.2, that is a 2766-atom pentadecahedron one has to start with a decahedron without a central site of order 6, with 1442 atoms, and add 4 331-atom caps.

The number of sites T, EP and VP is the same as in the decahedron which originated the pentadecahedron. The number of sites EE and VE is duplicated respect the original decahedron. The number of EV and RF sites for the pentadecahedra with and without a central site is the same, and are presented in Table 4.3, which presents the geometric characteristics of the pentadecahedra with and without a central site respectively, only some of μ values are presented. There are three groups one of three columns and two of four columns respectively. In the columns of first group are listed the quantities common to the two types of pentadecahedra: cluster order ν and μ, and the number of sites EV, N_{EV}; for both polyhedra, in each following group the geometric characteristics for each

Table 4.3: Geometric characteristics for the pentadecahedra with and without a central site, obtained from the corresponding decahedron of orden ν. μ is the number of equatorial layers in the cluster. The number of EV sites, N_{EV}, RF sites, N_{RF}, of sites added, N_{ag}, surface sites, N_{σ} and of total number of sites, N, in the cluster of order $\nu\mu$ are listed. Notice that for μ = 1 values of Table 4.2 are obtained. Even when μ can have any value higher than cero, here only some values are presented.

			with a central site				without a central site			
ν	μ	N_{EV}	N_{RF}	N_{ag}	N_{σ}	N	N_{RF}	N_{ag}	N_{σ}	N
1	1	0	0	0	22	23	0	0	7	7
	2	0	0	16	32	39	0	6	12	13
2	1	0	0	0	82	105	0	0	47	54
	2	0	0	51	102	156	0	31	62	85
	3	5	15	102	122	207	10	62	77	116
3	1	0	0	0	182	287	0	0	127	181
	2	0	0	106	212	393	0	76	152	257
	3	5	25	212	242	499	20	152	177	333
4	1	0	0	0	322	609	0	0	247	428
	2	0	0	181	362	790	0	141	282	569
	4	10	70	543	442	1152	60	423	352	851
5	1	0	0	0	502	1111	0	0	407	835
	2	0	0	276	552	1387	0	226	452	1061
	3	5	45	552	602	1663	40	452	497	1287
	5	15	135	1104	702	2215	120	904	587	1739

polyhedron are presented, those of the pentadecahedron with and without a central site. A list of the number of RF sites, N_{RF}, the number of sites added, N_{ag}, of sites at the surface, $N\sigma$ and the total of sites, N, in the cluster of order $\nu\mu$. Note that for $\mu = 1$ the values from Table 4.2 are obtained.

From Table 4.3, the analytic expressions for the number of sites which are added, sites in the surface and the total of sites for pentadecahedra with central site

$$N_{\text{ag}}(\nu,\mu) = (\mu-1)(10\nu^2+5\nu+1), \tag{4.5}$$

$$N_{\sigma}(\nu,\mu) = 20\nu^2+2+10\nu(\mu-1), \tag{4.6}$$

$$N(\nu,\mu) = \frac{20}{3}\nu^3+10\nu^2+\frac{16}{3}\nu+1+N_{\text{ag}}(\nu,\mu) \tag{4.7}$$

and for pentadecahedra without central site

$$N_{\text{ag}}(\nu,\mu) = (\mu-1)(10\nu^2-5\nu+1), \tag{4.8}$$

$$N_{\sigma}(\nu,\mu) = 20\nu^2-20\nu+7+5(2\nu-1)(\mu-1), \tag{4.9}$$

$$N(\nu,\mu) = \frac{20}{3}\nu^3+\frac{\nu}{3}+N_{\text{ag}}(\nu,\mu). \tag{4.10}$$

It must be noticed that for $\mu = 2\nu+1$ ($\mu = 2\nu$) in the decahedron with (without) a central site the Ino's decahedra are obtained.

MODIFIED DECAHEDRA WITH SURFACE RECONSTRUCTION

The triangular faces in the decahedron are (111) type, as in a fcc structure the layers follow the sequence $\cdots$ABCABC$\cdots$, that is, a layer is equal to the three before one. Modification of surface reconstruction of a decahedron is obtained if for each triangular face of the decahedron a stacking fault is provocated, that is, a triangular face equal to the one before the last is added to the decahedron, following a sequence as $\cdots$ABCABA. Hereafter these polyhedra are called $mrdec$ (Montejano's reconstructed decahedron) [1]. Figure 4.3a shows the example of a decahedron with a central site of 609 sites of order 4, to which 36 sites are added

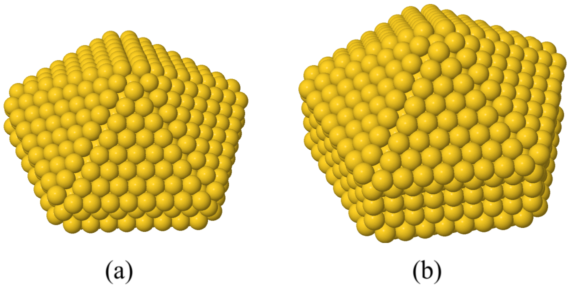

Figure 4.3: (a) Decahedron of order 4 with 609 sites and with a central site, with 360 sites aggregated for a $mrdec$ of 969 sites. (b) $mrdec$ decahedron with a central site of order 4 (609 sites), with surface reconstruction (969 sites) and three caps (181 sites each one) for a total of 1331 sites in the polyhedron, or pentadecahedron with surface reconstruction.

Table 4.4: Geometric characteristics for the $mrdec$, decahedra with and without a central site, modified with surface reconstruction. ν is the cluster order. The number of added sites, N_{ag}, of surface sites, N_σ, and of total number of sites, N, in the cluster are listed.

	with a central site			without a central site		
ν	N_{ag}	N_σ	N	N_{ag}	N_σ	N
2	100	122	205	60	77	114
3	210	242	497	150	177	331
4	360	402	969	280	317	708
5	550	602	1661	450	497	1285

per face, this is 360 sites in total, for a $mrdec$ of 969 sites. It should be noticed that it seems that a decahedron with a surface channel is obtained, although the sites which seem to form the channel are at a distance of $1.13d_{NN}$. This is why in this modification a long bond is considered and the EP sites of the interior decahedron do not form part of the surface. In fact, the surface of the resulting polyhedron is formed by the added sites and the sites VE, VP and EE of the internal decahedron, which are those which can be considered also as surface, because the remain with free bonds.

The characteristics of these polyhedra are presented in Table 4.4. ν, is the original cluster order, N_{ag} the number of sites added, N_σ, the number of sites in the surface and N the total number of sites in the cluster.

From Table 4.4, is possible to obtain the analytic expressions as a function of the order of the original cluster, for the different characteristics listed here and are presented next for the polyhedron with central site:

$$N_{ag}(\nu) = 20\nu^2 + 10\nu, \tag{4.11}$$

$$N_\sigma(\nu) = 20\nu^2 + 20\nu + 2, \tag{4.12}$$

$$N(\nu) = \frac{20}{3}\nu^3 + 30\nu^2 + \frac{46}{3}\nu + 1, \tag{4.13}$$

and without central site

$$N_{ag}(\nu) = 20\nu^2 - 10\nu, \tag{4.14}$$

$$N_\sigma(\nu) = 20\nu^2 - 3, \tag{4.15}$$

$$N(\nu) = \frac{20}{3}\nu^3 + 20\nu^2 - \frac{29}{3}\nu. \tag{4.16}$$

Alternatively it is possible to generate the pentadecahedra with surface reconstruction. For this simply add a triangular face provocating a stacking fault in the corresponding pentadecahedron, Fig. 4.3b. Table 4.2 presents the number of sites of the cap of the original decahedron, used to construct Table 4.5 for the pentadecahedra with surface reconstruction.

4.1.3 TRUNCATED DECAHEDRA (MARKS DECAHEDRA)

These result from the adequate elimination of some sites of a certain decahedron. The resulting geometry is a figure of 22 vertices (of three types), 40 edges (of 4 types, 15 from the original decahedron but shorter, and 25 which are generated by elimination of the adequate sites), 10 pentagonal faces (triangular faces from the original decahedron are converted to irregular pentagons) and 10 equilateral triangular faces (at the equator and joint by pairs) Fig. 4.4a.

Table 4.5: Geometric characteristics for the $mrdec$, decahedra with and without a central site, modified with surface reconstruction and added caps. ν is the cluster order, μ is the number of added caps in the polyhedron. Notice that for μ = 1 Table 4.4 values are obtained. Although μ can take any value higher than zero, here are only presented some values.

			with a central site				without a central site			
ν	μ	N_{EV}	N_{RF}	N_{ag}	N_σ	N	N_{RF}	N_{ag}	N_σ	N
2	1	0	0	0	122	205	0	0	77	114
	2	0	0	51	142	256	0	31	92	145
	3	5	15	102	162	307	10	62	107	176
3	1	0	0	0	242	497	0	0	177	331
	2	0	0	106	272	603	0	76	202	407
	3	5	25	212	302	709	20	152	227	483
4	1	0	0	0	402	969	0	0	317	708
	2	0	0	181	442	1150	0	141	352	849
	4	10	70	543	522	1512	60	423	422	1131
5	1	0	0	0	602	1661	0	0	497	1285
	2	0	0	276	652	1937	0	226	542	1511
	3	5	45	552	702	2213	40	452	587	1737
	5	15	135	1104	802	2765	120	904	677	2189

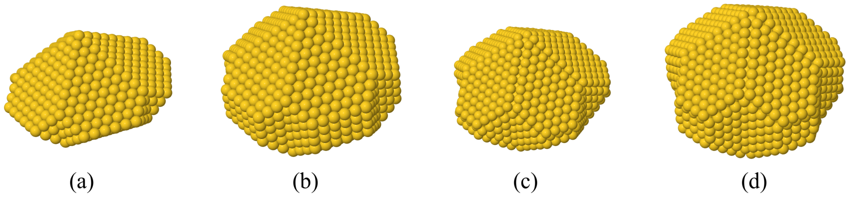
(a) (b) (c) (d)

Figure 4.4: a) Truncated decahedron without a central site of 1372 sites of order 63; b) Truncated decahedron without central site of order 63 with four caps, for a total of 2230 sites.a) Truncated decahedron with surface reconstruction. b) Truncated decahedron with surface reconstruction and with three caps.

The adequate elimination of sites is equivalent to eliminate the end sites of the edges which converge in the vertices of the equator of the corresponding decahedron. Notice that in each elimination the equatorial edges loose two sites, while the edges which converge also towards the poles only loose one, this causes that edges converging to the poles are larger than the equatorial ones, but shorter than the ones from the original decahedron.

In the first step, $n = 1$, the equator vertices from the equator of the exterior shell are eliminated, last shell, 5 sites. Second step, $n = 2$, two sites per equatorial edge are eliminated, and one of the rest of the edges, 20 sites that whit the previous stage are converted in 25. Third step, $n = 3$, the step of the edges of the last shell is repeated, 20 sites, plus two sites of each triangular face, 20 sites, besides, in one shell before the last, interior decahedron, the equator vertices are eliminated, 5 more sites in order to obtain 40 sites to be eliminated in this step, and complete a total of 70 eliminated sites in three steps. And so on, for $n < \nu$, because $N_{\mathrm{EE}} = 5(2\nu - 1)[= 5(2\nu - 2)]$ for decahedra with [without] a central site, for $\nu = n - 1$, there are only 3 [2] sites EE, see Table 4.6.

Table 4.6 lists the truncated decahedra, resulting from decahedra with and without a central site respectively. The order of the truncated decahedron consists of two numbers corresponding to the first and second column of Table 4.6, first column is the order of the decahedron generated, ν, and second column is the number of steps, n, needed to eliminate the adequate sites, or is the half of sites eliminated from each edge at the equator, $n = 1$ means that only the vertices at the equator are eliminated, first step in the elimination process. Third column lists the total number of sites eliminated from the original decahedron to obtain the truncated decahedron of order νn, $N_{(-)}$, in the fourth [eighth] the number of sites per equatorial site EE remaining in the originals (take into account that in these sites are included the two new vertices VE) per edge, for the polyhedron with a central site [without a central site] (for $n = 1$ is the number of sites in edges in the original decahedron); finally, the fifth, sixth and seventh columns [ninth, tenth

Table 4.6: Geometric characteristics for the truncated decahedra, constructed from a certain decahedra of order ν, with and without a central site. n is the half of sites eliminated from each equator edge.

order			with a central site				without a central site			
ν	n	$N_{(-)}$	N_{EE}	N_{cap}	N_σ	N	N_{EE}	N_{cap}	N_σ	N
1	1	5	1	11	17	18	–	–	–	–
2	1	5	3	46	77	100	2	26	42	49
	2	20	1	31	62	80	–	–	–	–
3	1	5	5	101	177	282	4	71	122	176
	2	25	3	86	162	262	2	56	107	156
	3	70	1	61	137	217	–	–	–	–
4	1	5	7	176	317	604	6	136	242	423
	2	25	5	161	362	584	4	121	227	403
	3	70	3	136	277	539	2	96	202	358
	4	150	1	100	240	459	–	–	–	–
5	1	5	9	271	497	1106	8	221	402	830
	2	25	7	256	482	1086	6	206	387	810
	3	70	5	231	457	1041	4	181	362	765
	4	150	3	186	422	961	2	156	327	685
	5	275	1	151	377	835	–	–	–	–
6	1	5	11	386	717	1828	10	326	602	1437
	2	25	9	371	702	1808	8	311	587	1417
	3	70	7	346	677	1763	6	286	562	1372
	4	150	5	311	642	1683	4	251	527	1292
	5	275	3	266	597	1558	2	206	482	1167
	6	435	1	211	542	1378	–	–	–	–

and eleventh] present the number of sites of the cap, N_{cap}, the number of surface sites, N_σ and the total number of sites in the resulting truncated decahedron with a central site [without a central site]. For example, the truncated decahedron without a central site of order 63, Fig. 4.4a, is generated from the decahedron with central site of order 6 (1442 sites, 10 sites per edge, 386 sites in cap, are eliminated the 5 sites VE, 4 sites EE of each one of the equatorial edges of the surface, 2 sites EP from each edge towards the poles ant the 5 VE sites from the immediate interior shell, so the truncated decahedron of order 63 has 6 sites per equatorial edge, 70 sites are eliminated and it has 1372 in total.

The number of eliminated sites, third column of Table 4.6, is the same for the two polyhedra, with and without a central site, and depends only on the number of steps n given and is obtained by

$$N_{(-)}(n) = \frac{5}{6}n(n+1)(2n+1). \tag{4.17}$$

Expressions for the number of surface sites and in total for the truncated decahedra with central site:

$$N_\sigma(\nu, n) = 20\nu^2 - 5n^2 + 2, \tag{4.18}$$

$$N(\nu, n) = \frac{20}{3}\nu^3 + 10\nu^2 + \frac{16}{3}\nu + 1 - N_{(-)}(n), \tag{4.19}$$

and for the truncated decahedra without central site

$$N_\sigma = 20\nu^2 - 20\nu - 5n^2 + 7. \tag{4.20}$$

$$N(\nu, n) = \frac{20}{3}\nu^3 + \frac{\nu}{3} - N_{(-)}(n). \tag{4.21}$$

The truncated decahedron is a polyhedron formed by 22 vertices, joint by 40 edges forming 10 pentagonal faces and 10 triangular. Vertices are of three types: VP, VE, and V'; VP (2 vertices) are the same as in the original decahedron, VE and V' (10 vertices each one) resulted by pairs from elimination of original VE and from elimination of sites from EE and EP; sites V' are found were the end of the edges converge towards the poles, this is, the edges EP join sites VP and V'.

Table 4.7: Geometric characteristics for the truncated decahedra with and without a central site. The number of surface sites for each type of site, the number of total surface sites and in the polyhedron are listed.

					with a central site					without a central site				
ν	n	N_{ET}	$N_{\mathrm{EV'}}$	N_{TF}	N_{EP}	N_{EE}	N_{PF}	$N\sigma$	N	N_{EP}	N_{EE}	N_{PF}	$N\sigma$	N
2	1	0	0	0	20	5	30	77	100	10	0	10	42	49
3	1	0	0	0	40	15	100	177	282	30	10	60	122	176
	2	20	5	0	30	5	80	162	262	20	0	40	107	156
4	1	0	0	0	60	25	210	317	604	50	20	150	242	423
	2	20	5	0	50	15	190	302	584	40	10	130	227	403
	3	40	10	10	40	5	150	277	539	30	0	90	202	358
5	1	0	0	0	80	35	360	497	1106	70	30	280	402	830
	2	20	5	0	70	25	340	482	1086	60	20	260	387	810
	3	40	10	10	60	15	300	457	1041	50	10	220	362	765
	4	60	15	30	50	5	240	422	961	40	0	160	327	685

Edges are of 4 types: the original EP edges (10 edges) and EE (5 edges), but the shorter, ET (20 edges) and EV' (5 edges) which form the triangular faces TF (10 faces) formed upon elimination of the equatorial sites, the edges EV' join the vertices V' by pairs, and the edges ET join sites VE and V'. So, any truncated decahedron will have vertex sites type VP, VE, V', edges type EP, EE, ET, EV' and faces type TF and pentagonal face PF. The number of VP sites is 2, of V' is 10 and VE is also 10. The number of remaining sites is variable and is listed in Table 4.7 for the truncated decahedra with and without central site. The number of surface sites is also listed as well as the total sites of the polyhedron. Columns 1 and 2 correspond to the order of the cluster ν and n respectively. Columns 3 to 8 [11 to 16] correspond to sites EP, N_{EP}, EE, N_{EE}, ET, N_{ET}, EV', $N_{\mathrm{EV'}}$, PF, N_{PF}, and TF, N_{TF}, respectively, and the two last columns to the surface sites, N_σ, and the total of sites N for truncated decahedra with [without] a central site.

The same method used to generate pentadecahedra, is used here. Caps can be added to the truncated decahedra in order to obtain polyhedra with 15 lateral

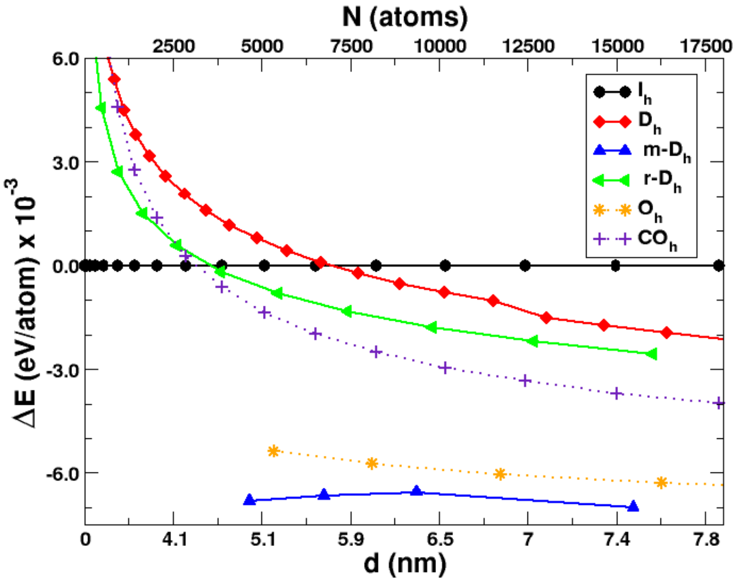

Figure 4.5: a) Energy per atom for different nanoparticles (decahedral and fcc). At this size, decahedral nanoparticles compete energetically with the fcc structures. Marks decahedra is even more stable than fcc structures.

faces, 5 rectangular and 10 trapezoidal (before triangular), Fig. 4.4b. This means that a cap is added per each layer wanted for widen the polyhedron, so the polyhedron of Fig. 4.4b has 4 equatorial layers; this means that 3 caps were added. So, in a developed truncated decahedron, there will be the same sites as in one without developing, except the TF sites, triangular face, which convert in sites TR, trapezoidal face, and the sites generated when adding the caps, sites in the rectangular faces RF and in the vertical edges, EV, joining the VE sites which are duplicated. The number of sites that will be added depends on the number of caps that the polyhedron will have, N_{cap} sites from the original truncated decahedron are added per each layer widen. It is to be noticed that in this case, the sites corresponding to EV and ET sites, will be added to the surface also.

Another modification of a truncated decahedron can be made with surface reconstruction, as explained for the decahedron, which reflects in adding N_{ag} sites to get the developed truncated decahedron, Fig. 4.4c.

Caps can be added to the developed truncated decahedra to obtain truncated decahedra with surface reconstruction and developed, Fig. 4.4d. Figure 4.5 shows point energy calculations for some of the decahedral nanoparticles previously discused, fcc structures as octahedral O_h and coboctahedral c-O_h are also included. It can be seen that in this size range, the decahedral nanoparticles energetically compete with the fcc structures, being the Marks decahedra even more stable than the O_h. The energy reference is the cohesive energy per atom for the icosahedral family.

4.2 THE DECMON-TYPE DECAHEDRAL MOTIF

In the 1960's decade, Shozo Ino was the first to report a very complete study on the structural phases for supported multiple twinned gold nanoparticles (NPs)– tetrahedra (T_h), truncated cuboctahedra (c-O_h), Mackay icosahedra (m-I_h), and regular decahedra (s-D_h) [2], by developing a theory that accounted for the specific surface, twin boundaries, elastic strain, and the adhesive energies to the substrate. This theory was the result after extensive studies of epitaxial growth of fcc metals on rocksalt faces by the same Ino [3] and Ino and Ogawa [4], where they proposed the *multiple twinned particle model with a nucleus of (001) orientation*, now known as the Ino decahedral (i-D_h) family. The Ino decahedron is a truncated decahedron with lower total surface-to-volume ratio that exposes higher energy (100) facets parallel to the 5-fold axis, and is energetically more stable than the simple (bi-pyramid) decahedra (s-D_h) but not with respect to other multi-twinned nanoparticles (MTNPs) like the m-I_h in the small and intermediate size range ($\approx$ 10 nm) [2].

This picture was prevalent for around a decade or so, and although the thermodynamic processes of shape and morphology formation for fcc particles was well understood by then by means of the Wulff construction [5], the more general problem of twinned nanoparticles was not. With the help of a modified Wulff construction for multiple-twinned particles, Marks [6] proposed a modification to the Ino decahedron which allowed for nonconvex re-entrant facets at the twin boundaries of the decahedron. This structure is now known as the Marks Decahedron (m-$\mathrm{D_h}$) and is energetically competitive with the m-$\mathrm{I_h}$ in the small size range, and even more stable than other multiple-twinned particles like the s-$\mathrm{D_h}$, the i-$\mathrm{D_h}$ and the m-$\mathrm{I_h}$ structures in the medium and large size range.

Recently, Barnard and coworkers [7] have applied nonconvex re-entrant features to the regular Mackay-Icosahedron (m-$\mathrm{I_h}$) to obtain the so called Chui-Icosahedron (c-$\mathrm{I_h}$), a modified icosahedron that, in the smallest re-entrant reconstruction, each particle contains 12 atoms less than the regular m-$\mathrm{I_h}$ family members. This type of reconstruction has been observed previously in experiments with decahedral nanoparticles by Rodríguez-López *et al.* [8], and in many reports by molecular dynamics (MD) simulations [9] (see also inside Ref. [7]).

Another related structure has been observed by Ascencio *et al.* [10] by means of high resolution transmission electron microscopy (HRTEM) characterization. They observed images with a contrast similar to the icosahedra or the truncated decahedra in gold nanoparticles samples. However, they also observed pseudo-square faces of type (100) toghether with triangular faces (111); then they proposed a new structure termed the *truncated icosahedron* (t-$\mathrm{I_h}$).

Thus, non-crystallographic atomic arrangements, like icosahedral (m-$\mathrm{I_h}$) and decahedral (s-$\mathrm{D_h}$) symmetries and some variations of them have been widely stablished, both from atomistic simulations [11] and first principles calculations [12] in the small size range (1-2 nm) or experimentally [13–15], and even other MTNPs like the bi-m-$\mathrm{I_h}$ [6, 16] had been observed; being these non-crystallographic symmetry structures lower in energy state than the fcc pristine structures, like the truncated octahedra (t-$\mathrm{O_h}$) and the cubo-octahedra (c-$\mathrm{O_h}$). A plausible explanation for this fact is that the observed MTNPs are in metastable states but with lower free energy barrier from the liquid to the m-$\mathrm{I_h}$ phase compared to the barrier from the liquid to the fcc crystalline phase [17].

In this study, we present another kind of truncation made to the regular m-I_h, that gives rise to a decahedral motif termed *decmon* (Montejano's decahedron). This decahedral structural motif presents exposed (100) and (111) facets, and depending if the truncation is performed on one side or on two oposite sides, it gives rise to the so called single truncated icosahedra (st-I_h) and double truncated icosahera (dt-I_h) families. The results presented, by means of point energy calculations for each member of these families, up to a considerable cluster size ($\approx 8nm$), are able to discern the stability and energetic competition of the single truncated icosahedra (st-I_h) with other MTNPs, such as regular decahedra (s-D_h) and icosahedra (m-I_h). Also, results are presented for structural transitions as a function of the cluster size, the identification of the surface reconstructions as a key factor in the stability of MTNPs, and the outline for the path transformation from the regular decahedra (s-D_h) to the Mackay icosahedra (m-I_h).

4.3 THE DECMON STRUCTURAL MOTIF

A classical approach to the examination of the shape and stability of nanocrystals is based on the Wulff construction [5]. The Wulff construction describes the equilibrium shape of crystals, given by the convex envelope of planes (perpendicular to the surface normals) that minimizes the total surface energy for a given enclosed volume. Equivalently, the distance of a surface plane from the center-of-mass of the crystal is proportional to the surface energy of that plane. This approach was first applied in metallic nanocrystals by Ino [2–4], that calculated the free energy of tetrahedral, truncated octahedral, icosahedral, and decahedral nanocrystals using macroscopic quantities such as cohesive, surface, twin-boundary, and elastic strain energies.

Decahedral particles have also been discussed by Marks [6], who devised a modification to the Wulff construction that allowed for re-entrant facets at the twin boundaries of the decahedron, that resulted in a polyhedron more in keeping with experimental observations. This structure has since been referred to as the *Marks decahedron* in the literature. Using this shape, Marks predicted the evolution of morphology in microcrystals, with the particle size progress from icosahedral to decahedral to truncated octahedral shapes.

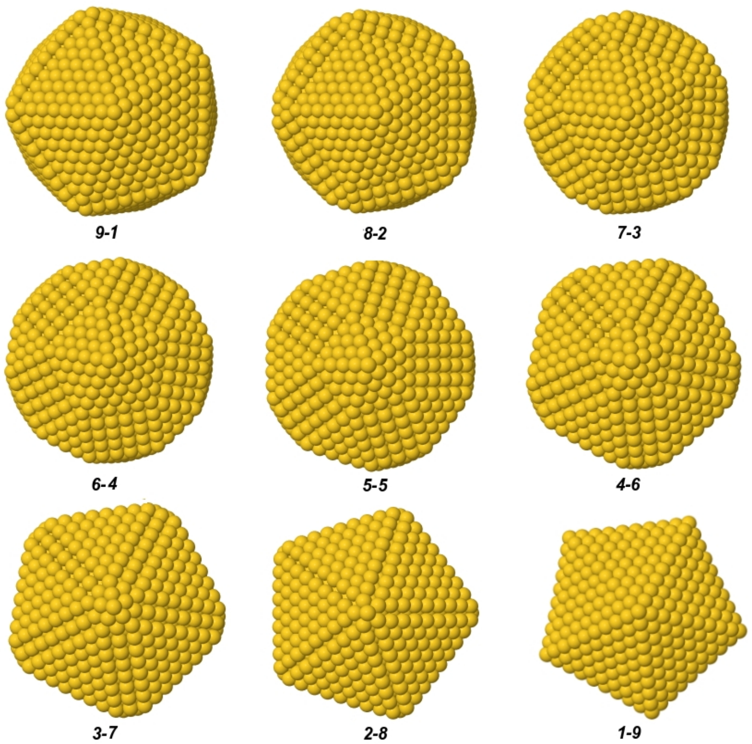

9-1 8-2 7-3

6-4 5-5 4-6

3-7 2-8 1-9

Figure 4.6: Complete sequence of truncations to the icosahedron with order ν = 10 (not shown). The single truncated icosahedra is denoted as $^{q=1}\text{st-I}_{\text{h}}{}^{\nu}$; where q is termed the order of the truncation made to the m-I_{h}, and the following relation $\nu = p + q$ holds. The decmon motif is evidenced in the halfway between the icosahedron and the decahedron structures, and observe how the surface areas with (100)-type and (111)-type atomic arrays, is changing after each truncation step, a fact that certainly influences the energetic stability of these structures through the surface energy contribution from these facets.

A more general thermodynamic theory was introduced recently by Barnard and Zapol [19], that consists in a multiscale and shape-dependent theoretical model for unsupported and pristine (untwinned) nanostructures, and then present new terms to describe planar defects and the associated edges at re-entrant angles [20]. Lately, Barnard have extended their study to a more general analytical model for the investigation of nanomaterials of arbitrary shape, and with any configuration of planar defects [21].

The approach we will follow here is based in point energy calculations by the method described above, on a wide range of particle sizes and structures.

The motif *decmon* (dm-D_h) in the truncated icosahedra comes from truncations made on the regular icosahedron, that starts drawing out the pentagonal cap to a given icosahedron of order ν, where the order ν is defined as the number of atoms in one edge, including both vertexes (see the complete sequence of truncations in Fig. 4.6; and the formal indexes definition on Fig. 4.7(a)), obtaining in this way a single truncated icosahedron (${}^{q=1}$st-$I_h{}^{\nu}$), where q is termed the order of the truncation made to the m-I_h, and the following relation $\nu = p + q$ holds. If a second truncation is made to a single truncated icosahedron, the top cap to be eliminated is different than the one discussed above; now the top cap of the ^{q}st-$I_h{}^{\nu}$ is formed by all the atoms of the decmon motif, *i.e.*, atoms in arrays (100)-type and (111)-type but is important to notice that *the number of atoms in both upper and lower caps is the same*, independently whether the cap has been truncated or not, thus the number of surface atoms in the caps remains constant.

Since the regular icosahedral models are built by shells of icosahedra (onion-like atomic growth), the central pentagonal pyramid revealed by each truncation corresponds to the succesive inner icosahedra that contains the structure. Thus, only $\nu - 1$ truncations are possible for the single truncation case in a ν-order icosahedron. Also, is worth to note from Fig. 4.6, that in this process of truncate the icosahedron, there appear facets with (100) and (111) arrays, and that the area of these facets is changing in each truncation step, which is reflected in the energetic behavior of the particle, as will be discussed later. At the very end of the truncations and after the minimization process, what is obtained is a regular decahedra (in the small size region) or a surface reconstructed decahedra (at medium and large size regions). This geometrical description is emphasized because (a) the lack or existence of a pentagonal cap (the upper part of the inner icosahedron) has relevant implications on the energy stability of the truncated icosahedra, and (b) the fact that the area of these facets is changing in each truncation step, influences the energetic behavior of the particle, as will be discussed below.

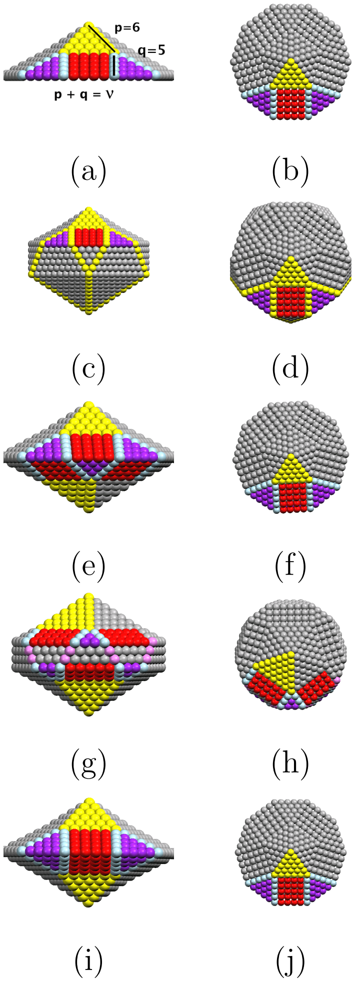

(a) (b)

(c) (d)

(e) (f)

(g) (h)

(i) (j)

Figure 4.7: The Montejano's Decahedral (*decmon*) motif is shown in (a) side and (b) top views. Indexes (p, q) –described in the text– are shown for this model. This atop decahedral motif is shared by some decahedrons, although structurally different among them, *i.e.,* by the single (st-$\mathrm{I_h}$) and double (dt-$\mathrm{I_h}$) truncated icosahedra (Schoenflies symbol C_{5v}), as well as the decmon subfamily (dm-$\mathrm{D_h}$). A comparison of representative members of the Montejano's decahedra family is shown for ^{5}st-$\mathrm{I_h}^{11}$ (c-d), the ^{5}dt-$\mathrm{I_h}^{11}$ (e-f) and ^{3}dt-$\mathrm{I_h}^{10}$ (g-h), and the regular dm-$\mathrm{D_h}$(i-j). Models are colored for to show structural differences among them.

In Fig. 4.7(a) we present a model that shows the main characteristics of this particular truncation. It is formed by a central pentagonal pyramid of triangular faces, where each one of these faces is connected to (100)-type array and each vertex to (111)-type array and these two arrays are joint toghether by couples. This pyramid has been termed the $decmon$ (Montejano's decahedron) motif, and it presents a decagonal base along with a pentagonal pyramid at the top, Fig. 4.7(b). The model proposed in Fig. 4.7(a) is only the top view of the particle and full particles could adopt one of the four differents shapes presented in Figs. 4.7[(c), (e), (g), and (i)]. These structures presented in Fig. 4.7 are only geometrical constructions, based in the proposed truncations. Energy stability calculations of these metastable states have been performed and are discussed in the next section.

Successive truncations can be made for obtain either the single truncated (^{q}st-$\mathrm{I_h}^{\nu}$) or the double truncated (^{q}dt-$\mathrm{I_h}^{\nu}$) icosahedron. We present single (Figs. 4.7(c)–(d)) and double (Figs. 4.7(e)–(h)) truncations made to the icosahedra of order ν = 11 and 10, respectively. All these structures form a new set of sub-families with decahedral symmetry, the so called *decmon* family. We have determined that the space group in Schoenflies notation for the proposed nanostructure corresponds to C_{5v}, which is a subgroup of the icosahedral (I_h) group. In Table 4.8 we present a list of the symmetry operations for the st-$\mathrm{I_h}$ and dt-$\mathrm{I_h}$ structures, compared with the icosahedral (I_h) and decahedral (D_{5h}) groups.

As can be seen, the groups I_h and D_{5h} have 120 and 20 symmetry operations, respectively. The C_{5v} subgroup has only 10 symmetry operations and therefore there is a significant reduction in the symmetry of the particles, but as expected, it has symmetry operations which are shared with the icosahedron and the decahedron.

A regular icosahedron of order ν is a cluster with a central site and $\nu - 1$ concentric icosahedra shells, and if observed perpendicularly to the five-fold symmetry axis, it has pentagonal pyramids at the top and the bottom; this picture is contrasting with Fig. 4.7(c) where the st-$\mathrm{I_h}$ has a decmon pyramid (similar to Figs. 4.7(a)), at the top and a pentagonal one at the bottom. Furthermore, when

Table 4.8: The space group in Schoenflies crystallographic notation for the proposed single (st-I_h) and double (dt-I_h) truncated icosahedra corresponds to C_{5v}, which is a subgroup of both the icosahedral (I_h) and the decahedral (D_{5h}) groups. The order of the I_h group is 120, for the D_{5h} group is 20, and for the subgroup C_{5v} is 10.

	Schoenflies symbol		
Symmetries	I_h	D_{5h}	C_{5v}
E	1	1	1
C_i	1		
C_s	15	6	5
C_2	15	5	
C_3	20		
C_5	24	4	4
S_5		4	
S_6	20		
S_{10}	24		

the top caps of two opposite vertexes are eliminated from an icosahedron, the double truncated icosahedron is obtained (dt-I_h), shown in Figs. 4.7(e) and 4.7(g), with a decmon pyramid at each side, rotated 36°.

As was mentioned before, there are $\nu - 1$ possible truncations for the single truncation case in a ν-order icosahedron; and the shape for any ${}^{q}\text{st-I}_h{}^{\nu}$ is a decmon pyramid by one side and a pentagonal one in the opossite vertex. Once we have exhausted all the possible truncations, there is obtained a fully single truncated icosahedron, whose atomic structure is an irregular decahedron, *i.e.,* a decahedron whose tetrahedral units correspond for the icosahedron, such as was defined by Marks [6].

With respect to the double truncations permissible in a ν-order icosahedron, there are $[\nu]/2$ for ν of order even and $[\nu - 1]/2$ for ν of order odd. The shape for any dt-I_h is formed by two opposite decmon pyramids joined by 10 trapezoidal lateral faces. The final shape for the fully ${}^{q}\text{dt-I}_h{}^{\nu}$ depends on whether the order (ν) of the icosahedron is odd [Fig. 4.7(e)] or even [Fig. 4.7(g)].

The $decmon$ type polyhedron (dm-D_h), Figs. 4.7(i)–(j), is a structure that results when reflecting the decmon pyramid with respect to the base; thus being a symmetric polyhedron with respect to the equator, constrasting with the ^{5}dt-I_h^{11} (Figs. 4.7(e) *vs.* 4.7(i)), which despite looking similar, they represent very different structural models.

4.4 RESULTS

The decmon truncation gives rise to two new sub-families with five-fold symmetry and a external decahedral motif. This truncation exposes the internal facets (100) and (111)–additional to the external (111) facets–of the regular icosahedron. Once all the possible truncations in a given icosahedron have been exhausted, in the small size region is obtained the regular decahedra, while in the medium and large size regions, the decahedra suffers a surface reconstruction that improves their stability.

Thus, the uncovering of these additional facets gives rise to phenomena such as surface reconstructions and a delicate competition in the energy contribution comming from the new facets (100) and (111) to the total surface energy, that very interestingly arise some regions in the path from the icosahedron to the decahedron (m-$I_h \rightarrow$ st-$I_h \rightarrow$ s-D_h) that becomes more stable than the icosahedra at those sizes.

This structural path from the icosahedra to the decahedra by means of this particular truncation, that gives rise to the external decahedral motif –the *decmon*– and surface reconstruction on two different structures, is the main subject in this study.

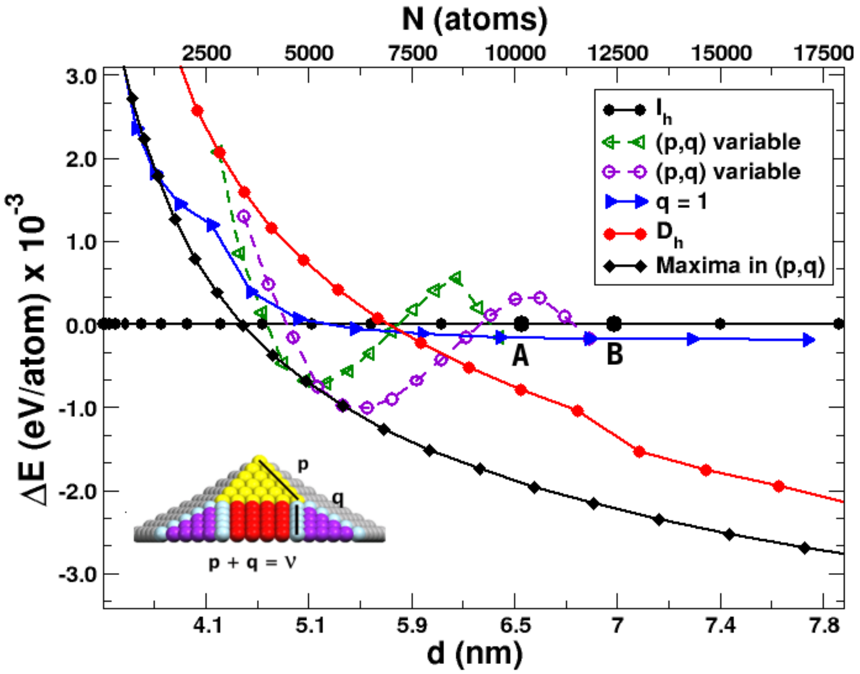

Figure 4.8: Different truncations made to the regular icosahedra are shown, plotting energy difference *vs.* mean diameter of the particle ($d \propto N^{1/3}$), where icosahedra energy is used as reference. Line in blue reflects how the first truncation (q = 1, with symbols ▶) affects the energy of the particles, being more stable to m-I$_h$ structures after a given cluster size (d = 5.3 nm). The marks A and B shown in the reference line (Δ E = 0) correspond to Mackay I$_h$ of order ν = 15 and 16, respectively. From these clusters, succesive single truncations (symbols ◁ and ○) take the structures to metastable states until a maximum in the stability (♦) is obtained. From these maxima points, a paulatine decaying is observed to the regular s-D$_h$ (◁) and to other closely related decahedral structures; *i.e.,* a partially surface reconstructed decahedron (○). These truncation paths offer evidence of a structural transformation from the m-I$_h$ to the s-D$_h$ symmetry structures.

As was mentioned from Fig. 4.6, we observe that in this process of truncate the icosahedron, appear facets with (100) and (111) arrays, and that the area of these atomic arrays is changing in each truncation step, a fact that is reflected in the energetic behavior of the particle, since both type of facets (100) and (111) contribute in a delicate balance to the total surface energy of the system. Thus, there are zones that these energy contributions improve the stability of the st-I$_h$

with respect to the icosahedron, and other zones that not, as can be observed in Fig. 4.8.

As we have discussed it, the decmon structural motif results from a particular truncation made to the regular icosahedron, being very different to that known as the Chui truncation [7]. The former truncation is a very efficient way to optimize the energy stability of metallic NPs, as can be observed in Fig. 4.8, where we have used as energy reference the cohesive energy per atom for the icosahedral family [22].

First, notice that from the (p, q) indexes that define a given st-I_h, we can keep fixed q and varying p as a function of the number of atoms (N), or viceversa. But we can also vary both (p, q) as a function of the number of atoms (N). Keeping q constant in all the size range, notice how the first truncation ($q = 1$, curve with symbols ▶) made to all the cluster sizes, begins with a high negative slope in the small size region, and after a given cluster size (around $d = 4.1$ nm), this truncation improves significantly their stability, being even more stable than the icosahedra near $d = 5.3$ nm ($N \approx 5000$ atoms). This change in the curvature is size dependent and is only observed up to the truncation $q = 3$, this is shown in Fig. 4.9 **a** . After that, succesive truncations only increase monotonically the energy stability of the ^{q}st-I_h. We have identified this abrupt change in the curvature of the nanoparticle's energy stability with a surface reconstruction in the st-I_h-particle, due to the strain release that the m-I_h structure accumulates as the size grows up. Figures 4.9 **a, b** show the surface reconstruction in an icosahedral nanopartcle.

Now, if succesive truncations are made to a given icosahedron size; lets say $\nu = 15$ (mark A in Fig. 4.8), with $N = 10\,179$ atoms, and particle diameter of $d \approx 6.6$ nm, the indexes (p, q) would be changing (keeping the relation $p + q = \nu$) and what we obtain is a transformation path from the m-I_h to the s-D_h symmetry structures (follow the symbols ◁), where each point represents the cohesive energy per atom for a different ^{q}st-I_h structure, but all of them coming from the same

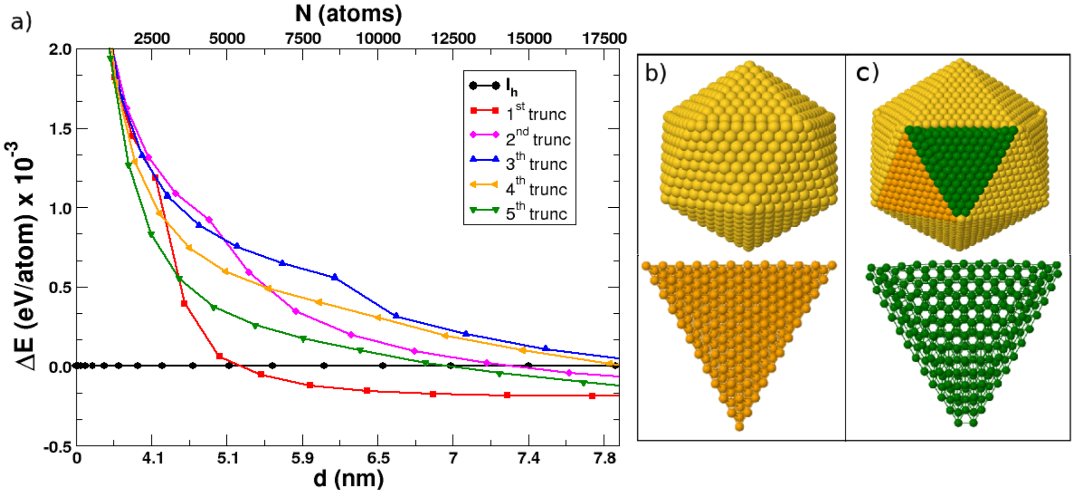

Figure 4.9: a) Energy per atom for the first five truncations made to the Icosahedron. The change in slope of the curves is related to a surface recontruccion in some of the faces of the particles. This change in slope disapear after the 3th truncation. b) and c) show an unreconstructed and a reconstructed face of the nanoparticles. The reconstructed faces have hcp packing.

m-$I_h^{\nu=15}$, as is shown in the sequence of Fig. 4.6. The first truncation slightly improves its energy (because of the energy strain release described above), the next four truncations take the particle below the icosahedral energy reference, and then the next five truncations or structures are more stable than the icosahedra around the respective ^{q}st-I_h cluster, reaching a maximum in $\nu - q = p = 5$. If the truncations are made until exhausting them, an irregular decahedron is obtained, which after relaxation turns either into the *structure with the same energy for a perfect decahedra* (shown for reference the complete s-D_h family with symbols ●), or into a *partially surface reconstructed* decahedra, evidenced by the last truncation for st-$I_h^{\nu=16}$ (follow the curve marked B with symbols ○). By partial surface reconstruction in a nanoparticle, we mean that only occurred in half surface of the decahedral particle, ending this surface with an hcp atomic packing (...ABCB) in the surface. The other half surface (originally from the m-$I_h$structure) remains with fcc atomic packing (...ABCABC). A partial surface reconstruction

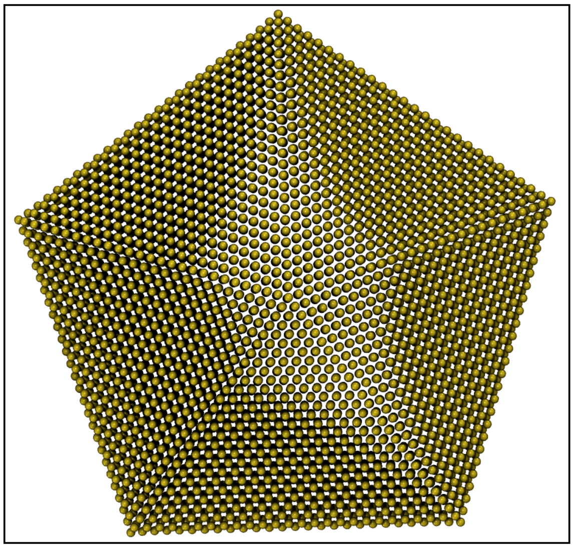

Figure 4.10: Reconstructed decahedron. Some regions of the nanoparticle changed its packing from fcc to hcp. This reconstruction improves their stability.

also appears for the regular decahedral NPs (see the curve ●) with a mean diameter particle around 7 nm, as can be infered from the change of slope for the data of energetic stability of the decahedra (s-D$_h$), and the explanation of this surface reconstruction for Au NPs is related with the release of the strain energy, accumulated by the nanocrystal growth. Figure 4.10 shows a surface reconstructed decahedral nanoparticle, it can be seen that some regions of the surface are in an hcp arrangement.

The maxima with $p = 5$, reached in these two path of truncations made from the m-I$_h$ to the s-D$_h$ structures ($\triangleleft$ for m-I$_h{}^{\nu=15}$ and $\circ$ for m-I$_h{}^{\nu=16}$), is constant over a given size range; *i.e.*, it is dependent of the cluster size. Therefore, and very interestingly, there are (size dependent) constants $p_1 < p_2 < p_3$, a fact that is related with the delicated competition between the release of the strain energy due to the appearence of (100) *vs.* (111) facets in these single truncated icosahedra.

Figure 4.11 shows how the decmon subfamilies (st-I$_h$, dt-I$_h$, and dm-D$_h$) com-

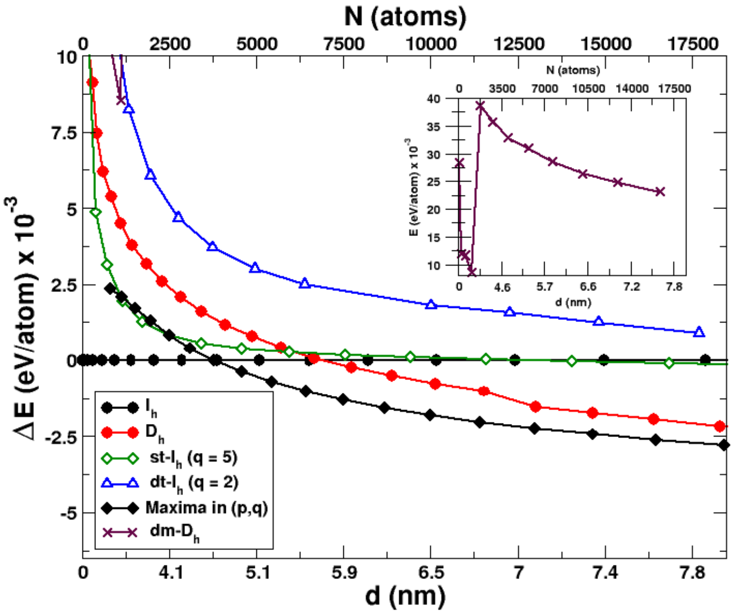

Figure 4.11: Energy competence between the different sub-families that show the decmon decahedral motif, plotting the energy difference *vs.* mean diameter of the particle ($d \propto N^{1/3}$), where icosahedra energy is used as reference. For reference also, we plot the curves for regular s-D_h (●), and the maxima obtained for the single truncations (♦). Data plotted with symbols ◇ correspond to ^{5}st-I_h and with the symbol △ is for the ^{2}dt-I_h. The *decmon* (dm-D_h) structure does not compete in energy with these ^{q}st-I_h and ^{q}dt-I_h structures, and is shown in the inset with symbol ×.

pete among them, where the cohesive energy for gold NPs is plotted as a function of the cluster size (upper *x*-axis) or as a function of the relative particle diameter (lower *x*-axis). We choose to plot representative truncations for each subfamily, *i.e.*, the 5*th* truncation for the st-I_h (◇), the 2*nd* truncation for the dt-I_h(△), the maxima for all the path truncations from the m-I_h–to the–s-D_h symmetries (♦) and in the inset, the energetically non-competitive dm-D_h structure family (×). For energy reference we plot the cohesive energy per atom for the icosahedral (m-I_h, •) as well as the regular decahedral family (s-D_h, •).

We conclude from this figure, that up to a given truncation, these single truncations made to the regular icosahedron improve its energetic stability on the resulting st-I_h, but that double truncations does not improve the energy of the NPs, as seen for the dt-I_h and dm-D_h curves. However, we can conclude that the *decmon* structural motif that results from this particular truncation made to the regular icosahedron, is an efficient way to optimize the energy stability of metallic NPs, if operated only for to obtain the single truncated icosahedra.

4.5 DISCUSSION

Figure 4.12 shows the potential energy surface for the transition from the icosahedra to the decahedra, for a wide spectrum of cluster sizes. The solid-red line is just the zero energy reference, and the main results described in Figs. 4.8 and 4.11 are evidenced in this figure, such that the surface reconstructions for the truncated icosahedra (mark II in the beggining of the truncations, and the mark IV in the exhausted truncated icosahedra, that follows the line with symbols square-blue), and the maxima for the decmon motif (solid-blue line). The data for the regular decahedra, presenting a partial surface reconstruction (mark V), correspond to both the truncated icosahedra and the regular decahedral that after relaxation, they become the same structure presenting surface reconstruction.

A more detailed discussion follows. First, notice that line with symbols bullet-red correspond to the energy of the members of the regular decahedral family; the line with symbols square-blue correspond to the exhausted truncated icosahedra. In the small size region (mark III), there is not present still the surface reconstruction in both structures, thus they are the same and the point energy calculations coincide.

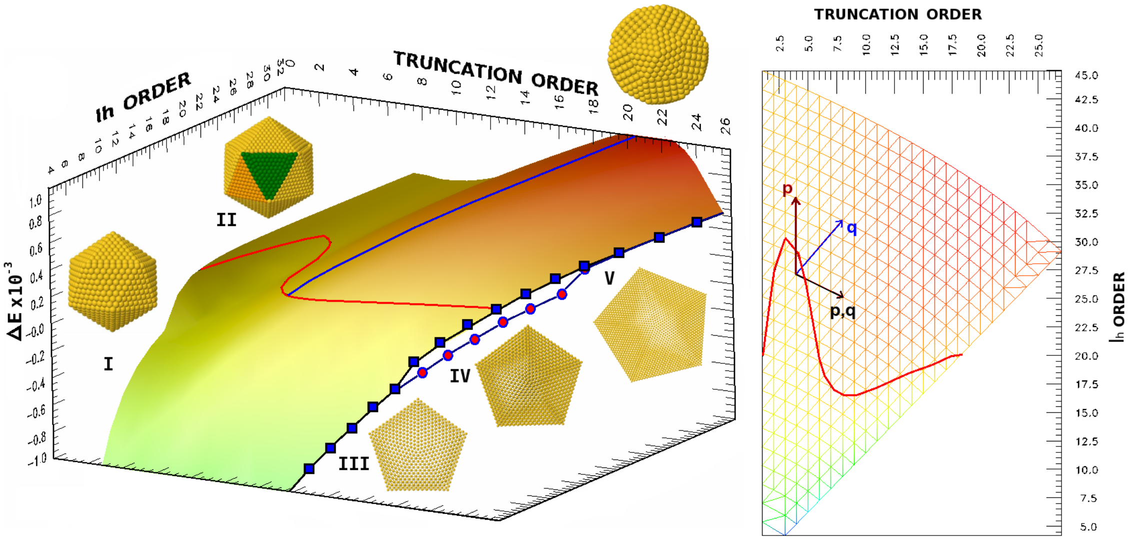

Figure 4.12: Lines with symbols red bullet correspond to the energy of the members of the regular decahedral family; and that the line with symbols with square blue correspond to the exhausted truncated icosahedra. In the small size region (marked III), both structures are the same, thus the point energy coincide. After a given cluster size, the exhausted truncated icosahedra –that at this point is an irregular decahedra, suffers a surface reconstruction that improves their energy stability (marked IV), therefore the energies of these families start to be separated. The regular decahedra suffers a surface reconstruction at a bigger size, and then the structures become to be the same again, but now the regular decahedra becomes an irregular decahedra, being the most stable, such that now both structures present a surface reconstruction (marked V).

After a given cluster size, the exhausted truncated icosahedra that at this structural point is an irregular decahedra, it experiences a partial surface reconstruction that improves their energy stability (marked IV, line square-blue), therefore the energies of these two families (the regular decahedra and the truncated icosahedra) start to be energetically separated. At bigger particle size, the regular decahedra (bullet-red line) also experiences a partial surface reconstruction, thus both irregular and regular decahedra became the same structure again, as is interpreted from the point energy calculations, but from now on this structure will present a surface reconstruction (marked V). As was mentioned above, by partial surface reconstruction we mean an hcp stacking in the surface (...ABCB), but only on one side of the decahedra–the side that is gradually discovered by the truncations.

Second, in the way of transformation from the icosahedra to the decahedra, there exists the truncated icosahedra structure (marked VI, being maxima all along the blue line). The improved energetic stability on these structures, is due to the competence of facets (100)and (111), a delicate competence that is related with the exposed areas that these facets present, thus the total surface energy of the particle has contributions from open (100) and closed (111) facets.

These results also evidence the magnitud of the energy potential barriers among different structural motifs, and address important aspects of nanoparticle growth. This path transition from the decahedral to the icosahedral symmetry in gold metallic nanoparticles, gives the possibility to study phase structural transitions in NPs, as well as to connect the results with some previous studies on the subject. Also, the surface reconstruction effects in these truncated icosahedra and decahedra, that gives stability to these multi-twinned nanoparticles, would be part of the eventual explanation of the very fundamental question of why there are observed MTNPs at really big sizes (at the micro-scale) with non-crystallographic symmetries?. Among other explanations for this fact, that some arguments can come from kinetic growth and metastable energetic transitions; certainly one that has to be considered is the surface reconstruction effect.

In conclusion, we have introduced the *decmon* decahedral motif for metallic NPs, which identifies a new family of decahedral structures. The decmon motif arises after proper truncations made on the icosahedron, it presents atomic facets (100) and (111) exposed in the surface, and whose energetic competition, at a given cluster size, make the structures very favorable from the energetic point of view. Other outlined aspects that is worth to mention are, the finding of structural transitions as a function of the cluster size, the appearing and competition of surface reconstruction with faceting, and the outlined path transformation from the m-I_h to the s-D_h symmetry structures.

BIBLIOGRAPHY

[1] Montejano-Carrizales, J. M., and Rodríguez-López, J. L., Institute of Physics University of San Luis Potosi, Internal report (2002) and personal communication.

[2] S. Ino, *J. Phys. Soc. Jpn.* **27**, 941 (1969).

[3] S. Ino, *J. Phys. Soc. Jpn.* **21**, 346 (1966). S.Ogawa, S. Ino, T. Kato, and H. Ota *J. Phys. Soc. Jpn.* **21**, 1963 (1966);

[4] S. Ino and S. Ogawa, *J. Phys. Soc. Jpn.* **22**, 1365 (1967).

[5] G. Wulff, *Z. Kristallogr.* **34**, 449 (1901).

[6] L.D. Marks, *J. Cryst. Growth* **61**, 556 (1983).

[7] A.S. Barnard, G. Opletal, I.K. Snook, and S.P. Russo, *J. Phys. Chem. C* **112**, 14852 (2008).

[8] J.L. Rodríguez-López, J.M. Montejano-Carrizales, U. Pal, J.F. Sánchez-Ramírez, H.E. Troiani, D. García, M. Miki-Yoshida, and M. José-Yacamán, *Phys. Rev. Lett.* **92**, 196102 (2004).

[9] Y.H. Chui, R.J. Rees, I.K. Snook, B. O'Malley, and S.P. Russo, *J. Chem. Phys.* **125**, 114703 (2006); Y.H. Chui, G. Grochola, I.K. Snook, and S.P. Russo, *Phys. Rev. B* **75**, 033404 (2007).

[10] J.A. Ascencio, M. Pérez, and M. José-Yacamán, *Surf. Sci.* **447**, 73 (2000).

[11] C.L. Cleveland, U. Landman, T.G. Schaaff, M.N. Shafigullin, P.W. Stephan, and R.L. Whetten, *Phys. Rev. Lett.* **79**, 1873 (1997); Structural evolution of smaller gold nanocrystals: the truncated-decahedral motif C.L. Cleveland, U. Landman, M.N. Shafigullin, P.W. Stephens, and R.L. Whetten, 1997 Structural evolution of larger gold clusters *Z. Phys. D* **40**, 503 (1997).

[12] F. Baletto, R. Ferrando, A. Fortunelli, F. Montalenti, and C. Mottet, *J. Chem. Phys.* **116**, 3856 (2002).

[13] L.D. Marks, *Rep. Prog. Phys.* **57**, 603 (1994).

[14] T.P. Martin, *Phys. Rep.* **273**, 199 (1996).

[15] K. Koga, T. Ikeshoji, and K. Sagawara, *Phys. Rev. Lett.* **92**, 115701 (2004).

[16] K. Koga, *Phys. Rev. Lett.* **96**, 115501 (2006).

[17] H.-s. Nam *et al.*, *Phys. Rev. B* **71**, 233401 (2005).

[18] An extensive and complete review on the relative stability –among other aspects– of different gold nanostructures, see the reference: A.S. Barnard, *Rep. Prog. Phys.* **73**, 086502 (2010). A. Howie and L.D. Marks, *Philos. Mag. A* **49**, 95 (1984); L.D. Marks, *Philos. Mag. A* **49**, 81 (1984); P.M. Ajayan and L.D. Marks, *Phys. Rev. Lett* **60**, 585 (1988);

[19] A.S. Barnard and P. Zapol, *J. Chem. Phys.* **121**, 4276 (2004).

[20] A.S. Barnard, *J. Phys. Chem. B* **110**, 24498 (2006).

[21] A.S. Barnard, *J. Phys. Chem. C* **112**, 1385 (2008).

[22] All the calculations were performed using the semi-empirical embedded atom method (EAM) as coded in the XMD algorithm [23], for Au element. The clusters were quenched at a rate of 5×10^{12} K/s for 35 ps.

[23] Jon Rifkin, University of Connecticut, http://www.ims.uconn.edu/centers/simul.

CHAPTER 5

MECHANICAL PROPERTIES OF DECAHEDRAL NANOPARTICLES: NANOINDENTATION

In this chapter we present a theoretical analysis of uniaxial compression to study malleability and hardening of gold nanoparticles with decahedral (D_h) shape, trying to explain some recent nanoindentation experiments in this kind of nanoparticles. It is found that an outstandingly high malleability up to 80% is present on the *Dh* metal nanoparticles, and this plastic deformation is followed by the blockage of partial dislocations by the coherent twin boundaries of the D_h nanoparticle, resulting in significant strain hardening of the nanocrystal. The dislocation blocking at twin boundaries results in a large plastic deformation with an increase in strength.

5.1 INTRODUCTION

Five-fold symmetry nanoparticles has fascinated researchers for more than half a century [19, 27]. If we assume this structure is formed by five regular tetrahedral

($\mathrm{T_h}$) fcc units, the space is not filled and a gap of 7.35° is formed (Fig. 5.1,**a**). This gap has to be closed by stressing the lattice of the $\mathrm{T_h}$ units; Fig. 5.1,**b** shows an experimental bright field (**BF**) image of a Au $\mathrm{D_h}$ nanoparticle. Recently the resulting strain distribution on a $\mathrm{D_h}$ particle has been studied by ***HRTEM*** [28]. In order to reproduce this strain distribution we have made theoretical calculations that are in agreement with the strain profile reported in Reference [28]; Fig. 5.1,**c** shows the calculated distribution of the $\varepsilon_{r\theta}$ component of the strain tensor in the middle of the particle. From this distribution, we can plot $\varepsilon_{r\theta}$ for a given radius (Fig. 5.1,**e**), and as we have mentioned, this results are in agreement with the experiment.

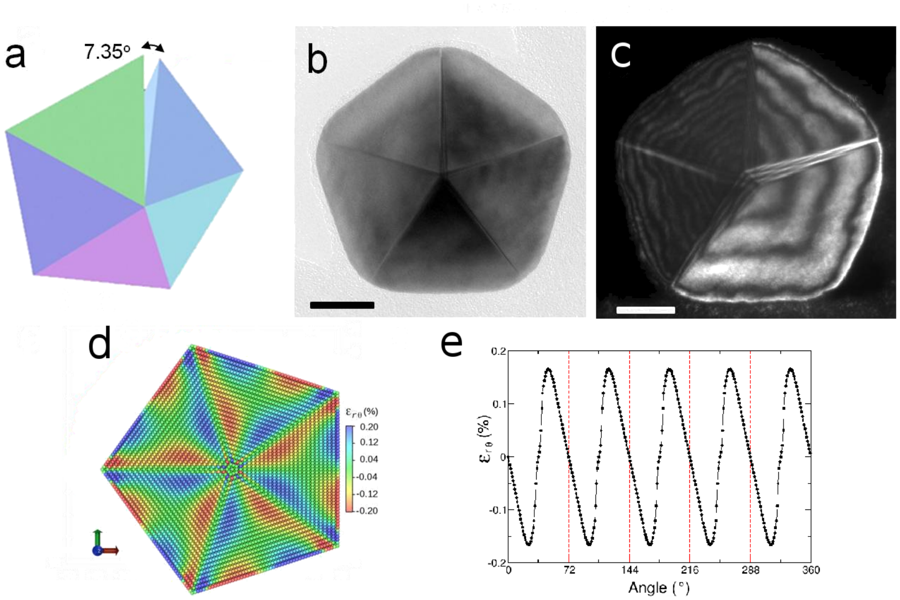

Figure 5.1: Experimental and theoretical $\mathrm{D_h}$ nanoparticles. **a**, Geometry angular deficiency in decahedral shape consisting of perfect tetrahedrons, the angle between adjacent (111) planes is 7.35° on projection of $\langle 110 \rangle$ orientation. **b**, Bright field (**BF**) image of a Au $\mathrm{D_h}$ nanoparticle. **c**, **WBDF** image of the $\mathrm{D_h}$ particle shown in **b** with bent thickness lines revealing the intrinsic strain in the structure. **d**, Calculated $\varepsilon_{r\theta}$ strain map for a gold $\mathrm{D_h}$ nanoparticle. **e**, $\varepsilon_{r\theta}$ $vs.$ θ for a given radius at the center of the particle. Scale bars in **b** and **c** are 20 nm.

Weak-beam dark field (**WBDF**) method in the **TEM** [29] can be used to study the strain field distribution on a D_h Au nanoparticle. This method allows us to follow directly the evolution of the plastic deformation. The method takes advantage of the enhancement of the contrast generated by the lattice deformation and thickness when the corresponding plane is out off the Bragg condition. **WBDF** images were taken using diffraction spots (111). Fringes which represent equal thickness contours are formed; however, the presence of strain in the structure bends the thickness fringes, as is shown in Fig. 5.1,**c**. How the existing strain in decahedral nanoparticles affects their mechanical properties is one of the objectives of this study.

The experimental studies of mechanical properties of individual nanoparticles are of great interest for the full understanding of the mechanical behavior of the matter at this size regime. The experimental challenges are enormous and no direct studies have been reported. Previous experimental work on *in-situ* measurements of mechanical properties using transmission electron microscopy has been focused on metal nanowires [1]. Zheng *et al.* have studied the plasticity in Au nanowires with a size less than 10 nm [13]. They observed that plasticity of the Au nanowires is dominated by the partial dislocations (*PDs*) emitted from the steps of the free surfaces; their results were consistent with previous theoretical calculations [14,17]. In the case of nanoparticles, the only experimental work that indirectly measures properties of individual nanoparticles is that of Sun *et al.* [18]. They used electron beam irradiation to induce mechanical stress on metal crystals inside graphitic nanocontainers. They concluded that the short-lived *PDs* nucleated by the formation of intrinsic stacking faults.

Recently, some interesting experimental results have been obtained by Prof. José-Yacaman's group (*Department of Physics and Astronomy, University of Texas at San Antonio*). They have been able to directly measure some mechanical properties of Au nanoparticles, including decahedral and icosahedral geometries. The deatails about this experiments will be discused in the next section.

5.2 EXPERIMENTAL RESULTS

Four different types of gold particles were tested: an octahedral fcc with no defects (Fig. 5.2,**A**) and three different particles containing twins: decahedral (D_h), icosahedral (I_h), and a single twinned (*Ts*) nanoparticles (Fig. 5.2,**B, C, D**, respectively).

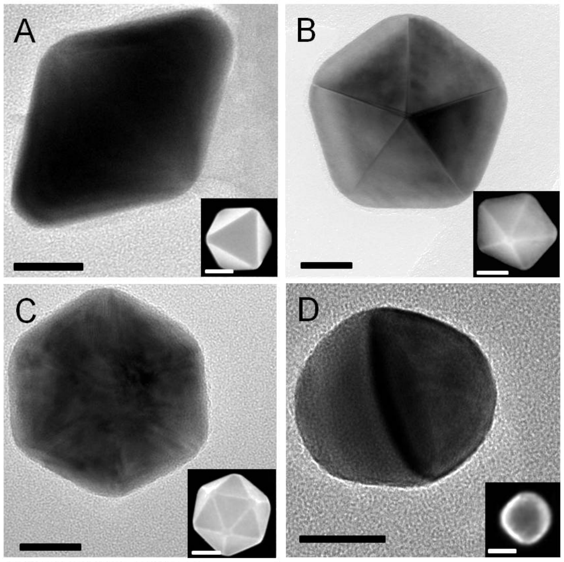

Figure 5.2: **TEM** images of (**A**) octahedral nanoparticle, (**B**) D_h nanoparticle, (**C**) m-I_h nanoparticle and (**D**) *ST* nanoparticle. Insets in (**A-D**) show scanning electron microscopy images of the same morphologies. Scale bar in (**A-D**) is 20 nm and 50, 50, 100 and 25 nm in the insets respectively.

In the experimental *set up*, D_h gold nanoparticles were deposited on a SiO2 substrate mounted them on a **TEM** specimen nano-indentation holder. Once a particle with the selected orientation has been found, the indentation probe was approached and the deformation initiates. Plastic deformation was produced by a large force applied on the nanoparticles.

Figure 5.3 shows the experimental plots of *true stress vs. true strain* curves for the four types of particles studied. The different behavior of the twinned particles

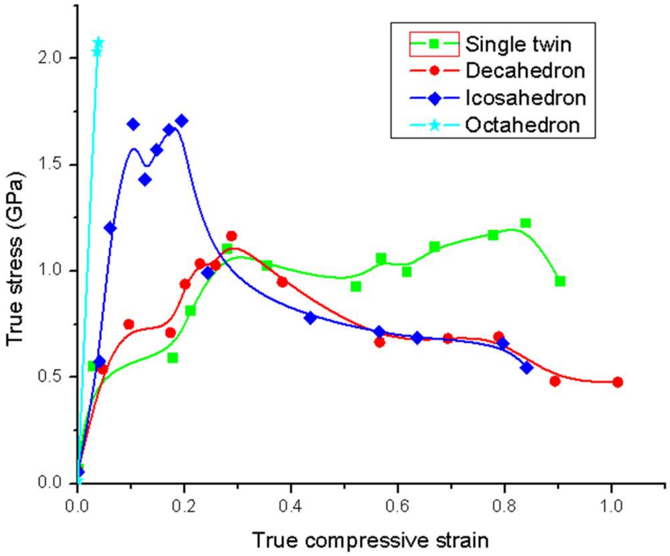

Figure 5.3: These plots shows that all the Au nanoparticles have a yield strength in the order of GPa, being the fcc the highest (yield strength not reached at 2 GPa) and the *ST* the lowest (around 0.5 GPa). From the *Ih* plot it can be seen that after the yield point there is strain hardening region up to a deformation of 20% and after that yields dropping the stress around 0.7 GPa. For the D_h the same thing happens, after the yield point there is a region of strain hardening up to 30% and then the stress drops around the 0.7 GPa. For the *ST* there is also a strain hardening region after the yield point, then the stress drops again around 30%, however, the is more strain hardening from compression of 60% up to 80%, then stress finally drops.

in comparison with the non-twinned particles is remarkable. Compression tests at ambient temperature showed an extremely high strength and the malleability coefficient for the single twinned particle is higher than 90% which is much higher than anything previously reported. The compression yield strength reached as high as 1.5 GPa for the icosahedron (0.7 GPa and 0.5 GPa for the decahedron and single twin respectively) and as for the octahedron was higher than 2.0 GPa but could not be reached with the particle size and hardware limitations. The nanoparticles can sustain yield strengths an order of magnitude higher than the bulk counterpart (25 MPa [30]) and considerably higher than gold thin films (390 MPa [31]). After the yield point on all the twinned particles there is an increase of stress with an increase of strain which evidences a *strain hardening* mechanism operating as the deformation advances. The fact that the fcc particle is brittle clearly shows the role of the TBs on the malleability and in the *work hardening* (strengthening of a metal by plastic deformation) of the nanoparticle.

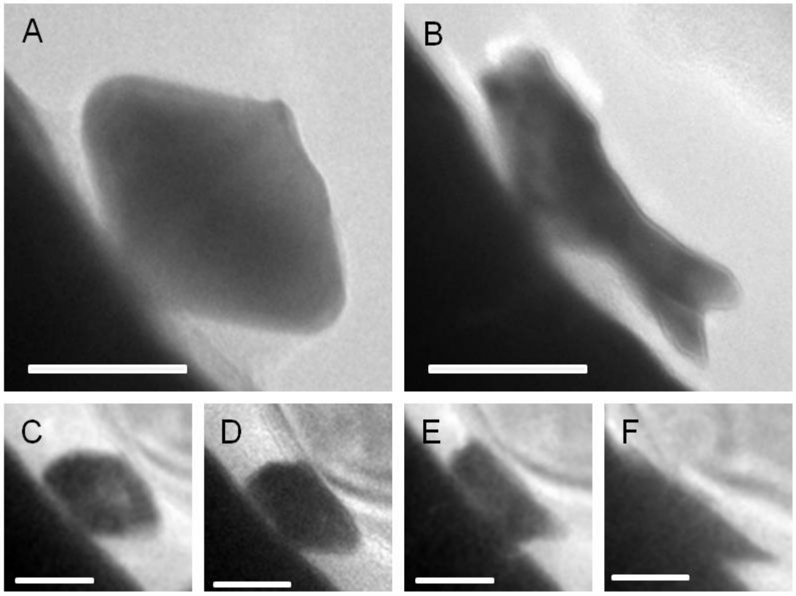

Figure 5.4: Before (**A**) and after (**B**) states of a D_h nanoparticle of a compression experiment. The particle was compressed 80%. (**C**-**F**) Sequence of a compression experiment of a D_h-nanoparticle. In this case the nanoparticle was compressed $\sim$100% and the true stress vs. true strain plot is shown in Fig. 5.3.

Figure 5.4 shows sequences of experimental images for D_h nanoparticles that exhibit dramatic plastic deformation. First close-ups of the morphologies of a D_h nanoparticle before and after a deformation experiment are shown in Fig. 5.4,**A** and Fig. 5.4,**B** respectively (80% compression). Figure 5.4,**C-F** shows the deformation sequence of a different D_h nanoparticle, in which case it was deformed $\sim$ 100%; the true stress vs true strain for this D_h is shown in Fig. 5.3.

Dark-Field images (Fig. 5.5 **b-g**) were used to follow the stress distribution in a D_h oriented on its five-fold axis (compressed $\sim$ 43%). When compression starts, a strain field is produced and propagates through the grains; as the deformation is progressing, dramatic changes on nanoparticle morphology can be observed. The first (Fig. 5.5 **a**) and the last (Fig. 5.5 **h**) figures correspond to bright field (**BF**) images whereas all the other correspond to weak beam dark field (**WBDF**) images using a (111) diffraction spot.

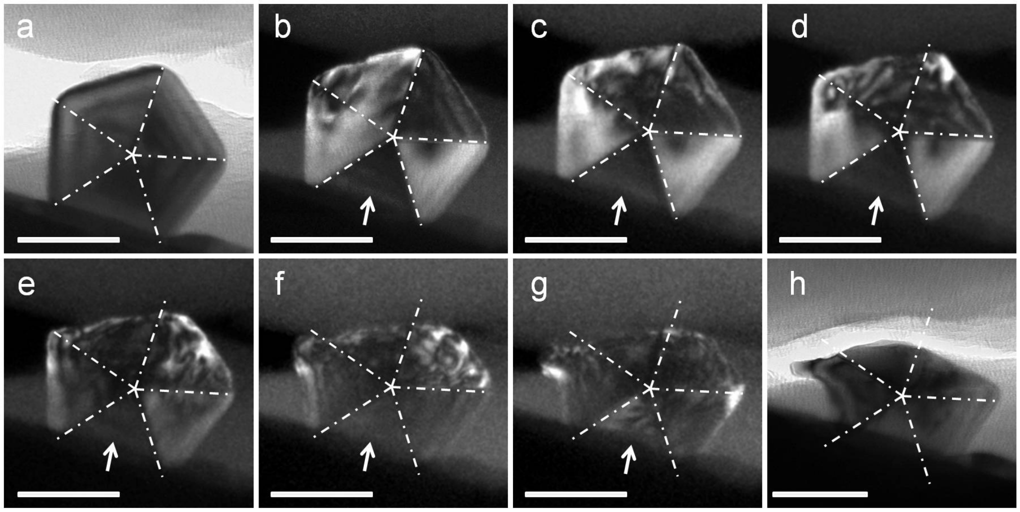

Figure 5.5: **a**, Setup of the experiment before deformation. From **b** to **h** is shown the evolution of the strain field in the particle. Only **a** and **h** are **BF** images, the rest correspond to **WBDF** images. The lower tetrahedron (pointed by the white arrow) showed almost no strain during the whole process until picture **g**, at which point the compression was about 27% in the tip direction. Scale bar are 50 nm.

As the compression takes place, strong strain field is produced at the termination of the twin boundaries at the surface of the particle, but the tetrahedral unit in contact with the SiO2 substrate does not show any evident stress (marked by a white arrow). However, after the D_h was compressed by 34% (Fig. 5.5 **g**), the lower tetrahedron started to show some bend contour fringes, meaning that strain initiated to build up there. This distribution of contrast is clearly the result of the stress field distribution on the D_h nanoparticle. The morphologies of D_h nanoparticle before and after deformation are shown in Figs. 5.6 **a** and 5.6 **b**.

Observe that the compression of the particle in the direction along the tip is about 34.4% after deformation, and that the center of the five-fold axis has shifted considerably after deformation. The same behavior was also observed in several Au D_h nanoparticles with an even larger deformation.

In the case of the *ST* nanoparticle, the plastic deformation measured was

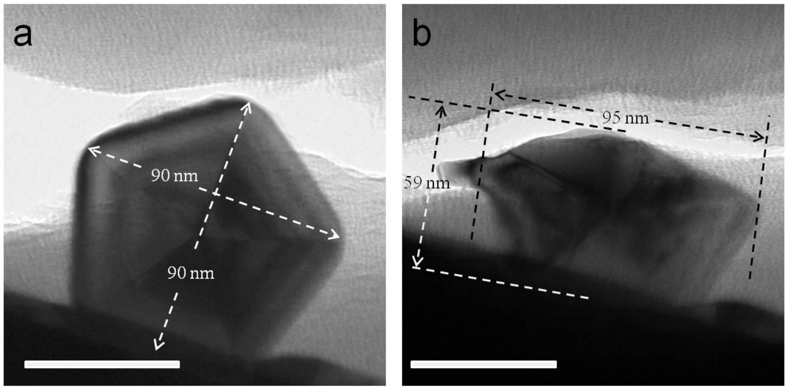

Figure 5.6: (**a**) Initial state of the D_h naoparticle.(**b**) Final state after ~35% of compression.

close to 90%. The octahedral nanoparticle (without twins) was tested with a maximum force of 5100 nN (2 GPa of stress) however, plastic deformation was not possible showing a more brittle behavior with higher yield strength than the particles with defects.

5.3 THEORETICAL ANALYSIS

In order to understand the experimental data we have performed calculations of the deformation process using molecular dynamics simulations.

5.3.1 METHOD

Molecular dynamics simulations were performed applying a frictionless indenter for the deformation of Au nanoparticles, using LAMMPS package ??. The *velocity-Verlet* integrator with a time step of 2 fs was used in the entire simulation, under the **NVE** ensemble. The embedded atom method potential was used to model the Au inter-atomic interactions. The whole simulation system was in a finite non-periodic simulation cell that consists of (a) the indenter, (b) a frictionless rigid plane as substrate where the NP is based and (c) the Au decahedron

($\sim$140,000 atoms). One decahedron placed with one tetrahedron based on the (100) planes (Fig. 5.7) and one decahedron is oriented with the five-fold symmetry axis in the direction of deformation (Fig. 5.9). The frictionless indenter is represented by an infinite fictitious wall with a repulsive potential of the type $F = k * (r - r_c)^2$, with k=10.0, and r being the distance from the plane to the approaching atoms, for simulation in Fig. 5.7, and an sphere with radius of 10 nm for the simulation in Fig. 5.9. This indenter was coupled with atomistic calculations to study the elastic and plastic deformation during indentation on the Au nanoparticles. Before mechanical loading, the structure of NPs was relaxed by means of the conjugate gradient method, and then NPs were thermally equilibrated to 10K for 300 ps using a *Nose-Hoover* thermostat. Starting from the equilibrium configuration of the nanocrystals, uniaxial compressive loading was applied. For the simulations presented in this study, during the loading process, indentation constant rate was 0.2 Å/ps, applied along the negative <100> direction (Fig. 5.7) and along the five-fold symmetry axis (Fig. 5.9) respectively.

We started with a Dh Au particle and applied a uniform uniaxial force. In order to understand the dynamics of the dislocations and stacking faults, we calculated the *centro-symmetry parameter P* for each atom defined in terms of the atomic coordination of the atoms [30]

$$P = \sum_{i=1}^{6} |\vec{R}_i + \vec{R}_{i+6}|^2 \tag{5.1}$$

where $\vec{R}_i$ and $\vec{R}_{i+6}$ are the vector or bonds corresponding to six pairs of opposite nearest neighbors in the fcc lattice. The 12 nearest-neighbors for each atom are first determined in an undistorted bulk lattice with the orientation of the slab. This number is a measure of the departure from centro-symmetry in the immediate vicinity of any given atom and is used to determine if the atom is near a defect. The *centro-symmetry parameter* is zero for atoms in a perfect fcc lattice, 24.9Å for surface atoms, 8.3Å for atoms located in an intrinsic stacking fault, and 2.1Å for atoms halfway between fcc and hcp sites, i.e., in a PD. These values assume that the gold nearest neighbor distance does not change in the vicinity of these defects. In practice, the *centro-symmetry parameter* can readily distinguish between these three types of environments, and as reference for Fig. 5.7, colors have been assigned that permit the distinction between atoms in PDs (red with P = 0.5$\sim$4.0) and for atoms in stacking faults (pale-red with P = 4.0$\sim$9.0) and for surface atoms P is in the range from 9 to 20 (blue). Atoms in bulk fcc environment (P =0.0$\sim$0.5) have been left out of the graph. The stress maps have been calculated using the virial expression for stress and the atomic volume needed for the stress per atom calculation was obtained by a Voronoi based algorithm [40].

5.3.2 RESULTS

For the nanoparticle compressed in the negative <100> direction, the sequence of deformation is shown in Fig. 5.7, where the deformation is shown from the initial, middle and latter stages of the deformation. Each frame shows the same elapsed time for two different orientations of the D_h particle. Frames at the left show the five-fold axis perpendicular to the observation, whereas frames on the right show the particle tilted so that this observation point help us to understand how partial dislocations emerge and their dynamics after a stage where enough stress has been accumulated at the other sides of the twin boundaries (**TB**). The indentator is coming from the left. At the beginning of the process partial dislocations are nucleated near the surface (red atoms) and start the deformation. The deformation front advances along the interface of two tetrahedral, parallel to the twin boundary. Partial dislocations are produced along all the surface of the tetrahedra affected by the indenter. In following steps, partial dislocations (PDs) are emitted by the twin boundary and dislocations fronts glide toward the other boundaries. Trailing PDs are produced. As the deformation advances the rate of PDs emission increases and many dislocation reactions are produced which result on the creation of many internal steps. It is remarkable that each twin boundary on the undeformed region is still coherent per se. Once the PDs arrive at the twin boundaries that were previously unaffected, effects not reported before in multi-twinned NPs are observed. The first one is seen on the two boundaries that are opposite to the **TB** in which the stress is applied. In the side opposite to the advance of the deformation we observe the formation of PDs with a burgers vector 1/6a <112> on the (111) twin plane. As the dislocation glides it emits a dislocation with burgers vector 1/2a <110> which immediately dissociates into partial dislocations with burgers vectors 1/6a <112> and 1/6a <-112> on the (1-11) slip plane [31–33]. As the dislocation motion continues they reach the surface of the D_h particle and deformation continues. Dislocations are constantly created on the two surfaces of tetrahedra **a** and **b** (see Fig. 5.7**a**). Eventually nucleation of PDs will begin in tetrahedra **c** and **d** at the **TB**s with **a** and **b** respectively. When the dislocations reach the pristine **TB**s, these become incoherent and the dislocation suffers a strong interaction in **e**.

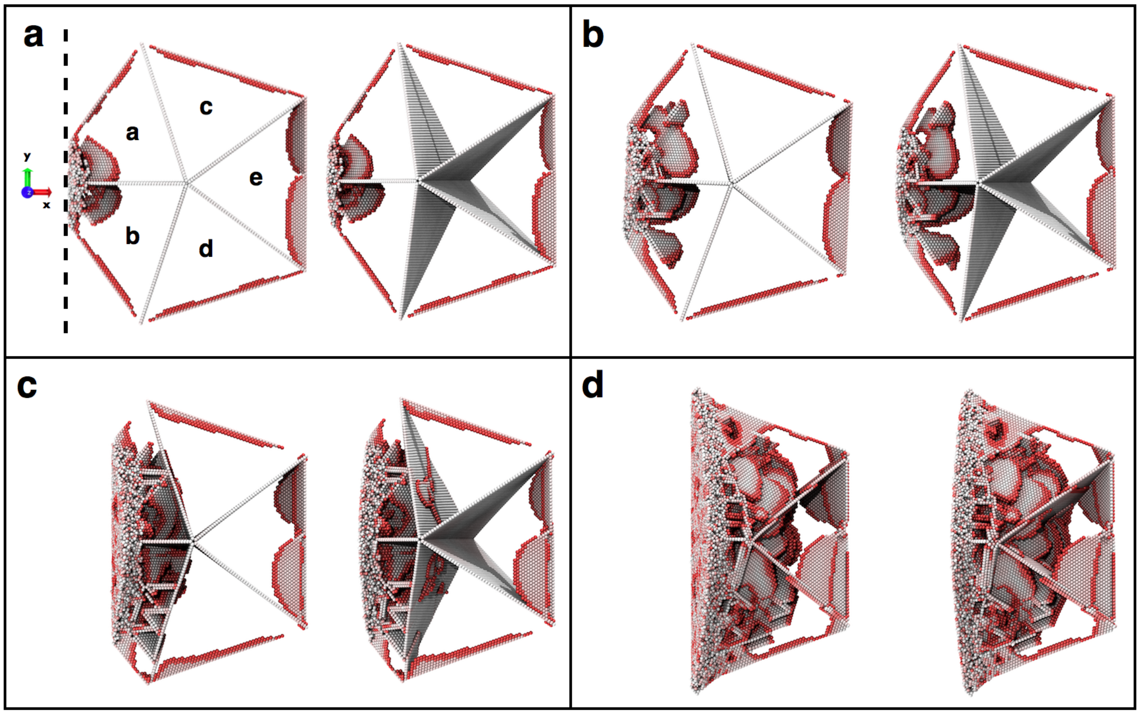

Figure 5.7: In these pictures, the atom color is related to the order parameter *P*. Atoms in red are located in PDs, whereas atoms in different tonalities of pale red are located in stacking faults (hcp environment). Bulk fcc atoms are not shown, and the indenter compressing the decahedron along the x direction is sketched by a dotted line in **a**. Both views in **a-d** correspond to the same time frame; just the one to the left has the five-fold axis parallel to the observation view, while the one to the right corresponds to a tilt of the axis of $\sim 30^{\circ}$ out of the perpendicular. In general, the production and movement of partial dislocations are the result of the deformation. Image **a** evidences the born and **b** the gliding of partial dislocations at early stages of deformation, which were nucleated near the surface and move along the T_h unit crystals. Images **c** and **d** show advanced stages of the deformation. However, notice that the twin boundaries act as dislocation barriers .

The results clearly show that many complex interactions and reactions are possible between PDs and coherent twin boundaries. After the interactions the boundary is displaced contributing to the deformation. As the deformation proceeds new internal surfaces are formed which contribute to the creation of new defects. It is important to note that the center of the D_h particles is displaced as a result of the deformation process, as well as a plastic deformation by almost 40%, being both results in agreement with the experimental observation. In order to further understand the remarkable properties of the D_h nanoparticles we have performed an analysis of the magnitude of the stress per atom on the decahedra at several stages of the deformation processes. Results for the same deformation stages from Fig. 5.7 are shown in Fig. 5.8. Here we have color coded the stress between 0 GPa (blue) and 4 GPa (red) frames to left and between 4 GPa (blue) and 20 GPa (red) frames to right and the scale in between (green tones). Both images complement each other. Atoms with a stress below 4 GPa are represented as voids, and are mainly located at the right side of the decahedron. Region of atoms with stress near or greater than 20 GPa can be observed mainly at the left of the decahedron, and a remarkable fact is that there are internal regions in the deformation front that present stress greater than 20 GPa, also represented by voids. Notice that in an advanced deformation stage the red colored atoms remain in the front line, along the heavily deformed region, and still the twin boundaries around the five-fold center of intersection of the five boundaries are almost undeformed, with a much lower stress $\sim$10GPa. In fact they are still coherent boundaries. The tetrahedron to the far right of the figure which is in contact with the substrate presents virtually no stress. In other words, the very particular geometry of the twin boundaries on D_h particles makes them a kind of filter for stress. Though the left side of the particle is under very heavy deformation, the right side is just slightly stressed, due to the efficient load distribution made by the twin boundaries in opposite to the deformation front. This fact is a very unique behavior in multi-twinned metallic nanoparticles. In fact we have calculated more advanced stages of deformation in which the deformation front has reach the center of the particle (the five-fold symmetry point) and still the **TB**s act as heavy dislocation blockers, being the last tetrahedron of the D_h almost undeformed.

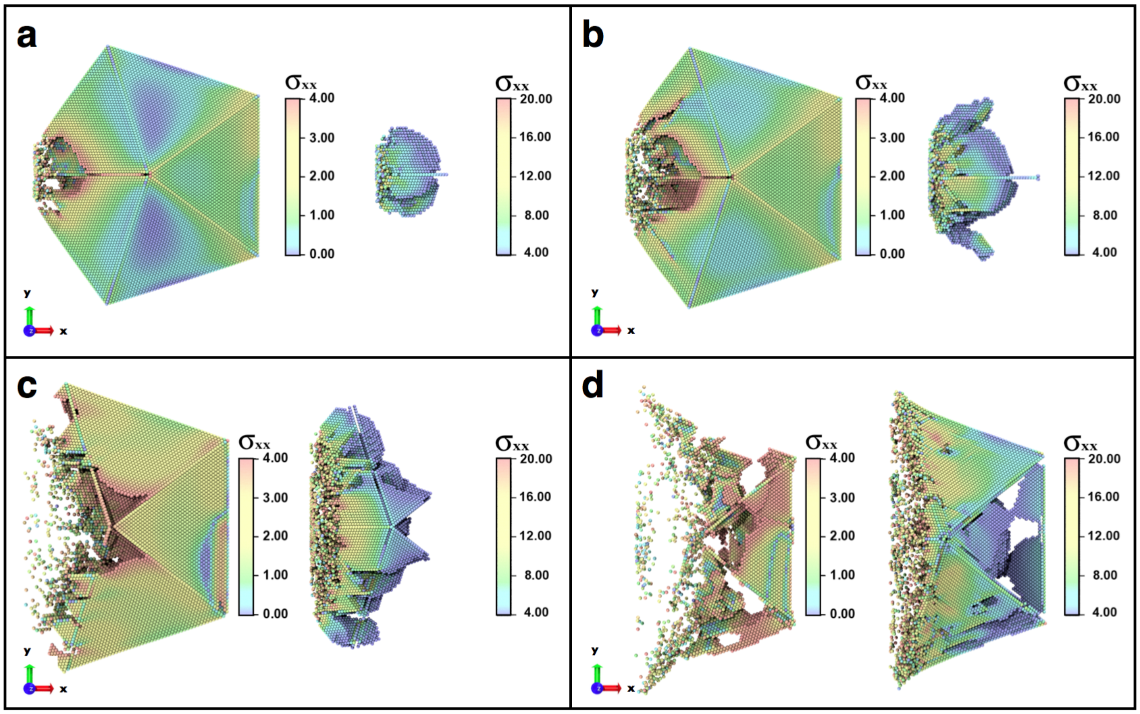

Figure 5.8: Sequence of images showing the σ_{xx} component of the stress tensor per atom, which is equivalent to the force per atom per unit area during the deformation of the decahedron. Frames to the left show a range stress from 0 GPa to 4 GPa, and to the right, the range stress is from 4 GPa to 20 GPa. In (**a**) stress builds up at the junction of the two tetrahedra separated by the twin boundary where the stress is applied. We can see that there is virtually no stress on the other 3 tetrahedra (8% compression). (**b**), Stress increments on the left side affecting the same leftmost tetrahedra. Stress is still very low on the other 3 tetrahedra (12% compression). (**c**), Stress starts to build up on the upper right and lower right tetrahedra at a compression of 20%. Tetrahedra on the left are highly deformed and there are atoms with stress greater than 20 GPa. (**a**), At a compression of 42% the two left tetrahedra are completely destroyed but remarkably the tetrahedron on the right just starts to have atoms with a stress higher than 4 GPa.

For the nanoparticle compressed in the five-fold symmetry axis, a sequence of deformation is shown in Fig. 5.9. This reproduces the experimental situation of Fig. 5.2. As expected, strain builds up around the contact point of the tip (Fig. 5.9**a**). This is also connected to the strain previously existing on the particle. At a strain of 20%, PDs nucleate and start to move along the TBs as shown in Fig. 5.9**b** (the dislocations start at the point where $|\varepsilon_{r\theta}|$ is maximum), until eventually they reach the surface and then move laterally creating steps at the surface (Fig. 5.9**c**). This process is repeated many times and is the onset of the plastic deformation. As the processes advances (Fig 5.9**d**), PDs parallel to the TBs are formed in the central part of each tetrahedron. We can see the multiplication of PDs with Burgers vectors 1/6a <112> on the (111) twin planes and the formation of many new **SF**s parallel to the **TB**s (Fig. 5.9**e**). Finally in Fig. 5.9**f** the D_h is 70% compressed with many **SF**s still moving in the tetrahedra. Figure 5.9**g** shows the true strain vs true strain plot calculated from the simulation which resembles the experimental curve. It has a first maximum around 0.5 GPa and then a second maximum around 0.6 GPa. While the strain value is different the magnitude of the stress is similar; this difference in strain can be attributed to the difference in size of the nanoparticle used in the simulation and those used in experiments. Fig. 5.9**g** also shows the correlation between the curve and the deformation process, it can be seen that the drops of stress are directly related with the slips of SFs parallel with the TBs.

5.4 DISCUSSION

In this chapter, we have presented a detailed study of indentation of individual multi-twinned metallic nanoparticles. Our results indicate that D_h gold nanoparticles show an outstanding high malleability. Based in our simulations we can propose a model to explain the ability of D_h nanoparticles to retain high compressive ductility while still being an strong material. The key roles are the nucleation

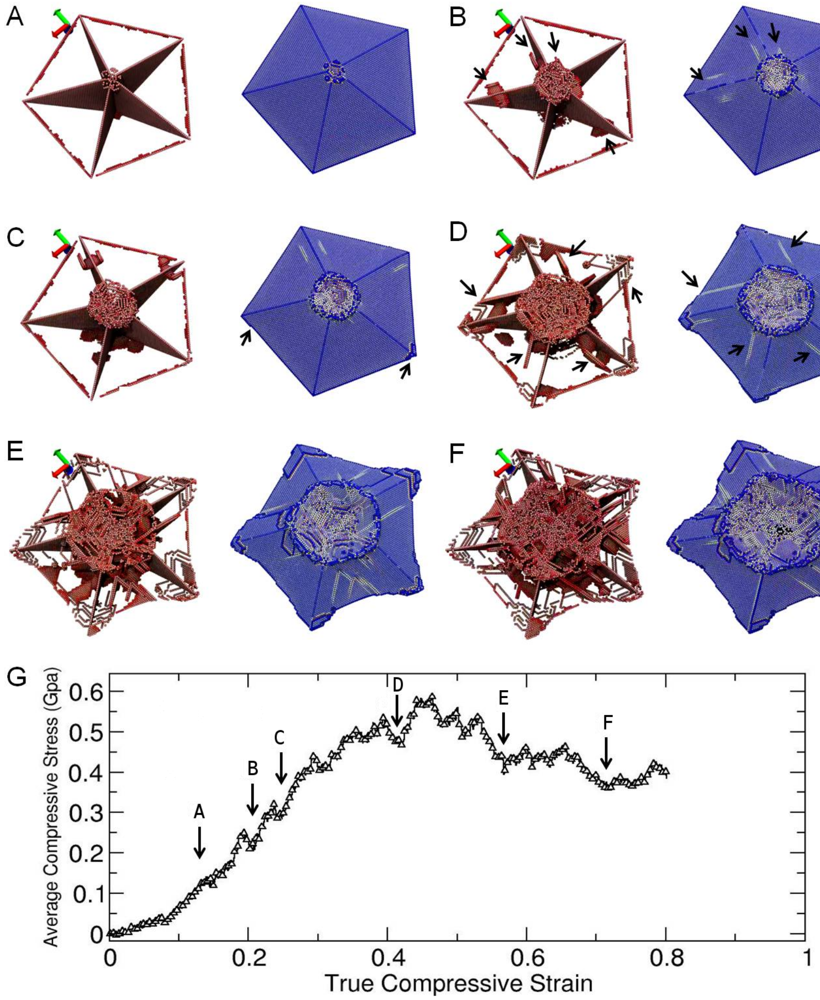

Figure 5.9: (**A**) First stage of deformation at 13% compression. (**B**) First PDs nucleated near and parallel the surface of the D_h moving along the TBs (pointed by the arrows) and eventually reaching the surface creating a step (at 20% compression). (**C**) At 24% compression the same type of PDs multiply and keep moving near the surfaces along the TBs creating more steps at the surfaces (pointed by the arrows). (**D**) At this point (42%) a new type of dislocation parallel to the twins contributes to the deformation of the D_h. We can see (pointed by arrows) that PDs move across the entire tetrahedron subunits moving in the direction of the twin creating further steps. (**E**) At this stage the stress dropped after reaching a maximum (around 48%) due to the formation of PDs parallel to the TBs. (**F**) There is another drop of stress and deformation continuous until the simulation ends at 80% of compression. (**G**) Calculated true stress vs true strain plot.

of partial dislocations and its interaction with coherent twin boundaries. This has been well established experimentally in many other cases [34]. If as result of the stress applied by the indenter the dislocations start to glide, it means that a critical resolved stress value on that direction has been passed. In order to describe the dislocation nucleation and reactions, it is convenient to use the standard Thompson notation [6] for the Burgers vectors. The Shockley partials generated are 1/6a<11-2> Bα, Aβ, γD and δC on the slip planes (a), (b), (c) and (d) respectively (see Fig. 5.10). When the PDs are nucleated at the stress sites that exist on the s-D_h nanoparticle (which are the result of the need of achieving stability at larger sizes), they start to glide on the (111) planes and on the <112> direction. If we assume that each tetrahedron is an fcc unit (which for nanocrystals of the size used on this study is a very good assumption), there will be four slip planes and six slip directions. If we use again the Thompson notation, there will be four slip systems (primary), (conjugate), (cross) and (critical), (see Fig. 5.10). When two tetrahedrons are joined forming a twin boundary, the geometry of the slip systems becomes symmetrical. So when the stress is applied along the TB between **a** and **b** (Fig. 5.7**a**) and PDs are nucleated, they glide on symmetrical regions on the twins. Thus the formation of Lomer-Cotrell (LC) locks become very likely. Lomer-Cotrell locks are formed by the following reactions: a/2<011> -> a/6<112> + a/6<-121> and a/2<10-1> -> a/6<11-2> + a/6<2-1-1>, the combination of this leading dislocations, gives

a/6<112> + a/6<11-2> -> a/3<110>

The resulting dislocation is along the crystal face, which is not a slip plane in fcc. When new PDs move they have to overcome the LC locks. Therefore this is an effective mechanism of strain hardening which operates on the middle stages of the deformation. As deformation proceeds and the deformation front reaches the central part of the particle. The two TBs between **a** and **c**, and between **b** and **d** (fig 5.7**c**) separate two grains that are also located on asymmetrical orientation with respect to the slip systems. Therefore when PDs are nucleated on those grains will also produce locks and will further contribute to stop dislocations. In fact these TBs are the ones that more contribute to the strain hardening. Passing these is very difficult and as a result the deformation advances significantly in the same perpendicular direction. Finally the new PDs cross the TBs or are nucleated at the right of these TBs and deformation advances.

In the case shown in Fig. 5.9 There are two well defined steps on the deformation mechanism. The PDs will move along the coherent twin boundaries and reach the surface producing steady state of deformation. This stage can be considered as "moderate" deformation. A next stage on the deformation is produced at the highest point of the stress in which new SFs parallel to the original TB are formed. This produces a catastrophic deformation which eventually leads to a star shaped nanoparticle. Our results clearly prove that particles that do not contain linear defects have much higher yield strength being more brittle than those with twins. In contrast particles containing twins show malleability that can be as high as 100%. The key phenomenon is the nucleation and multiplication of PDs that sustains plastic deformation, and their interaction with coherent TBs results in strain hardening.

5.5 CONCLUSIONS

Twenty years after the pioneering work of Gleiter was published, it has become clear that a route to achieve one of the original goals of nanotechnology: To develop ultra strong materials (smaller is stronger), is to introduce in a controlled way, internal coherent boundaries in the nanocrystalline grains [37]. Controlled introduction of coherent and stable nanostructured internal boundaries offers the possibility for introducing outstanding ductility.

In this chapter we have demonstrated that gold twinned nanoparticles combine a very high yield strength (0.5 to 2 GPa) with an outstanding malleability when subjected to stress, deforming plastically up to 100%. In addition, the effect

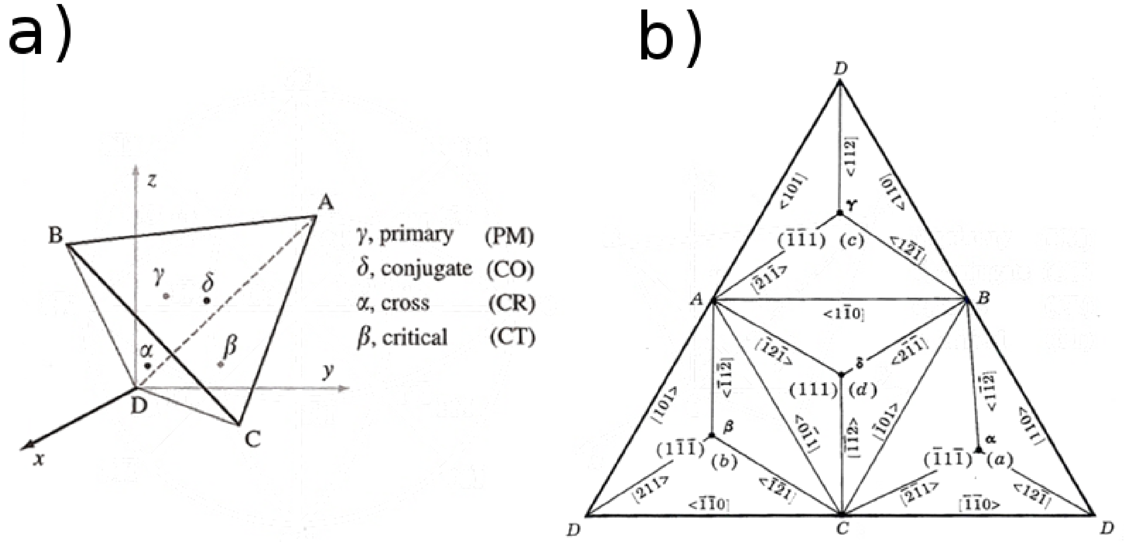

Figure 5.10: **a)** The Thompson tetrahedron representing the four {111} slip planes and the six slip directions. The four principal slip systems for a crystal with its axis located in the center region of the standard triangle are shown. The primary system (PM) is (11-1) [101], shown as Îş on the tetrahedron. The additional slip systems, conjugate (CO), critical (CT), and cross-slip (CR), are also shown in both the projection and the tetrahedron. **b)**, Opened out Thompson tetrahedron. Here the notation [110⟩ is used in place of the usual notation [110] to indicate the sense of the vector direction.

of strain hardening can be observed, which means that particles also increase their strength. These results open up potentially new exciting applications of twinned nanoparticles. Shapes such as the $\mathrm{D_h}$ and $\mathrm{I_h}$ are metastable and can be easily grown in different metals such as Au, Ag, Cu, Pd, Ir, It, and semiconductors such as Ge, Si, and in diamond. In the case of metals, it is possible to grow $\mathrm{D_h}$ particles in a very large range of sizes from 1 nm to 1 μm as is shown in Fig. 5.11. In recent years, it has been possible to produce high sample rates with at least 80% of decahedra [38]. This opens up the possibility of fabricating nanostructured materials with much better mechanical properties. The large plasticity and strengthening exhibited of the $\mathrm{D_h}$ nanoparticles can also be used to fabricate ultra efficient lubricants either by themselves or by mixing them with lubricant oils. When located between two metal surfaces and pressure is applied, nanoparticles would fill out the surface voids and irregularities on the surfaces, thus reducing friction losses and wear at the maximum possible level.

5.6 GENERAL CONCLUSIONS

The general conclusions of this thesis are:

The numerical solutions confirm the existing theoretical results that the main features of photon-assisted tunneling can be described by a classical trajectory in complex time. The probability of tunneling is governed by analytical properties of a nonstationary field and by those of a classical trajectory in the complex plane of time. This supports the general idea of applicability of trajectories to tunneling in a nonstationary case.

The results obtained open a way to apply the method of classical trajectories to more complicated problems of tunneling through nonstationary barriers, for example, to Euclidean resonance when the probability of tunneling through a classical barrier can be not exponentially small. The preliminary numerical study

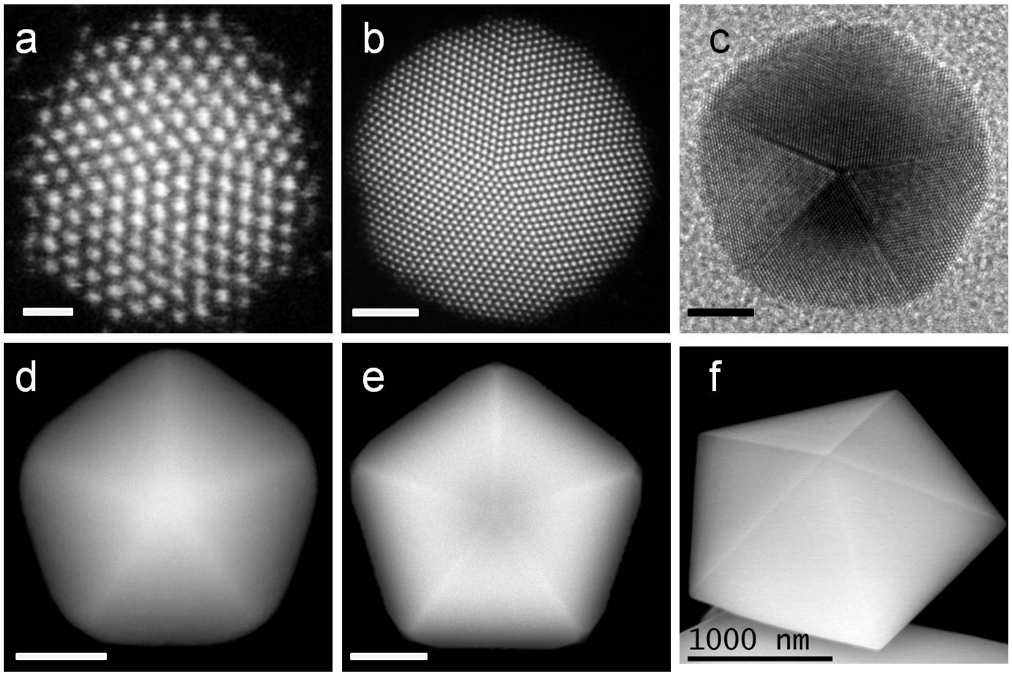

Figure 5.11: Different sizes for Au D_h nanoparticles. Particles in (**a-e**) correspond to high angle annular dark field **STEM** images. (**f**) corresponds to a **SEM** image formed using secondary electrons. This evidences the possibility to grow D_h nanoparticles in a wide range of sizes. Scale bars are 0.5 nm, 2 nm, 10 nm, 20 nm, 100 nm and 1 μm respectively.

of Euclidean resonance is presented in the tesis.

We have introduced the *decmon* decahedral motif for metallic NPs, which identifies a new family of decahedral structures. The decmon motif arises after proper truncations made on the icosahedron, it presents atomic facets (100) and (111) exposed in the surface, and whose energetic competition, at a given cluster size, make the structures very favorable from the energetic point of view.

We have finding structural transitions as a function of the cluster size, the appearing and competition of surface reconstruction with faceting, and the outlined path transformation from the m-I_h to the s-D_h symmetry structures.

A way to develop ultra strong materials, is to introduce in a controlled way, internal coherent boundaries in the nanocrystalline grains. Controlled introduction of coherent and stable nanostructured internal boundaries offers the possibility for introducing outstanding ductility.

We have demonstrated that gold twinned nanoparticles combine a very high yield strength (0.5 to 2 GPa) with an outstanding malleability when subjected to stress, deforming plastically up to 100%. In addition, the effect of strain hardening can be observed, which means that particles also increase their strength. These results open up potentially new exciting applications of twinned nanoparticles.

The large plasticity and strengthening exhibited of the D_h nanoparticles can also be used to fabricate ultra efficient lubricants either by themselves or by mixing them with lubricant oils. When located between two metal surfaces and pressure is applied, nanoparticles would fill out the surface voids and irregularities on the surfaces, thus reducing friction losses and wear at the maximum possible level.

BIBLIOGRAPHY

[1] Gleiter, H., Nanocrystalline materials. *Progress in Materials Science* 1989, **33 (4)**, 223-315.

[2] Gleiter, H., Nanocrystalline solids. *Journal of Applied* Crystallography 1991, **24**, 79-90.

[3] Gleiter, H., Nanostructured materials: basic concepts and microstructure. *Acta Materialia* 2000, **48 (1)**, 1-29.

[4] Suryanarayana, C.; Koch, C. C., Nanocrystalline materials - Current research and future directions. *Hyperfine Interactions* 2000, **130 (1)**, 5-44.

[5] Pokluda, J.; Cerny, M.; Sandera, P.; Sob, M., Calculations of theoretical strength: State of the art and history. *Journal of Computer-Aided* Materials Design 2004, **11 (1)**, 1-28.

[6] Hirth, J. P. a. L. J., *Theory of dislocations*. (Mcgraw Hill: New York, 1968).

[7] Courtney, T. H., *Mechanical Behavior of Materials*. 2nd ed.; (McGraw Hill: Boston, 2000).

[8] Zhu, T.; Li, J., Ultra-strength materials. Progress in Materials *Science* 2010, **55 (7)**, 710-757.

[9] Lu, L.; Chen, X.; Huang, X.; Lu, K., Revealing the maximum strength in nanotwinned copper. *Science* 2009, **323 (5914)**, 607-610.

[10] Lu, L.; Shen, Y.; Chen, X.; Qian, L.; Lu, K., Ultrahigh strength and high electrical conductivity in copper. *Science* 2004, **304 (5669)**, 422-426.

[11] Zhu, Y. T.; Liao, X. Z.; Wu, X. L., Deformation twinning in nanocrystalline materials. *Progress in Materials Science* 2011,**57 (1)**, 1-62.

[12] Wang, Z. L.; Gao, R. P.; Pan, Z. W.; Dai, Z. R., Nano-scale mechanics of nanotubes, nanowires, and nanobelts. *Advanced Engineering Materials* 2001, **3 (9)**, 657-661.

[13] Zheng, H.; Cao, A.; Weinberger, C. R.; Huang, J. Y.; Du, K.; Wang, J.; Ma, Y.; Xia, Y.; Mao, S. X., Discrete plasticity in sub-10-nm-sized gold crystals. *Nat. Commun.* 2010,**1 (9)**, 144.

[14] Agrait, N., Rubio, G. and Vieira, S., Plastic deformation of nanometer-scale gold connective necks. *Physical Review Letters* 1995, **74 (20)**, 3995-3992.

[15] Deng, C.; Sansoz, F., Near-ideal strength in gold nanowires achieved through microstructural design. *ACS Nano* 2009,**3 (10)**, 3001-3008.

[16] Diao, J.; Gall, K.; L. Dunn, M., Atomistic simulation of the structure and elastic properties of gold nanowires. *Journal of the Mechanics and Physics of Solids* 2004, **52 (9)**, 1935-1962.

[17] Ji, C. P., H. S., Geometric effects on the inelastic deformation of metal nanocrystals. *Applied Physics Letters* 2006,**89**, 181916.

[18] Sun, L.; Krasheninnikov, A. V.; Ahlgren, T.; Nordlund, K.; Banhart, F., Plastic deformation of single nanometer-sized crystals. *Physical Review Letters* 2008, **101 (15)**, 156101.

[19] Elechiguerra, J. L.; Reyes-Gasga, J.; Yacaman, M. J., The role of twinning in shape evolution of anisotropic noble metal nanostructures.*Journal of Materials Chemistry* 2006, **16 (40)**, 3906-3919.

[20] Hofmeister, H., Forty years study of fivefold twinned structures in small particles and thin films. *Crystal Research and Technology* 1998, **33 (1)**, 3-25.

[21] Howie, A.; Marks, L. D., Elastic strains and the energy balance for multiply twinned particles. *Philosophical Magazine A* 1984, **49 (1)**, 95-109.

[22] Ino, S., Stability of multiply-twinned particles. *Journal of the Physical Society of Japan* 1969, **27 (4)**, 941-953.

[23] Johnson, C. L.; Snoeck, E.; Ezcurdia, M.; Rodriguez-Gonzalez, B.; Pastoriza-Santos, I.; Liz-Marzan, L. M.; Hytch, M. J., Effects of elastic anisotropy on strain distributions in decahedral gold nanoparticles. *Nat. Mater.* 2008, **7 (2)**, 120-124.

[24] Jose-Yacaman, M., Asencio, J., Liu, H. B., and Gardea, J., Structure shape and stability of nanometric sized particles (Review Article). *Journal of Vacuum Science and Technology B* 2001, **19 (4)**, 1091-1103.

[25] Jose-Yacaman, M. A., M., Eletron microscopy of metallic nano-particles using high and medium resolution techniques. *Catalysis Review:Science and Engineering* 1992, **34 (1 and 2)**, 55-127.

[26] Koga, K., Novel bidecahedral morphology in gold nanoparticles frozen from liquid. *Physical Review Letters* 2006, **96 (11)**, 115501.

[27] Marks, L. D., Modified Wulff constructions for twinned particles. *Journal of Crystal Growth* 1983, **61 (3)**, 556-566.

[28] Marks, L. D.; Howie, A., Multiply-twinned particles in silver catalysts.*Nature* 1979, **282 (5735)**, 196-198.

[29] Wit, R. d., Partial disclinations. *Journal of Physics C: Solid State Physics* 1972, **5 (5)**, 529.

[30] Savitskii, E. M., *Handbook of Precious Metals*. (Hemisphere Publishing Company: New York, 1969).

[31] Wang, L.; Prorok, B. C., Characterization of the strain rate dependent behaviour of nancrystalline gold films. *Journal of Materials Research* 2007,**23 (1)**, 55-65.

[32] Tsuzuki, H.; Branicio, P. S.; Rino, J. P., Structural characterization of deformed crystals by analysis of common atomic neighborhood. *Computer Physics Communications* 2007, **177 (6)**, 518-523.

[33] Gannepalli, A.; Mallapragada, S. K., Atomistic studies of defect nucleation during nanoindentation of Au(001).*Physical Review B* 2002,**66 (10)**, 104103.

[34] Jin, Z. H.; Gumbsch, P.; Albe, K.; Ma, E.; Lu, K.; Gleiter, H.; Hahn, H., Interactions between non-screw lattice dislocations and coherent twin boundaries in face-centered cubic metals. *Acta Materialia* 2008, **56 (5)**, 1126-1135.

[35] Kelchner, C. L.; Plimpton, S. J.; Hamilton, J. C., Dislocation nucleation and defect structure during surface indentation. *Physical Review B* 1998, **58 (17)**, 11085-11088.

[36] Tsuru, T.; Kaji, Y.; Matsunaka, D.; Shibutani, Y., Incipient plasticity of twin and stable/unstable grain boundaries during nanoindentation in copper. *Physical Review B* 2010,**82 (2)**, 024101.

[37] Lu, K.; Lu, L.; Suresh, S., Strengthening Materials by Engineering Coherent Internal Boundaries at the Nanoscale. *Science* 2009,**324 (5925)**, 349-352.

[38] Pietrobon, B.; McEachran, M.; Kitaev, V., Synthesis of Size-Controlled Faceted Pentagonal Silver Nanorods with Tunable Plasmonic Properties and Self-Assembly of These Nanorods. *ACS Nano* 2008,**3 (1)**, 21-26.

[39] Tsai, D., The virial theorem and stress calculation in molecular dynamics. *J. Chem. Phys.* 1979, **70 (3)**, 1375.

[40] Gerstein, M.; Tsai, J.; Levitt, M., The Volume of Atoms on the Protein Surface: Calculated from Simulation, using Voronoi Polyhedra. *Journal of Molecular Biology* 1995, **249 (5)**, 955-966.

CHAPTER 6

APENDIX

6.1 FINITE DIFFERENCES

The finite difference methods have dominated computational science since its inception and were the method of choice in the 1960s and 1970s. While other methods, such as the finite element method and boundary element have enjoyed recent popularity, finite difference methods are still utilized for a wide array of computational engineering and science problems. In the finite differences methods, the derivatives are approximated by differences between neighboring points on a grid. In a one-dimensional ($1D$) problem on the x-axis with $x \in [0, L]$, a finite difference method introduces a set of grid points $x_0, x_1, ..., x_N$ where a sought function $u(x)$ takes the values $u(x_0), u(x_1), \dots, u(x_N)$.

Let us denote as u_j the values $u(x_j)$ (discretization of the function $u(x)$), then

$$u_j = u(x_j) = u(j\Delta x), \quad j = 0, \dots, N \tag{6.1}$$

where $\Delta x = L/N$.

A basic role to estimate the error involved in finite difference approximations of function derivatives is played by the well-known Taylor's series expansion

$$f(x+\Delta x) = f(x) + \sum_{h=1}^{n-1} f^{(h)}(x)\frac{(\Delta x)^h}{h!} + f^{(n)}(x+\theta\Delta x)\frac{(\Delta x)^n}{n!}, \tag{6.2}$$

where $0 < \theta < 1$ and $f^{(h)}$ denotes the hth derivative of f. This equation can also be written as

$$f(x+\Delta x) = f(x) + \sum_{h=1}^{n-1} f^{(h)}(x)\frac{(\Delta x)^h}{h!} + O((\Delta x)^n), \tag{6.3}$$

here $O((\Delta x)^n)$ represents the error of the aproximation and is proportional to $(\Delta x)^n$.

Now, if we apply 6.3 to u_j gives

$$u(x_j+\Delta x) = u(x_j) + u^{'}(x_j)\Delta x + O((\Delta x)^2) \tag{6.4}$$

which, by using notation 6.1, is written as

$$u_{j+1} = u_j + u_j^{'}\Delta x + O((\Delta x)^2) \tag{6.5}$$

that is,

$$u_j^{'} = \frac{u_{j+1} - u_j}{\Delta x} + O(\Delta x). \tag{6.6}$$

Hence, it follos the aproximation formula for the derivative of u, called *forward approximation*,

$$u_j^{'} \approx \frac{u_{j+1} - u_j}{\Delta x}. \tag{6.7}$$

Equation 6.12 implies a leading error of order Δx. The *backward approximation* is inferred in analogous way, that is,

$$u_j' \approx \frac{u_j - u_{j-1}}{\Delta x}. \tag{6.8}$$

Now, let us define the *central approximation*. Applying Taylor's expansion 6.3 with $n = 4$ yields

$$u_{j+1} = u_j + u_j' \Delta x + u_j'' \frac{(\Delta x)^2}{2!} + u_j''' \frac{(\Delta x)^3}{3!} + O((\Delta x)^4), \tag{6.9}$$

$$u_{j-1} = u_j - u_j' \Delta x + u_j'' \frac{(\Delta x)^2}{2!} - u_j''' \frac{(\Delta x)^3}{3!} + O((\Delta x)^4) \tag{6.10}$$

Substracting 6.10 from 6.9 gives

$$u_{j+1} - u_{j-1} = 2u_j' \Delta x + O((\Delta x)^3) \tag{6.11}$$

that is,

$$u_j' = \frac{u_{j+1} - u_{j-1}}{2\Delta x} + O((\Delta x)^2). \tag{6.12}$$

Then, the *central approximation* for u' is

$$u_j' \approx \frac{u_{j+1} - u_{j-1}}{2\Delta x}, \tag{6.13}$$

with a leading error of order $(\Delta x)^2$.

For the second order derivative u_j'' the *central approximation* can be obtained summing equations 6.9 and 6.10, and solving with respect to u_j'', that is,

$$u_j'' \approx \frac{u_{j+1} - 2u_j + u_{j-1}}{(\Delta x)^2}. \tag{6.14}$$

The leading error of this formula is of order $(\Delta x)^2$ as 6.13.

6.2 NUMERICAL SOLUTION OF THE SCHRÖDINGER'S EQUATION

The Schrodinger equation can be written as

$$i\hbar\frac{\partial\psi}{\partial t} = \mathbf{H}\psi \tag{6.15}$$

where H is the Hamiltonian operator,

$$\mathbf{H} = -\frac{\hbar^2}{2m}\frac{\partial^2\psi}{\partial x^2} + V(x)\psi \tag{6.16}$$

The formal solution of equation 6.19 is

$$\psi(x,t) = \mathbf{exp}\left(-\frac{i}{\hbar}\mathbf{H}t\right)\psi(x,0) \tag{6.17}$$

Various schemes have been proposed to approximate the exponential function, one of the most used is the CRANK-NICHOLSON scheme (*CN*). In this scheme the exponential function is approximated by a Cayley transformation, i. e. by a rational approximation with two first degree polynomials:

$$\psi(t+\Delta t) = \frac{1 - iH\Delta t/2\hbar}{1 + iH\Delta t/2\hbar}\psi(t) + O((\Delta t)^3) \tag{6.18}$$

The spatial interval $[xmin, xmax]$ is divided into equally spaced points with separation Δx, resulting in a net $x_{min} = x_0, x_1, \ldots, X_J = x_{max}$. The solution in time n at the point j is denoted by ψ_j^n. To calculate $\mathbf{H}\psi_j^n$ is necessary to approximate the second derivative appearing in the Hamiltonian. In the *CN* scheme, this approach is done using finite differences

$$\frac{\partial^2\psi}{\partial x^2} \approx \frac{\psi_{j+1}^n - 2\psi_j^n + \psi_{j-1}^n}{\Delta x^2} \tag{6.19}$$

Then, using a matrix notation, the wave function is obtained from the wave function at the previous time through the relation

$$\left(\mathbf{I}+\frac{i\Delta t}{\hbar}\mathbf{H}\right)\blacksquare^{\mathbf{n+1}}=\left(\mathbf{I}-\frac{i\Delta t}{\hbar}\mathbf{H}\right)\blacksquare^{\mathbf{n}} \tag{6.20}$$

where **I** is the identity matrix, and Δt is the time step that has been used in the discretization of the problem. As can be seen from Eq. 6.20, each iteration of the algorithm requires the solution of a system of linear equations, which will result in the wave function at each time step. The *CN* scheme has the advantage that is unconditionally stable and preserves the norm of the wave function, besides being of second order in Δt and Δx.

6.2.1 TRANSPARENT BOUNDARY CONDITIONS

The time dependent Schröedinger equation, is a parabolic type partial diferential equation which is normally defined in an infinite domain with well defined boundary conditions (usually the solution must tend to zero at the ends of the domain). However, for a numerical treatment of the problem, it is necessary to restrict the original problem to a finite interval. This approach results in the emergence of reflections on the boundaries that affect the wave function dynamics and therefore the generation of errors in the calculation of physical quantities. One solution is to increase the range of integration, but in most cases it is necessary to use very large intervals, which increases the computational cost and memory requirements. In order to eliminate or at least reduce these reflections, special procedures have been developed, allowing then to use smaller spatial domains. In these procedures special boundary conditions are imposed, which obviously must be consistent with the original boundary conditions on the total space. One of the best methods is the one proposed by Ehrhardt and Arnold [1]. This method avoids the numerical reflections at the borders in addition to maintaining the unconditional stability of the *CN* scheme.

By using this procedure, the resulting boundary conditions are:

$$\psi_1^n - s_0^{(0)}\psi_0^n = \sum_{k=1}^{n-1} s_0^{(n-k)}\psi_0^k - \psi_1^{n-1}, \quad n \geq 1, \tag{6.21}$$

$$\psi_{J-1}^n - s_J^{(0)}\psi_J^n = \sum_{k=1}^{n-1} s_J^{(n-k)}\psi_J^k - \psi_{J-1}^{n-1}, \quad n \geq 1, \tag{6.22}$$

where

$$s_j^{(n)} = \left[1 - i\frac{R}{2} + \frac{\sigma_j}{2}\right]\delta_n^0 + \left[1 + i\frac{R}{2} + \frac{\sigma_j}{2}\right]\delta_n^1 + \alpha_j e^{-in\varphi_j}\frac{P_n(\mu_j) - P_{n-2}(\mu_j)}{2n-1},$$

$$\varphi_j = arctan\frac{2R(\sigma_j + 2)}{R^2 - 4\sigma_j - \sigma_j^2}, \quad \mu_j = \frac{R^2 + 4\sigma_j + \sigma_j^2}{\sqrt{(R^2 + \sigma_j^2)[R^2 + (\sigma_j + 4)^2]}},$$

$$\sigma_j = \frac{2\Delta x^2}{\hbar^2}V_j, \quad \alpha_j = \frac{i}{2}[(R^2 + \sigma_j^2)(R^2 + (\sigma_j + 4)^2)]^{\frac{1}{4}} e^{i\varphi_j/2}, \quad j = 0, J.$$

P_n denotes the *Legendre polynomials* ($P_{-1} \equiv P_{-2} = 0$) and δ_{ij}^n is the *Kronecker delta*. Note that these boundary conditions are nonlocal in time, *i. e.*, it is necessary to know the value of the wave function on the ends of the domain for all previous times, so the calculation time increases with each iteration.

BIBLIOGRAPHY

[1] M. Erhardt and A. Arnold, Rev. Mat. Univ. Parma, $\mathbf{6/4}$, 57 (2001).